



# Decay Spectroscopy of $^{100}\text{Sn}$ and Neighboring Nuclei

**Daniel Georg Lubos**

Vollständiger Abdruck der von der Fakultät für Physik der Technischen Universität München zur Erlangung des akademischen Grades eines

**Doktors der Naturwissenschaften (Dr. rer. nat.)**

genehmigten Dissertation.

Vorsitzender Univ.-Prof. Dr. Norbert Kaiser

Prüfer der Dissertation  
1. Univ.-Prof. Dr. Reiner Krücken  
2. Univ.-Prof. Dr. Stefan Schönert

Die Dissertation wurde am 2. November 2016 bei der Technischen Universität München eingereicht und durch die Fakultät für Physik am 23. November 2016 angenommen.



# Zusammenfassung

In dieser Arbeit werden Atomkerne entlang der  $N = Z$  Linie in der Nähe der Protonenabbruchkante um den doppelt magischen Kern  $^{100}\text{Sn}$  untersucht. Die Eigenschaften dieser Isotope sind von großer Bedeutung für die theoretische Beschreibung durch Kernmodelle.

$^{100}\text{Sn}$  ist ein idealer Modellkern zum Studium des Schalenmodells, weil er dominant durch einen Gamow-Teller Übergang eines Protons im  $\pi g_{9/2}$ -Orbital in ein Neutron im  $\nu g_{7/2}$ -Orbital in  $^{100}\text{In}$  zerfällt. Unterschiede zwischen Schalenmodellrechnungen und experimentell bekannten Werten der Übergangsstärke konnte zuletzt durch Verwendung großer Konfigurationsräume mit bis zu 5-Teilchen 5-Loch Anregungen berücksichtigt werden. Wegen der mangelnden Genauigkeit in der Bestimmung der Übergangsstärke konnte bisher aber nicht zwischen verschiedenen theoretischen Modellen unterschieden werden. Die genaue Vermessung der Lebensdauern des Wartepunktkerns  $^{96}\text{Cd}$  sowie der Kerne  $^{98}\text{In}$ ,  $^{94}\text{Ag}$  und  $^{90}\text{Rh}$ , die durch einen übererlaubten Fermi-Übergang zerfallen können, sind wichtig für das Verständnis des astrophysikalischen rp-Prozesses und der Theorie vom erhaltenen Vektorstrom.

Am Kernforschungszentrum RIKEN Nishina Center in Japan wurde dazu ein Experiment mit einem  $^{124}\text{Xe}$ -Primärstrahl bei einer Energie von  $E_{\text{kin}} = 345$  AMeV und einer Intensität bis zu  $I_{\text{Xe}} = 36$  pA durchgeführt. Die exotischen Kerne wurden durch Fragmentation des Projektils an einem  $^9\text{Be}$ -Target erzeugt und anschließend im hochauflösenden Magnetseparator BigRIPS getrennt. Zur Zerfallsspektroskopie wurde ein breiter Cocktail exotischer Projektilfragmente im Massenbereich  $A = 100$  in das Siliziumdetektorarray WAS3ABi implantiert. Dieses ermöglichte eine detaillierte Untersuchung angeregter Zustände in Verbindung mit dem Germaniumspektrometer EURICA.

Insgesamt wurden 2525  $^{100}\text{Sn}$ -Kerne und eine große Anzahl von Nukliden entlang der  $N = Z - 1$  Linie erzeugt. Dadurch können Lebensdauern,  $Q_\beta$ -Werte und die Verzweigungsverhältnisse der Zerfallskanäle dieser Kerne mit hoher Genauigkeit bestimmt werden. Die Halbwertszeit von  $^{100}\text{Sn}$  mit  $1.17 \pm 0.10$  s und die  $\beta$ -Endpunktenergie mit  $Q_\beta = 3.74 \pm 0.14$  MeV führen zu einer Gamow-Teller Übergangsstärke von  $5.26^{+0.90}_{-1.06}$ . Erste Hinweise auf niederenergetische Gamma-Übergänge liefert die Gammaspektroskopie nach dem  $\beta$ -Zerfall von  $^{100}\text{Sn}$ , so dass das bisher bekannte Termschema für  $^{100}\text{In}$  in diesem Zusammenhang bestätigt wird. Die Untersuchung von ungerade-ungerade  $N = Z$  Kernen lieferte präzise Ergebnisse über deren Halbwertszeiten. Einen isomeren Zustand des Kerns  $^{90}\text{Rh}$  konnte in Analogie zu den Kernen  $^{94}\text{Ag}$  und  $^{98}\text{In}$  entdeckt werden. Darüberhinaus wurden die Halbwertszeiten der  $N = Z - 1$  Kerne  $^{99}\text{Sn}$ ,  $^{97}\text{In}$ ,  $^{95}\text{Cd}$  und  $^{91}\text{Pd}$ , die dominant in ihren isobaren Analogzustand zerfallen, bestimmt. Im Vergleich zu diesen Kernen stellte sich  $^{93}\text{Ag}$  als Protonenemitter jenseits der Protonenabbruchkante heraus. Seine Halbwertszeit wurde zu  $T_{1/2} = 228 \pm 16$  ns ermittelt. Erstmals wurden die noch exotischeren Kerne entlang der  $N = Z - 2$  Linie  $^{96}\text{In}$ ,  $^{94}\text{Cd}$ ,  $^{92}\text{Ag}$  und  $^{90}\text{Pd}$  identifiziert und deren Halbwertszeiten bestimmt.



# Abstract

Nuclei around the heaviest known, doubly-magic  $N = Z$  nucleus  $^{100}\text{Sn}$  are investigated within this thesis. The detailed knowledge of their nuclear properties is important for the understanding of nuclear models.  $^{100}\text{Sn}$  is an ideal show case to study the nuclear shell model because of its dominant Gamow-Teller decay by a transition of a  $\pi g_{9/2}$ -proton into a  $\nu g_{9/2}$ -neutron in  $^{100}\text{In}$ . Large-scale shell model calculations considering large configuration spaces up to 5-particle 5-hole excitations have already been in agreement with previous experimental values. However, theoretical models could not be discriminated yet. The  $N = Z$  nuclei below  $^{100}\text{Sn}$  are also very interesting. The half-lives of the waiting point nucleus  $^{96}\text{Cd}$  as well as the odd-odd  $N = Z$  nuclei  $^{98}\text{In}$ ,  $^{94}\text{Ag}$ , and  $^{90}\text{Rh}$  are important regarding the understanding of the astrophysical rp-process and the theory of the conserved vector currents.

In order to address these questions, an experiment was performed at the RIKEN Nishina Center in Japan with an beam energy of  $E_{\text{kin}} = 345$  AMeV and intensities up to 36 pA. Exotic nuclei were produced by projectile fragmentation of a  $^{124}\text{Xe}$ -beam impinging on a  $^9\text{Be}$ -target. The fragment separation and identification has been achieved by using the high-resolution magnetic separator BigRIPS. In order to perform decay spectroscopy, a cocktail of various fragments in the mass region  $A = 100$  was implanted into the silicon detector array WAS3ABi where subsequent decays were also observed. In combination with the surrounding Ge-spectrometer EURICA, excited states, half-lives,  $Q$ -values and branching ratios were studied.

During the experiment, 2525 nuclei  $^{100}\text{Sn}$  as well as a large amount of  $N = Z - 1$  nuclei were identified. Thus, the half-lives,  $\beta$ -endpoint energy and branching ratios of the decay channels of these species were precisely determined. The half-life of  $^{100}\text{Sn}$  was measured to  $1.17 \pm 0.10$  s and the  $Q_\beta$ -value of its dominant transition was determined to  $Q_\beta = 3.74 \pm 0.14$  MeV resulting in a Gamow-Teller transition strength  $\mathcal{B}_{\text{GT}}$  of  $5.26^{+0.90}_{-1.06}$  such that theoretical models can be challenged by means of an experiment for the first time. The gamma-spectroscopy after the  $\beta$ -decay of  $^{100}\text{Sn}$  reveals first hints with regards to the missing low energy transitions. This confirms a previously proposed level scheme of the daughter nucleus  $^{100}\text{In}$ . The analysis of the odd-odd  $N = Z$  nucleus  $^{90}\text{Rh}$  reveals precise half-lives and an isomeric  $5^+$ -state in analogy to the nuclei  $^{94}\text{Ag}$  and  $^{98}\text{In}$  for the first time. The gamma-spectroscopy has given evidence of an expected isomeric state of  $^{98}\text{In}$  which decays to an  $8^+$ -state and the core-excited  $10^+$ -state of  $^{98}\text{Cd}$ . Beyond the analysis of these nuclei, the half-lives of the  $N = Z - 1$  nuclei  $^{99}\text{Sn}$ ,  $^{97}\text{In}$ ,  $^{95}\text{Cd}$  and  $^{91}\text{Pd}$ , which decay dominantly into their isobaric analog states, was performed with unprecedented precision.  $^{93}\text{Ag}$  was unambiguously identified as a proton emitter with a half-life of  $228 \pm 16$  ns beyond the proton dripline. Finally, the even more exotic  $N = Z - 2$  nuclei  $^{96}\text{In}$ ,  $^{94}\text{Cd}$ ,  $^{92}\text{Ag}$  and  $^{90}\text{Pd}$  were newly identified and their half-lives were determined for the first time.



# Contents

<b>1</b>	<b>Introduction and Physical Motivation</b>	<b>1</b>
1.1	The Nuclear Shell Model & Mean Field	1
1.2	The $\beta$ -Decay	4
1.3	The Nuclear Structure around $^{100}\text{Sn}$	6
1.4	The Superaligned Fermi Decay	8
1.5	$\beta$ -Delayed Proton Emission and Direct $p$ -Decay	10
1.6	The rp-Process	11
<b>2</b>	<b>Experimental Setup</b>	<b>13</b>
2.1	The RI Beam Factory	13
2.1.1	The Production Mechanism	14
2.2	The Fragment Separator BigRIPS	16
2.3	Particle Identification	18
2.4	The Detector Setup for Decay Spectroscopy	21
2.4.1	The Silicon Detector Array WAS3ABi	22
2.4.2	Energy Calibration of the Si-Detectors in WAS3ABi	24
2.4.3	The EURICA Spectrometer	26
2.4.4	The Detection Efficiency	28
2.5	The Detector Readout	30
<b>3</b>	<b>Analysis</b>	<b>33</b>
3.1	Half-Life Analysis	33
3.1.1	The Maximum Likelihood Approach (MLH)	34
3.1.2	Example: The p.d.f. of the Radioactive Decay	35
3.1.3	The Bateman Equations	36
3.1.4	Analysis from First Decay Correlations	37
3.1.5	Test of the Half-Life Analysis	38
3.1.6	The Background Evaluation	39
3.2	Event Discrimination of Implantation and Decay Events	40
3.2.1	Implantation & Decay	40
3.2.2	Positrons & Protons	40

3.3	The Correlation Technique for Implantation and Decay Events	42
3.3.1	Isomeric Transitions	42
3.3.2	Detection of the $\beta$ -Decay	43
3.4	Determination of $Q_\beta$ -Values	44
3.4.1	Positron Tracking & The Detector Response	44
3.4.2	The $\chi^2$ -Method	47
3.4.3	Test of the $\chi^2$ -Method with $^{98}\text{Cd}$	49
<b>4</b>	<b>Decay Spectroscopy</b>	<b>51</b>
4.1	Determination of Half-Lives	51
4.1.1	$N = Z - 2$ Nuclei	51
4.1.2	$N = Z - 1$ Nuclei	52
4.1.3	Even-Even $N = Z$ Nuclei	55
4.1.4	Odd-Odd $N = Z$ Nuclei	59
4.1.5	Determination of the $\beta p$ -Branching Ratios	69
4.2	The Level Scheme of $^{100}\text{In}$	70
4.3	Search for the Isomeric $6^+$ -state of $^{100}\text{Sn}$	75
4.4	$Q_\beta$ -Value & Transition Strength	76
4.4.1	The $\beta$ -Endpoint Energy of $^{100}\text{Sn}$	76
4.4.2	The Gamow-Teller Transition Strength of $^{100}\text{Sn}$	80
<b>5</b>	<b>Summary &amp; Prospects</b>	<b>83</b>
5.1	Summary of the Results	83
5.2	Why the Region of $^{100}\text{Sn}$ Remains Interesting	84
5.3	Summary of the Half-Lives	85
	<b>Appendix</b>	<b>86</b>
A	The Gamow-Teller Transition Strength	86
B	The Fermi-Function	87
C	The Construction of the p.d.f for the First Correlation	87
D	Half-Life Plots & Tables	89

## Abbreviations & Acronyms

ADC	Analog-to-Digital Converter
AME	Atomic Mass Evaluation
CFD	Constant Fraction Discriminator
CKM	Cabibbo-Kobayashi-Maskawa
CVC	Conserved Vector Current
DAQ	Data Acquisition
DGF	Digital Gamma Finder
DSSD	Double Sided Silicon-strip Detector
ESM	Extreme Single particle Model
EURICA	Euroball RIKEN Cluster Array
FFST	Finite Fermi System Theory
FRS	FRagment Separator at GSI
GT	Gamow-Teller
HPGe	High-Purity Ge-detector
LED	Leading Edge Discriminator
LSSM	Large Scale Shell Model
LUPO	Logical Unit for Programmable Operation
MLH	Maximum Likelihood
NNDC	National Nuclear Data Center
PID	Particle Identification
PPAC	Parallel-Plate Avalanche Counter
QRPA	Quasi-Random Phase Approximation
RIBF	Radioactive Isotope Beam Factory
RILAC	RIKEN Linear Accelerator
RTD	Room-Temperature Dipole magnet
SC-ECR	Superconducting Electron Cyclotron Resonance
SIMBA	Silicon Implantation detector and Beta Absorber
SSSD	Single Sided Silicon-strip Detector
STQ	Superconducting Quadrupole Triplets
TAS	Total Absorption Spectrometry
TFA	Time-Filter Amplifier
TDC	Time-to-Digital Converter
TEGIC	Tilted Electrode Gas Ionization Chamber
TOF	Time-Of-Flight
WAS3ABi	Wide-range Active Silicon-Strip Stopper Array for Beta and ion detection

# List of Figures

1.1	The Nuclear Chart	2
1.2	The Shell Model	3
1.3	Log( $ft$ )-Values	6
1.4	Detection Sensitivity of the Gamow-Teller Transition Strength	7
1.5	Shell Structure of $^{100}\text{Sn}$	8
1.6	Charge and Radiative Corrections of the log( $ft$ )-Values	9
1.7	Schematic of the $\beta\text{p}$ -Decay	10
1.8	The Path of the Rapid-Proton Capture Process	11
2.1	Overview Schematic of the RIBF Facilities	14
2.2	RIBF Configuration at Fixed Energy	15
2.3	Schematic of the BigRIPS Separator	17
2.4	Schematic of the TEGIC Detector	19
2.5	Particle Identification Plot of the Present Experiment	20
2.6	Cross Sections for the Exotic Beam Production	21
2.7	Schematic of the WAS3ABi-Detectors	22
2.8	Calibration of Si-Detectors	25
2.9	Decay Scheme of $^{60}\text{Co}$	26
2.10	Geometry of the EURICA Spectrometer	27
2.11	Schematic of the Addback Method	27
2.12	Isomeric $\gamma$ -Transitions of $^{98}\text{Cd}$	28
2.13	Efficiency Calibration Curve of the EURICA-Spectrometer	29
2.14	The Detector Readout	31
3.1	Radioactive Decay Chains	37
3.2	Test of Self-Consistency of the Half-Life Analysis	38
3.3	Benchmark Test of the Half-Life Analysis using $^{98}\text{Cd}$	39
3.4	Discrimination of Decay Events	41
3.5	Sectional View of the WAS3ABi Detector Geometry	43
3.6	Front View of a DSSD and Multiple-Scattering	44
3.7	Z-Position Sensitivity of Simulated $Q_{\beta}$ -Spectra	45
3.8	Simulation Input and Output	46
3.9	Analysis of Strip Groups in Si-Detectors	47
3.10	The Phase Space of $\beta^+$ -Particles	48
3.11	Analysis of Systematic Uncertainties of $Q_{\beta}$ -Values	49
3.12	Determination of the $Q_{\beta}$ -Value in $^{98}\text{Cd}$	50
4.1	Half-Life of $^{95}\text{Cd}$	53
4.2	Extrapolation of the $Q_p$ -Value of $^{93}\text{Ag}$	54
4.3	Half-Life of the Decay Products Correlated with $^{93}\text{Ag}$ Implantations	55

4.4	Determination of Half-Lives in $^{100}\text{Sn}$	57
4.6	Determination of Half-Lives in $^{96}\text{Cd}$	58
4.5	Level Scheme of $^{96}\text{Cd}$	58
4.7	Determination of Half-Lives in $^{92}\text{Pd}$	60
4.8	Discrimination of Fermi- and GT-Transitions in $^{98}\text{In}$	61
4.9	Determination of Half-Lives in $^{98}\text{In}$	62
4.10	Decay Scheme of $^{98}\text{In}$ and the $\beta p$ -Branch	63
4.11	$Q_{\text{EC}}$ -Dependence on the Ratio of Intensities	63
4.12	$\gamma$ -Spectroscopy of $^{94}\text{Ag}$ and $^{90}\text{Rh}$	66
4.13	Determination of Half-Lives in $^{94}\text{Ag}$ and $^{90}\text{Rh}$	67
4.14	Determination of $\beta p$ -Branching Ratios in $^{98}\text{In}$	68
4.15	Search of the 2p-Decay in $^{94}\text{Ag}$	68
4.16	Determination of $\beta p$ -Branching Ratios in $^{98}\text{In}$	69
4.17	Scenarios for the Level Scheme of $^{100}\text{In}$	71
4.18	$\gamma$ -Spectroscopy in $^{100}\text{Sn}$	72
4.19	Absolute Intensities of the $\gamma$ -Transitions in $^{100}\text{In}$	73
4.20	Coincidence Analysis of $\gamma$ -Emission in $^{100}\text{In}$	74
4.21	Level Scheme and Measurements of the Isomeric State of $^{100}\text{Sn}$	76
4.22	Level Scheme of $^{100}\text{In}$	77
4.23	Determination of the $Q_{\beta}$ -Value in $^{100}\text{Sn}$	79
4.24	Gamow-Teller Transition Strength of $^{100}\text{Sn}$	82
5.1	Total Absorption Spectrometry in $^{100}\text{Sn}$	84
D.1	Determination of Half-Lives in $^{98}\text{In}$ , $^{94}\text{Ag}$ and $^{90}\text{Rh}$	90
D.2	Coincidences of $^{98}\text{In}$ and $^{94}\text{Ag}$	91
D.3	Coincidences of $^{90}\text{Rh}$	92
D.4	Half-Lives of $N = Z - 1$ Nuclei	92

## List of Tables

1.1	Selection Rules of the $\beta$ -Decay	5
2.1	Characteristics of the BigRIPS Separator	17
2.2	Number of Implantations per Layer for $N = Z$ Nuclei	24
4.1	Half-Lives of $N = Z - 2$ Nuclei	52
4.2	Half-Lives of $N = Z - 1$ Nuclei	54
4.3	Half-Lives of $^{100}\text{Sn}$ in Literature	57
4.4	Half-Lives of $^{98}\text{In}$ in Literature	64
4.5	$\beta$ -Delayed $\gamma$ -Correlations in the Search of the 2p-Decay in $^{94}\text{Ag}$ Nuclei	69
5.1	Summary of Half-Lives	85
D.1	Decay Correlations of $N = Z - 2$ Nuclei	89

# 1 Introduction and Physical Motivation

The region around doubly magic  $^{100}\text{Sn}$  is unique with regard to the understanding of the nuclear structure and effective interactions.  $^{100}\text{Sn}$  is the heaviest proton bound doubly magic  $N=Z$  nucleus close to the proton dripline and it proceeds by the fastest  $\beta$ -decay in the nuclear chart. Since large scale shell model (LSSM) calculations predict a very pure Gamow-Teller (GT) transition, while a Fermi-transition is forbidden,  $^{100}\text{Sn}$  is the most adequate nucleus to derive the axial-vector coupling constant  $g_A$ . Apart from  $^{100}\text{Sn}$ , the neighboring odd-odd  $N=Z$ -nuclei as well as the  $N=Z-1$  nuclei have  $\beta$ -decay branches which proceed by the Superallowed Fermi-decay. Thus, the study of nuclei from this region provides another test of the conserved-vector current (CVC) hypothesis and it allows for the calculation of the first matrix element  $V_{ud}$  of the Cabibbo-Kobayashi-Maskawa quark mixing matrix (CKM-matrix).

In addition, nuclei around the  $N=Z$ -line take part in the astrophysical rapid-proton capture process (rp-process) which terminates just above  $^{100}\text{Sn}$  due to  $\alpha$ -unbound  $^{105-107}\text{Te}$ -isotopes. Hence, this region is strongly connected with astrophysics and accurate nuclear properties are needed for astrophysical reaction network calculations. The region provides the ideal testing ground for the nuclear shell model. A comprehensive discussion of the physics and experimental techniques to produce and investigate nuclei of the region around  $^{100}\text{Sn}$  is given by Faestermann, Gorska, and Grawe [FGG13]. This chapter gives an introduction into the essential physics. In particular, the nuclear shell model as well as Fermi and Gamow-Teller  $\beta$ -transitions are discussed.

## 1.1 The Nuclear Shell Model & Mean Field

Studying the binding energies of nuclei, maxima occur at certain numbers, on top of a smooth trend which is described by the Bethe-Weizsäcker mass formula [BB36]. This anomaly of binding energies, which goes along with certain proton and neutron numbers, was the reason for their names: *magic nuclei*. Recalling atomic physics, noble gases show a similar behavior as the electron binding energy is at its maximum when the corresponding electron shells are completely filled (closed shell). For this reason, a shell model approach to nuclei was developed with the basic assumption that each nucleon moves independently in a spherically symmetric potential. In first approaches, the harmonic oscillator potential  $V_{\text{HO}}(r) = -V_0(1 - (r/R)^2)$ ,  $r < R$  and the Woods-Saxon-Potential  $V_{\text{WS}}(r) = -V_0(1 + \exp((r - R)/a))^{-1}$ ,  $r < R$  were used in the shell model Hamiltonian  $\mathcal{H}_{\text{SM}}$ .  $V_0$  represents the depth of a potential well,  $a$  is the surface parameter and  $R = r_0A$  represents the nuclear radius with  $r_0 = 1$  fm and the mass number  $A$ . Herein, closed shells result from large gaps between certain single-particle energies. Indeed, these potentials result in the occurrence of large shell gaps between

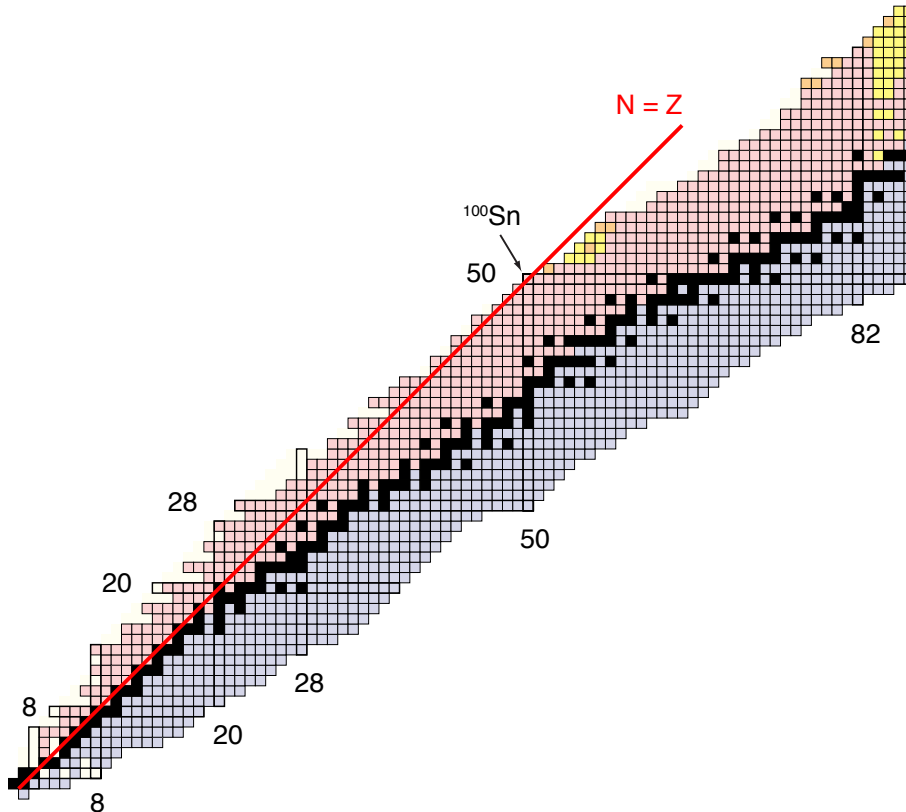


**Figure 1.1:** The nuclear chart. The color code describes the dominant decay channel. Black: stable, red:  $\beta^+$ -decay, blue:  $\beta^-$ -decay and yellow:  $\alpha$ -decay. The figures denote the magic numbers.

certain orbitals corresponding to the magic numbers. But only the numbers 2, 8 and 20 were reproduced while those of heavier nuclei with  $N, Z > 20$  could not be explained. This discrepancy was resolved by the introduction of a spin-orbit coupling term (**LS**-term) that manifests in a large correction compared to a small correction in atomic physics, which changes the order of spacings between energy levels. It causes a splitting of the energy levels with angular momentum  $\ell$  into levels with spin  $j_{\geq} = \ell \pm \frac{1}{2}$ . The levels with  $j_{>} = \ell + \frac{1}{2}$  are shifted down and levels with  $j_{<} = \ell - \frac{1}{2}$  are shifted up resulting in an energy splitting  $\Delta E_{\ell \pm \frac{1}{2}} \propto 2\ell + 1$  where each level is  $2j + 1$ -fold degenerated. Ultimately, this term reproduces all proton and neutron numbers at which maxima has been observed in the binding energies when Goeppert-Mayer and Jensen [GMJ55], Goeppert-Mayer [GM48] and Haxel, Jensen, and Suess [HJS49] has developed this correction of the nuclear shell model ( $\rightarrow$  Fig. 1.1). This approach allows for the phenomenological description of the magic numbers. However, one strives for a more fundamental understanding of the origin of shell structure based on the interaction of the nucleons with each other. Modern approaches make use of self-consistent mean-field potentials where the many-body problem is turned into a one-body problem [SP08]. The most general Hamiltonian which considers only two-body nucleon-nucleon forces is

$$\mathcal{H} = \sum_{k=1}^A T(k) + \sum_{1=k<\ell}^A V(k, \ell) \quad (1.1)$$

with the kinetic energy  $T$  of particle  $k$  and the potential  $V$  of the interaction between two particles  $k$  and  $\ell$ . The second sum consists of  $(A-1)!$ -terms. Hence, this expression



It is attractive in case of adding two particles ( $pp$ ) to the core and repulsive in case of adding a pair of an interacting particle and a hole ( $ph$ ). However, the energy gain by the residual interaction of two unlike nucleons, which are added to the core, depends on the relative orientation of their angular momenta and is maximum for parallel spins and minimum for orthogonal spins. In the case of two like particles the monopole interaction is significantly weaker as the Pauli principle requires the space-spin part of the wave function to be anti-symmetric and only even spins are allowed for this configuration. In contrast, the addition of unlike particles in an odd-spin configuration implies a symmetric space-spin wave function which generates a much stronger attractive interaction. Concerning the study of the nuclear interaction from a fundamental point of view, the monopole term is further divided into three terms. A central term, the spin-orbit coupling and the tensor coupling:

$$V_C(1, 2) = V_0(r) + V_\sigma(r)\sigma_1 \cdot \sigma_2 + V_\tau(r)\tau_1 \cdot \tau_2 + V_{\sigma\tau}(r)\sigma_1 \cdot \sigma_2\tau_1 \cdot \tau_2 \quad (1.4)$$

$$V_{LS}(1, 2) = (V_{LS}^{is}(r) + V_{LS}^{iv}(r)\tau_1 \cdot \tau_2)\mathbf{L} \cdot \mathbf{S} \quad (1.5)$$

$$V_T(1, 2) = (V_T^{is}(r) + V_T^{iv}(r)\tau_1 \cdot \tau_2)S_{12}(r) \quad (1.6)$$

$$S_{12} = \frac{3}{r^2}(\sigma_1 \cdot \mathbf{r})(\sigma_2 \cdot \mathbf{r}) - \sigma_1 \cdot \sigma_2 \quad (1.7)$$

$\sigma$  is the spin-operator,  $\tau$  denotes the isospin operator and labels  $is, iv$  denote the isoscalar and iso-vector components of the interactions, respectively. The  $V_{LS}(1, 2)$ -term corresponds to what has been discussed before. The tensor interaction  $V_T$ , which is another contribution to the monopole interaction, results in an attraction of unlike spin-orbit partners  $j_<, j'_>$  and a repulsion of like spin-orbit partners  $j_<, j'_<$  [Ots+05], with  $j_<, j_>$  denoting the down and upshifted energy levels due to the  $\mathbf{LS}$ -term. Other contributions occur due to three-body forces which are not considered in the Hamiltonian ( $\rightarrow$  Eqn. 1.1). Conclusively, nuclei with proton and neutron numbers around magicity are the ideal playground to probe the Shell Model and study the NN-interaction as well as the nuclear structure.

## 1.2 The $\beta$ -Decay

The  $\beta$ -decay is a three-body process while the neutrino was postulated by von Meyenn, Hermann, and Weisskopf [vHW85] in order to explain the continuous energy spectrum of electrons in the  $\beta$ -decay and the evidence of the neutrino was given by Cowan et al. [Cow+56]. In neutron rich nuclei, it proceeds by a decay to a proton ( $\beta^-$ -decay) while in proton rich nuclei a proton decays into a neutron ( $\beta^+$ -decay).

$$\beta^- : n \rightarrow p + e^- + \bar{\nu}_e$$

$$\beta^+ : p \rightarrow n + e^+ + \nu_e$$

$$\text{EC} : p + e^- \rightarrow n + \nu_e$$

The last line represents the electron capture (EC) decay channel which is the inverse of the  $\beta^+$ -decay where an electron is captured from the  $K$ -shell of the atom. This is the only accessible decay process if the mass of the  $Z + 1$ -neighbor is only smaller by less than  $2m_e c^2$ . The  $\beta$ -decay is mediated by the  $W$ -bosons of the weak interaction. While Fermi [Fer34] has proposed to describe the  $\beta$ -decay by a parity conserving current  $j^\mu$ , this

Change of	Fermi transition	Gamow-Teller transition
isospin $T$	$\Delta T = 0$	$\Delta T = 0, \pm 1$
nuclear spin $I$	$\Delta I = 0$	$\Delta I = 0, 1$
angular momentum $L$		$\Delta L = 0$
parity $\pi$		$\Delta\pi = 0$

**Table 1.1:** Selection rules of the Fermi and Gamow-Teller transitions.

had to be adjusted when maximum parity violation of the  $\beta$ -decay was observed in the experiment by Wu et al. [Wu+57]. This issue was solved by the introduction of an axial-vector current accounting for the asymmetry. Then, the interaction of the  $\beta$ -decay is given as

$$\mathcal{H}_{V-A} = \frac{1}{\sqrt{2}} \int d^3r \cdot \bar{\psi}_p g_V \gamma^\mu (1 - g_A \gamma_5) \psi_n \cdot \bar{\psi}_e \gamma_\mu (1 - \gamma_5) \psi_\nu \quad (1.8)$$

with  $g_V = 1, g_A = 1.26$  being the coupling constants of the vector and axial-vector currents, respectively,  $\gamma_\mu$  being the Lorentz-invariant Dirac-matrices and  $\psi_i$  denoting the wave functions of the proton, neutron, positron and neutrino. This interaction can be used to determine the transition probability  $\lambda$  of the  $\beta$ -decay by Fermi's Golden Rule

$$\lambda = \frac{2\pi}{\hbar} |\langle \psi_f | \mathcal{H}_{V-A} | \psi_i \rangle|^2 f(Z, Q_\beta) \quad (1.9)$$

where  $f(Z, Q_\beta)$  is Fermi's function representing the phase space, which depends on the nuclear charge of the daughter nucleus  $Z$  and the  $Q_\beta$ -value.  $Q_\beta$  is the reaction energy of the  $\beta$ -decay which determines the endpoint of the  $E_{\beta\pm}$ -distribution where the electron carries the complete reaction energy while the mass of the neutrino is negligible. The derivation and explanation is given in Appendix A and B. The decays which are mediated by the vector current are the so called *Fermi*-transitions where the nuclear spin does not change such that the spins of the emitted leptons have to be anti-parallel. On the other hand, in the *Gamow-Teller*-transition, which is mediated by the axial-vector current, the nuclear spin flips and the lepton spins are parallel. The transition strength  $\mathcal{B}$  of these two channels is generally written as

$$\mathcal{B}_F = |\mathcal{M}_V|^2 = |\langle \psi_f | \tau_\pm | \psi_i \rangle|^2 \quad (1.10)$$

$$\mathcal{B}_{GT} = |\mathcal{M}_A|^2 = |\langle \psi_f | \sigma \tau_\pm | \psi_i \rangle|^2 \quad (1.11)$$

where  $\psi_{i,f}$  denotes the wave functions of initial and final states,  $\tau$  is the isospin operator and  $\sigma$  the spin operator. The selection rules for both  $\beta$ -decay channels are summarized in Table 1.1. These expressions are the results of the Born approximation considering the wave functions of the leptons as plane waves since the recoil of the nucleus is negligible because of the lepton mass which is more than three orders of magnitude smaller than the nuclear mass. Then, the leptonic wave function  $\psi_{lep} = \frac{1}{\sqrt{\mathcal{V}}} e^{i\mathbf{p}\cdot\mathbf{x}/\hbar} = \frac{1}{\sqrt{\mathcal{V}}} [1 + \frac{i\mathbf{p}\cdot\mathbf{x}}{\hbar} + \dots]$  is an expansion in the angular momentum  $\ell$  where  $\mathcal{V}$  is the normalization volume. Thus, as the order of the expansion increases, the contribution of each term drops by a factor of  $10^{-4} - 10^{-3}$  (supposing momenta in the range of  $\approx 2$  MeV/c and the radius  $R \approx 2 - 3$  fm). Consequently, these decay channels do only play a role if the Fermi- and Gamow-Teller transition with  $\ell = 0$  are hindered. The forbiddenness of a decay is classified by the

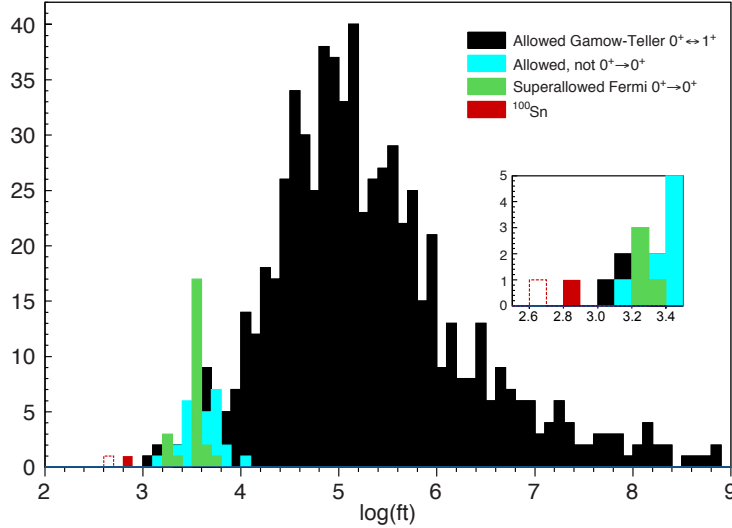


**Figure 1.3:** Histogram of the  $\log(ft)$ -values in the nuclear chart. The majority of the nuclei decays by a Gamow-Teller transition (black) as the Fermi-transitions (green) are confined to nuclei around the  $N=Z$  line which can decay into the isobaric analogue state.  $^{100}\text{Sn}$  (red) has the smallest  $\log(ft)$ -value in the nuclear chart. The dashed, red bin marks the value from the previous experiment [Hin+12] while the filled, red bin represents the result from this work. The histogram is generated from the compilation of  $\log(ft)$ -values in the Nuclear Data Sheets [Sin+98].

change of angular momentum  $\ell$ , represented by the  $\log ft$ -value which is often used as a guidance for the forbiddenness of a transition. The smaller the  $\log ft$ -value is, the higher is its transition probability. The distribution of  $\log ft$ -values throughout the nuclear chart is shown in Figure 1.3 where the exceptional value for  $^{100}\text{Sn}$  as measured in this work, is marked by the red filled bin.

### 1.3 The Nuclear Structure around $^{100}\text{Sn}$

In the region of  $^{100}\text{Sn}$ , the orbital  $\pi g_{9/2}$  is filled between Nb ( $Z=41$ ) and Sn ( $Z=50$ ).  $^{100}\text{Sn}$  is the heaviest known proton-stable doubly magic nucleus on the  $N=Z$ -line which is expected to be near the proton dripline. As the shell is closed when the  $\nu g_{9/2}$ -orbital is filled, neutrons occupy the orbitals above the shell gap starting with the  $\nu d_{5/2}$ -orbital according to the extreme single particle model (ESM) [ST63]. These shells are accessible in the  $\beta$ -decay due to the shift of the proton shells to lower binding energies because of the Coulomb interaction. The  $\nu g_{7/2}$  and  $\nu d_{5/2}$  are almost degenerate ( $\rightarrow$  Fig. 1.5). However, due to the selection rules, the matrix elements are highly suppressed if  $\Delta L \neq 0$  and other transitions allowed by the change of angular momentum  $\Delta L = 0$  (e. g.  $\pi f_{7/2} \rightarrow \nu f_{5/2}$ ) are forbidden due to the Pauli principle. Thus, the Gamow-Teller transition into the  $\nu g_{7/2}$ -orbital is strongly favored. Calculations in the ESM even predict a pure  $\pi g_{9/2} \rightarrow \nu g_{7/2}$  transition [Gra+95]. The transition strength in this model is given according to [ST63]

$$\mathcal{B}_{\text{GT}}^{\text{ESM}} = \frac{3\ell}{2\ell + 1} \cdot \left(1 - \frac{N_{\nu g_{7/2}}}{8}\right) \cdot N_{\pi g_{9/2}} \quad (1.12)$$

with the occupation number of the corresponding orbitals  $N$  and the angular momentum  $\ell$ . Regarding  $^{100}\text{Sn}$ , this expression serves as a reference number  $\mathcal{B}_{\text{GT}}^{\text{ESM}} = 17.78$  with  $\ell = 4$ , the number of protons in the  $\pi g_{9/2}$ -shell  $N_{\pi g_{9/2}} = 10$  and the number of neutron

states available in the  $\nu g_{\pi 7/2}$ -shell  $N_{\nu g_{\pi 7/2}} = 8$ . Deviations from this value are interpreted in terms of  $pn$ -interactions, particle-hole excitations, pairing correlations, tensor forces and the core polarization.

In comparison with the experimental values known from literature  $\mathcal{B}_{\text{GT}}^{\text{lit}} = 5 - 10$ , this value is too large by a factor of  $\sim 2 - 3$  ( $\rightarrow$  Cpt. 4). Therefore, a hindrance factor  $h = \mathcal{B}_{\text{GT}}^{\text{exp}}/\mathcal{B}_{\text{GT}}^{\text{mod}}$  was introduced which is the ratio of the experimental strength and the strength calculated according to a nuclear model. This model is oversimplified because further  $1^+$ -states, calculated by large-scale shell model (LSSM) calculations, contribute to the Gamow-Teller strength and pairing correlation as well as the *core polarization* results in a remarkable reduction of the transition strength [Tow85]. In the case of  $^{100}\text{Sn}$ , Brown and Rykaczewski [BR94] have already shown that the transition strength is reduced to 80% when applying a model space which considers 2-particle 2-hole ( $2p2h$ ) excitations when further  $1^+$ -states exist. Modern LSSM calculations in the gds harmonic oscillator shell performed by Caurier et al. [Cau+05] confirm these results and yield  $\mathcal{B}_{\text{GT}}^{\text{mod}} = 8.19$ . These calculations considered up to five particle-hole excitations and the strength was renormalized to take into account correlations beyond the gds-shell. In another LSSM calculation [Hin+12]  $\mathcal{B}_{\text{GT}}^{\text{mod}} = 9.1$  was obtained and a reduction of  $\mathcal{B}_{\text{ext}}^{\text{exp}}$  by 16% is reported if the first four excited  $1^+$ -states are accessible within the  $Q_{\beta}$ -window but not observed due to small branching ratios. The last contribution, which leads to a reduction of the  $\mathcal{B}_{\text{GT}}$ -value, originates from virtual excitations of the  $\Delta$ -resonances [Ari+01]. Here, further excited  $1^+$ -states up to 300 MeV contribute to the transition strength but cannot be observed within the energy window of the  $\beta$ -decay. Hence, the apparent hindrance of the  $\beta$ -decay has vanished as larger model spaces could be calculated and agreement between experiments and calculations was found. However, the uncertainties in the experimentally derived  $\mathcal{B}_{\text{GT}}$ -value is still too large to allow for a discrimination between different model predictions which is the motivation for the experiment described in this thesis. Experimentally, the  $\mathcal{B}_{\text{GT}}$ -value is determined by the relation

$$f(Z, Q_{\beta}) \cdot T_{1/2} = \mathcal{K} \frac{\ln(2)}{g_V^2 |\mathcal{M}_{\text{F}}|^2 + g_A^2 |\mathcal{M}_{\text{GT}}|^2} \quad (1.13)$$

with the phase space factor  $f$  and the half-life  $T_{1/2}$  on the left side as well as the square matrix elements of the Fermi and Gamow-Teller transitions and the corresponding coupling constants  $g_V$  and  $g_A$ . The determination of the  $Q$ -value of the decay is the most important part of the analysis because the phase space integral in Equation (1.9) evolves with the fifth power of the energy. In case of  $^{100}\text{Sn}$  the  $\mathcal{M}_{\text{F}}$  vanishes because there is no allowed state in  $^{100}\text{In}$  to occur within the  $Q_{\beta}$ -window for the Fermi transition. Hence, it has to be certainly known which fraction of the  $\mathcal{B}_{\text{GT}}$  is accessible using  $\beta$ -spectroscopy with regard to conclusions on the interactions applied in shell model calculations ( $\rightarrow$  Fig. 1.4). Also, the sensitivity limit of the experiment has to be prop-

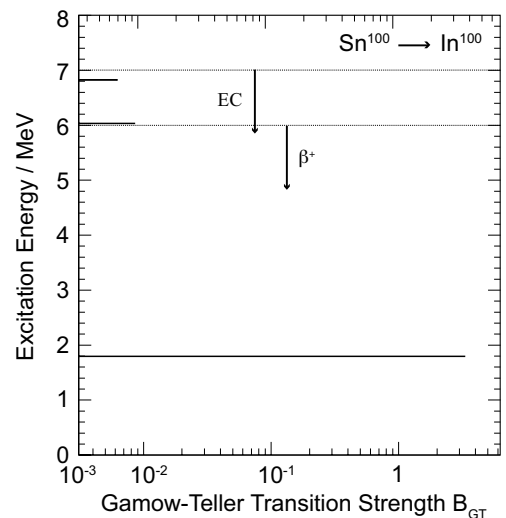


**Figure 1.4:** Fragmentation of the Gamow-Teller transition strength in the  $\beta$ -decay of  $^{100}\text{Sn}$  according to Brown and Rykaczewski [BR94].

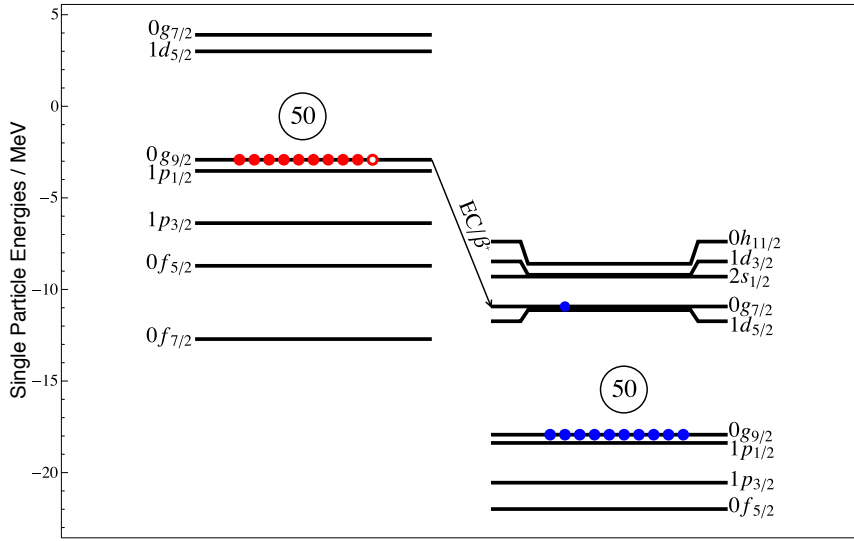


**Figure 1.5:** Shell structure around the double shell closure at  $N=Z=50$  with the occupancy of the  $\pi g_{9/2}$  and  $\nu g_{9/2}$  shells in the  $\beta^+$ -decay of  $^{100}\text{Sn}$  as predicted by Grawe et al. [Gra+95].

erly known in order to understand which part of the Gamow-Teller distribution has been observed. Transitions to different final states are distinguished by selective  $\gamma$ -emission. If these transitions are too weak to be observed, a part of the  $\mathcal{B}_{\text{GT}}$  remains hidden although it possibly contributes a large fraction to the transition strength. Since shell model calculations of  $^{100}\text{Sn}$  show that the dominant part in the  $\mathcal{B}_{\text{GT}}$  originates from the transition to the spin-orbit partner in the  $\beta$ -decay, the strength contained below the sensitivity limit is negligible in first order and the nucleus enables to study the Gamow-Teller transition strength to great accuracy as very little fragmentation occurs compared to other nuclei (e. g.  $^{98}\text{Cd}$ ) [BR94; Hin+12]. The determination of the Gamow-Teller transition strength and the detailed analysis of  $^{100}\text{Sn}$  are discussed in Chapter 4.

## 1.4 The Superaligned Fermi Decay

Besides the Gamow-Teller transition discussed in the previous section, Superaligned Fermi decays occur in the region of  $^{100}\text{Sn}$  as the  $N=Z-1$  nuclei and  $N=Z$  nuclei can decay into their isobaric analogue states. The nucleus with larger  $Z$  usually has the larger mass. Therefore, the Superaligned Fermi transitions are only possible in  $\beta^+$ /EC decays. The nuclear spin does not change and the  $\log(ft)$ -values of Superaligned  $0^+ \rightarrow 0^+$ -transition are very small ( $\sim 3.5$ ) due to a very large overlap of the wave functions of the initial and final states. For this reason the transitions are termed *Superaligned Fermi decay* ( $\rightarrow$  Fig. 1.3). The study of nuclei undergoing these transitions is directly related to the testing of the conserved-vector-current (CVC) hypothesis. In particular,  $0^+ \rightarrow 0^+$ -transitions are only mediated by the vector coupling  $g_V$  which is connected to the first element of the Cabibbo-Kobayashi-Kaskawa matrix (CKM-matrix) by the ratio [HT15]

$$|V_{ud}| = \frac{g_V}{G_{\text{F}}} = 0.97417(21) \quad (1.14)$$

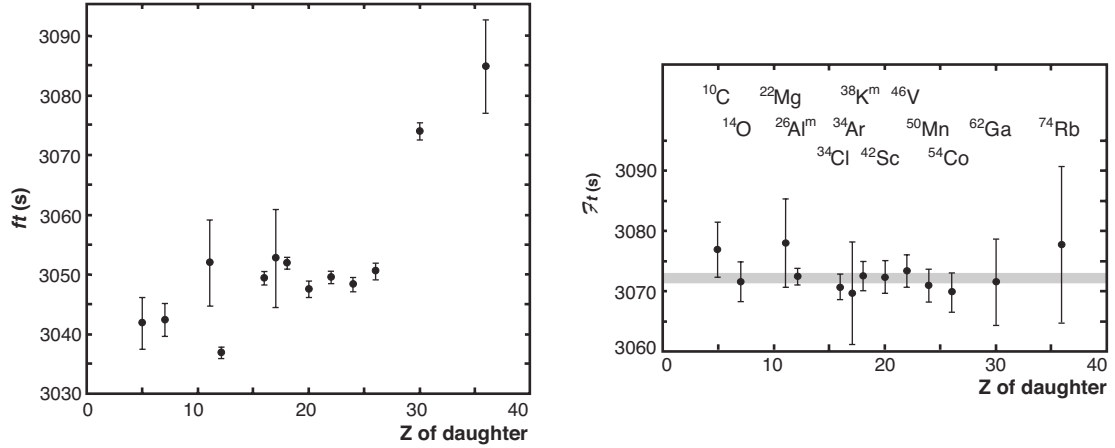


**Figure 1.6:** Comparison of  $ft$ -values with the charge and radiative corrected  $\mathcal{F}t$ -values [HT15]. After the corrections, the conserved-vector-current theory reveals to be true on the 0.06% confidence level. The gray layer marks the mean value with its uncertainties of  $\mathcal{F}t = 3072.27 \pm 0.72$  s.

with the weak-coupling constant and the Fermi-constant  $G_F/(\hbar c)^3 = 1.16637 \cdot 10^{-5} \text{ GeV}^{-2}$  which is known from the muon-decay  $\mu^- \rightarrow e^- + \bar{\nu}_e + \nu_\mu$ . In order to derive  $V_{ud}$ , the test of the CVC is very important because it confirms that  $g_V$  is constant. If the matrix element of  $0^+ \rightarrow 0^+$ -transitions of different nuclei does not vary much, the variation in the observations has to be explained by a renormalized coupling constant or further corrections. Since 1989, Hardy et al. [Har+90] have extensively studied charge-dependent and radiative corrections. Then, the corrected  $ft$ -values  $\mathcal{F}t$  are written as

$$\mathcal{F}t = ft(1 + \delta_R)(1 - \delta_C) = \frac{C \ln 2}{g_V^2(1 + \Delta_\beta)} \quad (1.15)$$

The term  $\delta_C$  originates from the charge-dependence of the phase space of the matrix element. The radiative corrections are split into one part  $\Delta_\beta$  which depends on the model of the weak interaction and is independent of the nucleus referred to as the inner corrections. The second part, denoted as  $\delta_R$ , varies from nucleus to nucleus and is referred to as the outer term. Hence, the  $\mathcal{F}t$ -values are the actual measures which have to be compared to test the CVC-hypothesis and the results of the recent survey by Hardy and Towner [HT15] are shown in Figure 1.6. Out of twenty known Superallowed Fermi decays, thirteen decays have reasonable uncertainties regarding the determination of  $\mathcal{F}t$  and it yields  $\mathcal{F}t = 3072.27 \pm 0.72$  s in their analysis. On the level of this accuracy,  $g_V$  is constant and  $V_{ud}$  is correctly determined by Equation (1.14). With the matrix elements  $V_{us}$  and  $V_{ub}$  a test of the unitarity of the CKM matrix reveals  $|V_{ud}|^2 + |V_{us}|^2 + |V_{ub}|^2 = 0.99978 \pm 0.00055$ . Hence, unitarity is satisfied on the 0.06% confidence level. The determination of  $\mathcal{F}t$ -values was performed up to  $^{74}\text{Rb}$ . The decays from the region of  $^{100}\text{Sn}$  have not been considered yet because half-lives and  $Q$ -values could not be determined precisely due to small production cross sections. Therefore, the present experiment also contributes to expand the test of the CVC hypothesis to heavier nuclei. In this thesis, the nuclei  $^{90}\text{Rh}$ ,  $^{94}\text{Ag}$  and  $^{98}\text{In}$  are discussed which proceed by Fermi-decays as the unpaired nuclei couple to form a ground state with spin-parity  $0^+$ . In contrast, the isomeric states proceed by the Gamow-Teller decay. Due to the fragmentation of the  $\beta$ -decay of these nuclei, a detailed study of the branching ratios is required in order to derive the transition strength according to Equation 1.13. The corresponding analysis and results of these nuclei is presented in detail in Chapter 4.

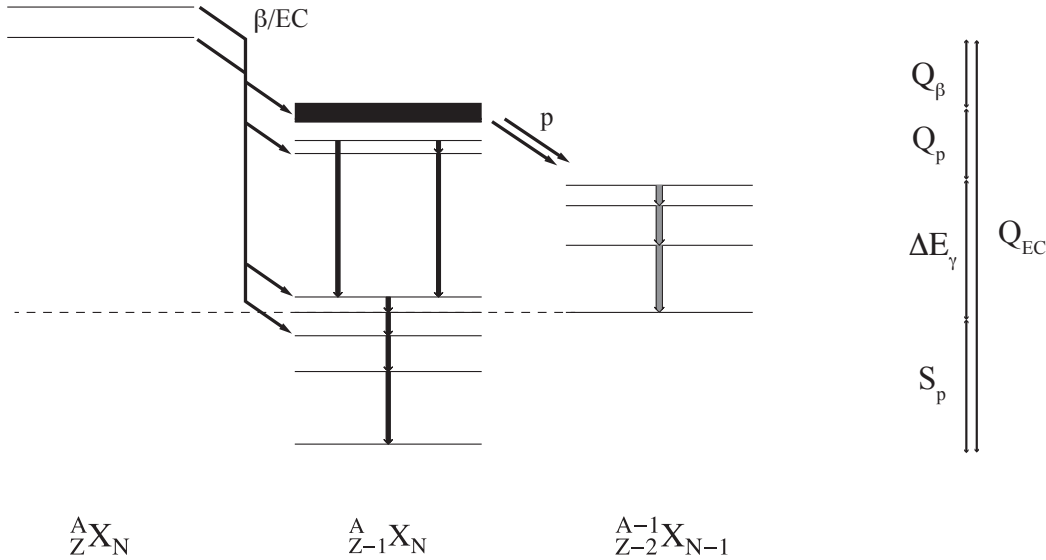


**Figure 1.7:** Schematic of the  $\beta$ -delayed proton decay. The parent nucleus decays into high-lying states at a high level density via  $\beta^+$ /EC-decay which are well-above the proton separation energy.

## 1.5 $\beta$ -Delayed Proton Emission and Direct $p$ -Decay

Approaching the proton dripline, there are more relevant decay processes besides  $\beta^+$ /EC. In this region, the direct proton decay occurs if there are accessible states well above the proton separation energy  $S_p$  but sufficiently low to be compensated by the Coulomb barrier and centrifugal barrier ( $\sim 600$  keV). This decay channel competes with the  $\gamma$ -emission from excited states or  $\beta$ -decay. Direct proton and two-proton decay was reported for  ${}^{94}\text{Ag}$  [Muk+06b] and is also investigated in this work.

States above the proton separation energy are also populated through the  $\beta^+$ /EC-decay to high-lying states (hs) with  $E_{\text{hs}} > S_p$  in its daughter nucleus (e. g.  ${}^{90}\text{Rh}$ ,  ${}^{94}\text{Ag}$ ,  ${}^{98}\text{In}$ ). Subsequently, the daughter nucleus decays by proton emission. In the case of the region around  ${}^{100}\text{Sn}$ , this decay channel benefits from the decreasing separation energies and increasing energy release in  $\beta$ -decays. Starting from the  $N = Z$ -line all nuclei towards the proton dripline show  $\beta$ -delayed proton emission ( $\beta p$ -channel). The  $\beta p$ -branching ratios for  $N = Z$  and  $N = Z - 1$  nuclei are determined within the framework of this thesis while an extended compilation of branching ratios for the region of  ${}^{100}\text{Sn}$  has been reported by Lorusso et al. [Lor+12]. The energy distribution of protons from the  $\beta p$ -channel is quasi continuous since the transitions occur between many states as nuclei with large  $A$  show high level densities at high energies. Specifically, the  $\beta p$ -channel is used to infer the energy spacings between the ground state and the isomeric state of  ${}^{98}\text{In}$  as shown in Figure 1.7. If each term is measured or known in literature, the energy level of the parent state follows by the sum  $Q_\beta + Q_p + \Delta E_\gamma + S_p$ . The analysis and derivation of each term is explained in detail in Chapter 4.

Eventually, the  $\beta p$ -channel contributes to the rapid-proton capture process (rp-process) as it adds another decay channel to a nucleus which alters the evolution of the elemental abundances being particularly interesting for the waiting point nuclei.

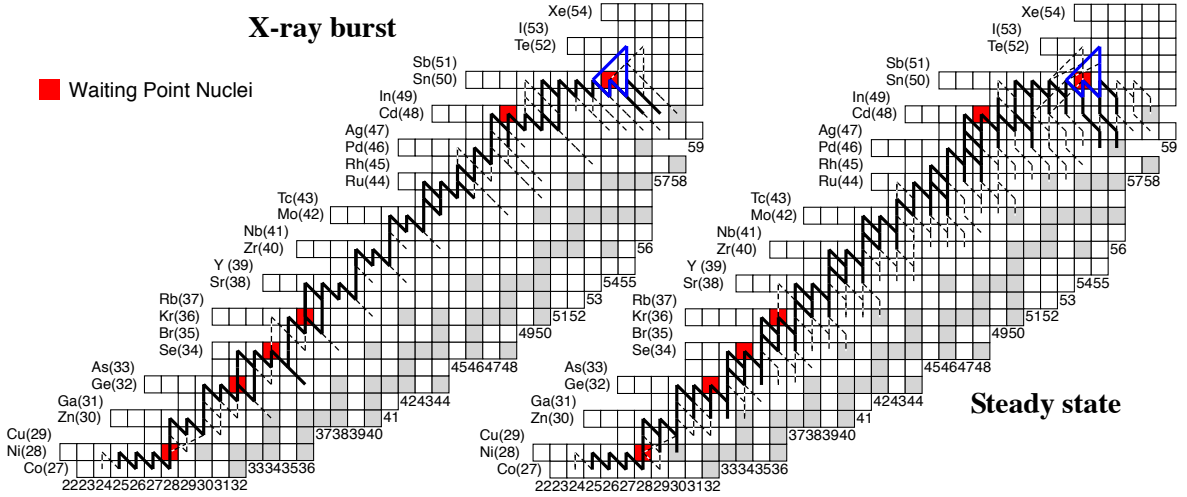


**Figure 1.8:** The rapid-proton capture process within the nuclear chart and its endpoint according to Schatz et al. [Sch+01]. The path ends in the SnSbTe-circle due to the  $\alpha$ -unbound  $^{106-109}\text{Te}$ . It proceeds along the  $N=Z$ -line close to the proton dripline. The path depends on the astrophysical site. The bold black line marks the main path of the rp-process. The blue circular shape marks the SnSbTe-cycle.

## 1.6 The rp-Process

The *rp*-process was introduced to explain the elemental abundances on the proton-rich side in analogy to the *s*- and *r*-process of neutron-rich nuclei [WW81]. It proceeds along the  $N=Z$ -line close to the proton dripline and the process itself starts with the accretion of hydrogen and helium rich matter onto neutron stars in X-ray binaries. These objects were discovered in 1976 and they provide the astrophysical conditions such that X-ray bursts can proceed.

Thus, the most likely astrophysical sites for explosive hydrogen burning are novae and X-ray bursts [FGG13] in accreting binary systems with one neutron star. The X-ray bursts are triggered in two different scenarios: 1) due to extremely sensitive fusion reactions that the rise in temperature cannot be compensated by readjusting the stellar structure or surface cooling resulting in a thermonuclear runaway which is observed for 10 s to 100 s by its X-ray bursts, 2) by the temperature sensitivity of the helium burning in systems with low accretion rates of a mixture of hydrogen, helium and metal in solar abundances. This ignites hydrogen burning through the *rp*-process while the *rp*-process itself needs high temperatures ( $\sim 10^9$  K) for the protons in order to be able to overcome the Coulomb barrier.

High temperature allows for a rapid proton capture ( $p, \gamma$ ) which is faster than the  $\beta$ -decay. The *rp*-process continues until ( $p, \gamma$ ) and photo-disintegration ( $\gamma, p$ ) are in equilibrium. At this point nuclei need to wait for subsequent  $\beta$ -decay to continue, which are called *waiting points*. Therefore, during the X-ray burst, the vast majority of the mass is concentrated in a few important waiting points which are the reason that time scales of X-ray bursts go up to several 100 s. For instance, the reaction flow becomes very slow at the nuclei  $^{64}\text{Ge}$ ,  $^{68}\text{Se}$  and  $^{72}\text{Kr}$  where ( $\gamma, p$ ) reactions are likely to dominate and half-lives of  $\beta$ -decays are in the range of 17 s to 64 s which is long compared to the actual duration of the *rp*-process of about some tens of seconds [GLMP07; Sch+98a]. At this point, astrophysics and nuclear physics are very close because nuclear properties determine which

temperatures are necessary to trigger the process. Transition probabilities and  $Q_p$ -values of nuclear reactions determine how the rp-process and elemental abundances can evolve. Astrophysical network calculations consider more than 1000 reaction rates where the essential input parameters are the half-lives, nuclear masses and the proton separation energies where the masses should be known better than 10 keV [SR06]. Furthermore, Schatz et al. [Sch+98a] have shown that 2p-capture rates can significantly bypass the  $\beta$ -decay. For this reason, a detailed knowledge of the branching ratios of nuclear decay channels is necessary for reliable calculations. Finally, Schatz et al. [Sch+01] have shown that the rp-process ends in the SnSbTe-cycle independent from the initial conditions as the known ground state  $\alpha$ -emitters  $^{105-109}\text{Te}$  are unbound by 3.4 to 4.9 MeV [Sch+79; Lid+06]. The proton capture proceeds up to  $^{105}\text{Sn}$  via  $\beta$ -decay along  $Z = 50$  where the Sn-proton is sufficiently bound against  $(\gamma, p)$ . Antimony can only proceed further to  $^{106,107}\text{Te}$  which decays back to Sn. This cycle marks the end of the rp-process. The impact of uncertainties in the observables on the results of rp-process calculations was studied in order to find out which nuclei are most urgent to know in more detail. The results are tabulated in [Par+09; Ili+02]. In particular, the  $Q$ -values and half-lives are still not known sufficiently precise or nuclei have not been produced yet in the region of the endpoint of the rp-process. There are many open questions concerning the accuracy of the path of the rp-process such as the half-lives of  $N = Z - 1$  nuclei, the observation of the proton dripline, the branching ratios of decay channels, the accuracy of the half-lives in  $N = Z$  nuclei, the observation of a 2p-decay in  $^{94}\text{Ag}$  and the  $Q_p$ -values. In this work, the half-lives of  $N = Z - 1$  nuclei as well as the half-life of the interesting waiting point nucleus  $^{96}\text{Cd}$  are derived with higher precision than in previous works and the  $\beta p$ -channels are also investigated while new  $N = Z - 2$  isotopes towards the proton dripline has been discovered.

## 2 Experimental Setup

The experiment presented within this work was particularly designed with regards to study the properties of the doubly magic nucleus  $^{100}\text{Sn}$  and the nuclear structure of neighboring nuclei. The experiment was performed at the RI Beam Factory (RIBF) [Yan07] of the RIKEN Nishina Center in Japan in 2013 from June 15th to June 25th using a total beam-on-target time of 8.4 days. A short test was performed [Suz13] to demonstrate the feasibility and to verify the proposed production cross sections. Due to an intense period of accelerator development at the RIBF facilities, a  $^{124}\text{Xe}$  beam with extremely high intensity of up to 36 pA could be used.

The primary beam was generated with a superconducting electron cyclotron source. Here, Xe-ions reach a high charge state, so that they can be accelerated with a linear accelerator after extraction from the source. Then, the ions are further accelerated by a boosting system of four sector cyclotrons and the final energy of 345 AMeV is reached in the SRC cyclotron while the charge-state is further increased using two strippers between the RRC and IRC cyclotrons up to  $^{124}\text{Xe}^{52+}$ . The secondary beam which is composed of a cocktail of exotic nuclei in the region of  $^{100}\text{Sn}$  was generated by projectile fragmentation of a stable primary  $^{124}\text{Xe}$ -beam bombarding a 4-mm thick  $^9\text{Be}$ -target. Eventually, the fragments were well-separated and identified by means of the BigRIPS separator before being implanted into the WAS3ABi/EURICA detector arrays where spectroscopy was performed with Si(Li)-, High Purity Ge- and LaBr(Ce)-detector arrays.

### 2.1 The RI Beam Factory

Projectile fragmentation is a method to generate exotic nuclei from a stable primary beam which is used at several facilities such as GANIL [Lew+94], GSI [Str10], NSCL [Baz+08] and RIBF. The RIBF is the state-of-the-art facility for the acceleration of heavy ions with the highest intensities. In the present experiment, the average beam intensity was 30 pA with a maximum of 36 pA while the primary beam energy was 345 AMeV.

Secondary beam particles, which are generated from projectile fragmentation, nearly preserve the velocity of the incoming beam which allows for a clear event-by-event identification.

An overview schematic of the RIBF accelerator complex is shown in Figure 2.1. The production of the primary beam starts with a super conducting electron cyclotron resonance (SC-ECR) ion source. The  $^{124}\text{Xe}$  ions are extracted by injecting microwaves at 28 GHz followed by an acceleration with the linear accelerator RILAC after. Then, the beam enters a boosting system which consists of four sector cyclotrons (RRC, fRC, IRC and SRC). While passing from RRC to IRC, a He gas-stripper and a thick air gas stripper are placed between the cyclotrons to remove the electrons [Ima+14]. After, the beam is accelerated to its final energy in the superconducting cyclotron (SRC) before

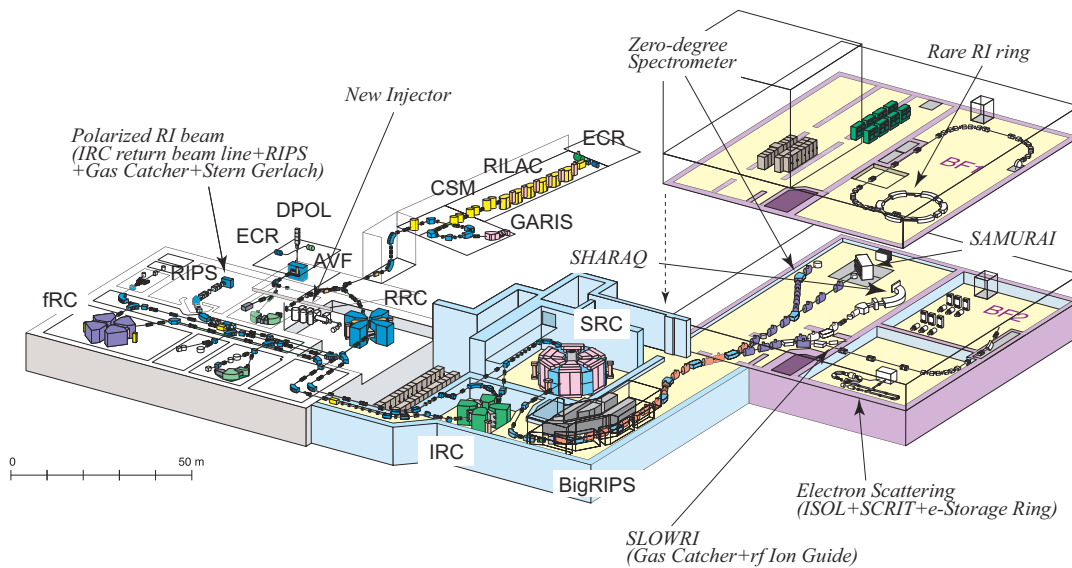


**Figure 2.1:** Bird's eye view of the RIBF facilities at the RIKEN Nishina Center [Yan04]. The beam production starts with the ion extraction at the SC-ECR ion-source passing a boosting system until products of projectile fragmentation are implanted into the EURICA/WAS3ABi spectrometer located at the final focus of the Zero degree spectrometer.

impinging the production target. This system of cyclotrons can be operated in different modes in order to serve experiments with fixed (mode 1) or variable (mode 2) energies as well as for experiments with deuterons (mode 3). Here, the accelerators were used in mode 1 and the configuration is shown in Figure 2.2.

### 2.1.1 The Production Mechanism

The fragmentation of nuclei is described as an inelastic scattering process in a two step model [Ser47; Rei94]. In the macroscopic *abrasion-ablation* model according to Gaimard and Schmidt [GS91], the regions of participating nucleons of the projectiles and the target as well as the non-participating nucleons of the reaction are geometrically separated into overlapping and non-overlapping regions which are called participators and spectators, respectively. The number of removed nucleons by the abrasion process depends only on the impact parameter for a specific projectile-target combination which can be calculated by a numerical integration of the overlap volume [GS91] according to the description by Morrissey et al. [Mor+78] and Oliviera et al. [Oli+79]. The abrasion model only specifies the number of removed nucleons rather than the proton-to-neutron ratio of the pre-fragments<sup>1</sup>.

Hereafter, the pre-fragment de-excites in a statistical evaporation cascade where light-particles as protons, neutrons, deuterons and alpha particles are emitted as long as the residual nucleus remains in an excited state which is below the corresponding particle separation energy. This emission of light particles which have the correct magnetic rigidity to pass until the implantation detectors is another source of background as discussed

<sup>1</sup>Pre-fragment prescribes a fragment in an excited state after the fragmentation reactions in the target.

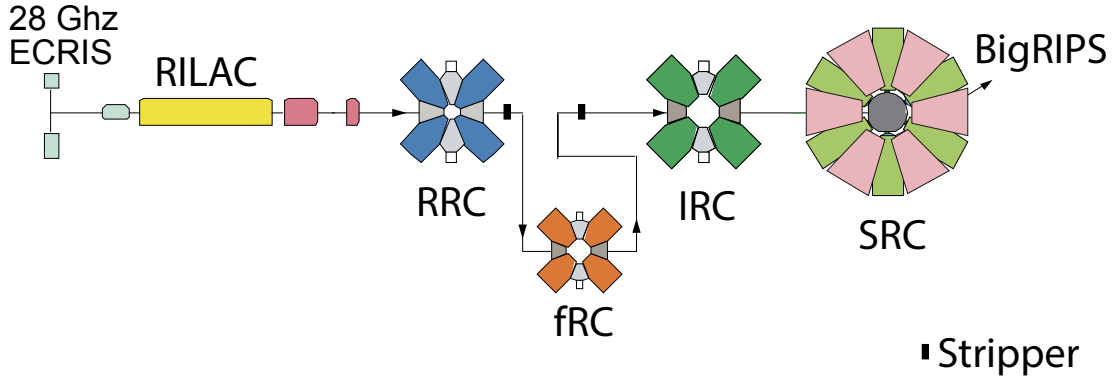


**Figure 2.2:** Schematic of the RIBF configuration of the present experiment generating a primary beam of 345 AMeV taken from [Yan04]. The production starts with an ion source ECRIS. The extracted ions are accelerated by the linear accelerator RILAC and a sequence of four sector cyclotrons before the beam is delivered to the BigRIPS separator.

in Section 2.4.1 and results in a contribution to the background rate of Si-detectors. The mean number of nucleons which are released in one evaporation step is  $\frac{8}{5}$  with an average reduction of excitation energy of 20 MeV per step [CH81; GS91].

The production cross section becomes energy-independent as the projectile energy is much larger than the Fermi energy ( $\approx 40$  AMeV). Beam energies above 100 AMeV are desirable because the fraction of bare nuclei which are produced in the target becomes maximized such that a clear separation is feasible reducing the contamination by the hydrogen-like neighboring isobar with one electron and resulting in a clean PID [FGG13]. The isobaric distribution of the fragments is Gaussian with a steeper slope to the neutron-deficient side. If the mass loss of nuclei is larger than 15-20% compared to the projectile, the isotopic distribution is mainly independent of the projectile nucleus referred to as the residue corridor. On the other hand, the isotopic distribution of nuclei is close to the mass number of the projectile with a small variance and a continuous transition to the residue corridor for small mass losses [SB+00]. The state-of-the-art method of calculating production cross sections is the universal empirical parametrization EPAX [Sü12; Sü+90] where the parameters are adjusted such that the measured cross sections are reproduced. Regarding these properties of the projectile fragmentation, the neutron-deficient nuclei  $^{112}\text{Sn}$  and  $^{124}\text{Xe}$  are the most suitable isotopes for the use as primary beams for the production of  $^{100}\text{Sn}$ . In previous experiments at GSI<sup>2</sup>, both isotopes were used.  $^{124}\text{Xe}$  was focused on a  $^9\text{Be}$  target and  $^{112}\text{Sn}$  was focused on a  $^{22}\text{Na}$  target [Sch95a; Sto02; Hin+12]. The production cross sections were measured as  $\sigma = 11.0(46)$  pb,  $\sigma = 1.8_{-1.3}^{+3.2}$  pb and  $\sigma = 5.8(21)$  pb with respect to the references. Another two experiments using  $^{112}\text{Sn}$  as primary beam have been performed at MSU<sup>3</sup> and GANIL<sup>4</sup> using a Be- or Ni-target and the cross sections were reported to  $\sigma = 0.25(15)$  pb and  $\geq 120$  pb, respectively.

<sup>2</sup>GSI Helmholtzzentrum für Schwerionenforschung, Germany

<sup>3</sup>Michigan State University, USA

<sup>4</sup>Grand Accélérateur National d'Ions Lourds, France

## 2.2 The Fragment Separator BigRIPS

Many fragments are produced in the collisions inside the target. Efficient and high-resolution fragment separation and selection is essential to not exceed the rate capability of the beam-line detectors regarding the particle identification and also to optimize the correlation efficiency of the implantation detectors described in Section 2.4.1. Nuclei are separated using the two-stage RI beam separator BigRIPS ( $\rightarrow$  Fig. 2.3) which is a magnet separator with a length of 78.2 m, an angular acceptance of  $|\Delta\theta| < 40$  mrad (horizontally) by  $|\Delta\phi| < 50$  mrad (vertically), and a momentum acceptance of  $|\Delta P|/P < 3\%$  [Kub+12]. The basic characteristics of the BigRIPS separator are summarized in Table 2.1.

The first stage of the separator ( $\rightarrow$  Fig. 2.3), which is the part starting at the production target until the focal plane F2, serves isotopic separation by using the dispersion-matching technique. It consists of four superconducting quadrupole triplets (STQ) and two room-temperature dipole magnets (RTD). An achromatic wedge-shaped Al-degrader, which is momentum-dispersive, is placed at the focal plane F1 (between two STQs) where isotopes are separated according to their energy loss in matter and their mass-to-charge ratios. STQs are ion optical elements which are used to focus the divergent beam of charged ions and RTDs are used to select the magnetic rigidity of the fragments of interest. The method which is used for the separation according to the mass-to-charge ratio  $A/Q$  and energy loss  $\Delta E$  in matter is referred to as the standard  $B\rho$ - $\Delta E$ - $B\rho$ -method [Gei+92]. The separation proceeds basically in three steps. In an RTD, which is placed in front of the degrader, particles pass the magnetic field according to their  $A/Q$ -ratios while further separation by energy loss is achieved passing an Al-degrader. In first order, the energy loss of charged particles depends on the incident velocity ( $\Delta E \propto \frac{1}{\beta^2}$ ) and the nuclear charge  $Z$  ( $\Delta E \propto Z^2$ ). The latter dependence causes a separation in momentum so that nuclei with a specific  $Z$  can be selected by adjusting the magnetic rigidity in the second RTD which is located behind the degrader. Thus, a momentum separation transforms the  $Z$ -dependence and energy-dependence of the energy loss  $\Delta E$  in the degrader into a spatial separation by the RTDs. As the beam is bent by the two RTDs, isotopes with different  $A/Q$ , momenta  $P = M \cdot v$ , the nuclear mass  $M = m_0 \cdot A$  and charge  $Q$  moving in a magnetic field  $\mathbf{B}$  on a track of radius  $\rho$ , the magnetic rigidity  $B\rho$  is given by

$$B\rho = \frac{P A}{A Q} = c \cdot m_0 \cdot \frac{\beta}{\sqrt{1 - \beta^2}} \cdot \frac{A}{Q} \quad (2.1)$$

where  $m_0$  is the mass of a nucleon in the rest frame and  $\beta$  denotes the velocity  $v/c$  with the speed of light  $c$ . Therefore, different slit configurations were used during the experiment to focus on exploring the proton dripline in the end of the experiment when a few counts of  $N = Z - 2$  nuclei have already been detected. The magnetic rigidity is experimentally determined with trajectory reconstruction by measuring positions and angles of the particles before and after the RTDs with PPAC<sup>5</sup> detectors.

The second stage, which refers to the range between the focal planes F3 and F7, is designed for the particle identification ( $\rightarrow$  Fig. 2.3). Additionally, further separation

<sup>5</sup>Parallel-Plate Avalanche Counter (PPAC) detectors consist of an anode plane at its center surrounded by two cathode planes defining the XY-coordinates. The detector gas is octafluoropropane  $C_3F_8$  and the design is according to Kumagaia et al. [Kum+01].

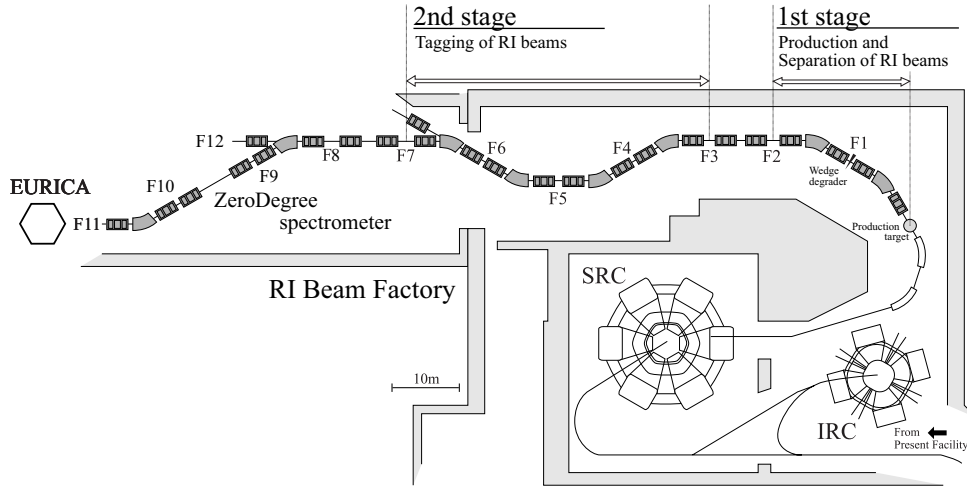


**Figure 2.3:** Schematic of the BigRIPS separator. The focal planes are labeled by „F“. The first stage serves beam separation with a wedge-shaped degrader right after F1. The second stage and the ZeroDegree spectrometer serve particle identification. The schematic is taken from Aoi [Aoi06].

is performed by another wedge-shaped degrader which was placed at the momentum dispersive focal plane F5 referring to the name of the method as tandem  $B\rho\text{-}\Delta E\text{-}B\rho$  separation. The degrader thicknesses were 2.84 mm and 2.17 mm for the central track corresponding to 714.1 mg/cm<sup>2</sup> and 587.3 mg/cm<sup>2</sup> at F1 and F5, respectively. The optimum thicknesses were determined by the maximum transmission and the optimal beam purity according to LISE++ calculations [TB08] which simulate the complete beam-line from the production target until the implantation detectors. The second stage of the BigRIPS separator, which consists of 8 STQs and 4 RTDs, is operated such that the beam is achromatic in the focal plane F7. The focus of the beam was also monitored with PPAC detectors here. The magnetic rigidity  $B\rho$  was determined by measuring positions and angles in each of the focal planes F3, F5 and F7 and a tilted electrode gas ionization chamber (TEGIC) was placed to perform energy loss measurements in the last focal plane F11 before implantation.

horizontal angular acceptance $\Delta\theta$ [mrad]	$\pm 40$
vertical angular acceptance $\Delta\phi$ [mrad]	$\pm 50$
momentum acceptance $\delta$ [%]	$\pm 3$
$P/\Delta P$ (1st)	1260
$P/\Delta P$ (2nd)	3420
Max. $B\rho$ [Tm]	9.5/8.8
Length [m]	78.2

**Table 2.1:** Basic parameters of the BigRIPS separator [Kub+12].

## 2.3 Particle Identification

Regarding the spectroscopy ( $\rightarrow$  Cpt. 4) of nuclei, a unique event-by-event identification is necessary in order to perform a proper event selection and study the decay radiation correlated with a particular implantation event. The particle identification (PID) was performed in the second stage of the BigRIPS separator ( $\rightarrow$  Fig. 2.3). In particular, as the experimental setup was focused on the most exotic species close to the proton dripline, production cross sections are small and a high resolution of the separator is necessary to minimize losses of nuclei by ambiguities in the identification of neighboring nuclei. Therefore, the ions have to be completely stripped to ensure that each species only occurs in a unique charge-state. Applying a beam energy of 345 AMeV, nearly  $\sim 100\%$  of the nuclei are completely stripped [Sch+98b]. Considering proton-rich nuclei, contaminants which contribute to a certain PID are even more exotic so that there is little effect on the PID in this region since the production cross sections of these contaminants are strongly suppressed. Then, a unique identification of each species is achieved in terms of the mass-to-charge ratio  $A/Q$  and the nuclear charge  $Z$  ( $\rightarrow$  Fig. 2.5). Both quantities are derived by using the  $B\rho$ - $\Delta E$ -TOF scheme

$$\text{TOF} = \frac{L}{\beta c} \quad (2.2)$$

$$\frac{A}{Q} = \frac{B\rho}{\beta\gamma} \frac{c}{m_u} \quad (2.3)$$

$$\frac{dE}{dx} = \frac{4\pi e^4 Z^2}{m_e v^2} N z \left[ \ln \frac{2m_e v^2}{I} - \ln(1 - \beta^2) - \beta^2 \right] \quad (2.4)$$

where the time-of-flight (TOF) between the focal planes F3 and F7 with a distance of  $L = 46.6$  m is used to determine the velocity  $v$  of the particles. The TOF is measured with plastic scintillators in these focal planes. In practice, the correct measurement of the TOF was checked by the sum of  $\text{TOF}_{35}$  and  $\text{TOF}_{57}$  by using the timing signal of the PPAC in F5. Furthermore,  $c$  denotes the speed of light,  $\beta = \frac{v}{c}$  with the velocity  $v$ ,  $\gamma = \frac{1}{\sqrt{1-\beta^2}}$ ,  $I$  is the ionization potential,  $m_u$  the atomic mass unit,  $m_e$  the electron mass and  $e$  the elementary charge. The ratio  $A/Q$  is experimentally determined by measuring the deviation of the particle trajectory from the central track  $\delta_{35}$  with the radius  $\rho_0$  in the focal planes F3, F5 and F7.

$$B\rho = B\rho_0(1 + \delta_{35}) \quad \text{with} \quad \delta_{35} = \frac{B\rho - B\rho_0}{B\rho_0} \quad (2.5)$$

with the relation for the section between F5 and F7, correspondingly. Equivalently, these indices denote the part of the separator where the observables have been measured in the forthcoming. The relation in Equation (2.5) allows for trajectory reconstruction by ion-optical transformations if the position and the angle relative to the central track are known in the initial and final focal plane. The relation between the magnetic rigidity, the position and angular measurements at a focal plane, which is achromatic in y-direction and dispersive in x-direction, is given by

$$B\rho = B\rho_0 \left( 1 + \frac{x_5 - (x|x)x_3 - (x|\theta)\theta_3}{(x|\delta)} \right) \quad (2.6)$$

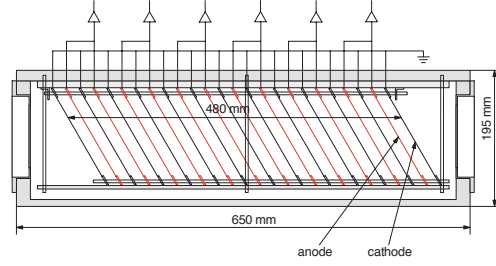


**Figure 2.4:** Schematic of the multi-sampling ionization chamber at F11 which was user for the determination of the nuclear charge  $Z$ . Twelve anode (red) and thirteen cathode (black) planes in a distance of 20 mm. The chamber is filled with the detector gas Ar – CF<sub>4</sub> and the electrodes consist of a conductive 4  $\mu\text{m}$ -thick mylar aluminized foil. [Kim+05]

with the transfer matrix elements  $(x|x)$ ,  $(x|\theta)$  and  $(x|\delta)$  representing the image magnification, the angular dependence and the momentum dispersion, respectively, which are derived experimentally by the correlations of positions, angles and the TOF. The  $x_i$  and  $\theta_i$  denote the positions and inclination angles in the focal planes, correspondingly. In coherence with the measurement of the magnetic field  $\mathbf{B}$  with hall probes and the radius  $\rho$  of the central particle track which is given by the geometry of the RTDs, the mass-to-charge ratio  $A/Q$  is derived according to Equation (2.1).

After, the nuclear charge is determined by the relation with the energy loss  $\Delta E$  according to the Bethe-Bloch formula ( $\rightarrow$  Eqn. (2.4))

$$Z = C_1 v_{57} \sqrt{\frac{\Delta E}{\ln \frac{2m_e v_{57}^2}{I} - \ln(1 - \beta_{57}^2) - \beta_{57}^2}} + C_2 \quad (2.7)$$

where the constants  $C_{1,2}$  denote two empirically determined calibration constants [Fuk+13]. The energy loss measurement was performed by the TEGIC detector which was placed in the focal plane F11, designed according to Kimura et al. [Kim+05]. It consists of twelve anode planes and thirteen cathode planes, made of conductive mylar aluminized foils which are tilted with respect to the beam-line in order to prevent electrons and positive ions from recombination ( $\rightarrow$  Fig. 2.4). The result is a PID which allows to distinguish between different nuclei as shown in Figure 2.5 which is uniquely checked by well-known  $\gamma$ -emission from isomeric states of nuclei which are implanted in WAS3ABi/EURICA (e.g. <sup>98</sup>Cd). The focus was on the production of <sup>100</sup>Sn with a total number of 2525 identified nuclei so that the nuclei on the  $N = Z - 1$  line were also produced with much higher statistics ( $\geq 10$ ) compared to a previous experiment [Str10]. The  $N = Z - 2$  nuclei <sup>96</sup>In, <sup>94</sup>Cd, <sup>92</sup>Ag and <sup>90</sup>Pd were newly identified which has already been reported by Celikovic et al. [Cel+16]. In case of <sup>96</sup>In, the proton dripline was even crossed and <sup>98</sup>Cd was used for a benchmark test regarding the determination of half-lives and  $Q_\beta$ -values ( $\rightarrow$  Sec. 3.1.5, 3.4.3).

### Background Discrimination of the Particle Identification

Nuclear reactions, scatterings, signal pile-ups and improper detector response lead to improper identifications. Therefore, the consistency of the identification is checked by several correlations between position detectors, scintillation detectors and reconstructed trajectories according to Fukuda et al. [Fuk+13].

- The charge-integrated signals and the timing signals of both photo-multiplier tubes of each scintillation detector for the TOF measurement contain also the position

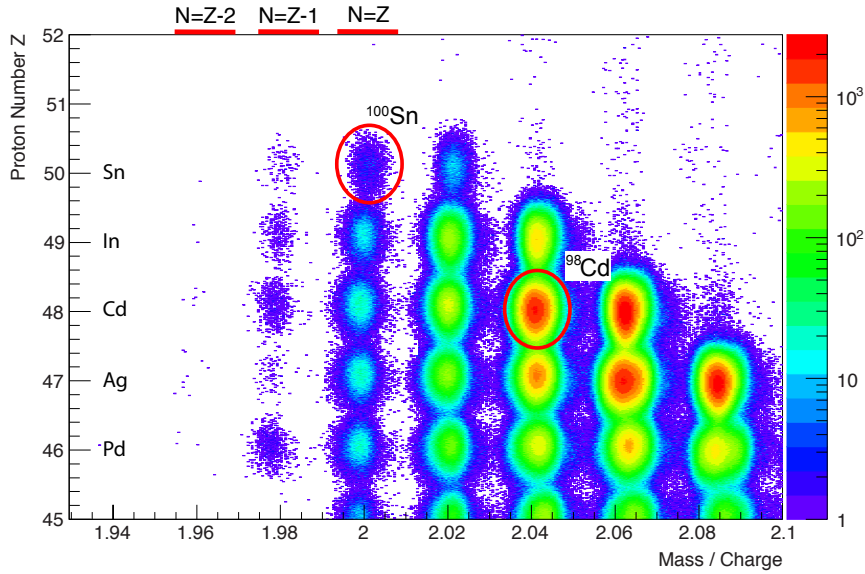


**Figure 2.5:** Particle identification (PID) plot of the present experiment. Encircled nuclei:  $^{100}\text{Sn}$  which has 2525 identified nuclei and one of the most abundant species,  $^{98}\text{Cd}$  ( $\sim 2.4 \cdot 10^6$ ) which was used for the efficiency calibration of the Ge-detectors, the benchmark test of the half-life fit and the verification of the  $\chi^2$ -method. The columns which are highlighted by the proton-to-neutron ratios are subject of this thesis.

information. This results in a linear correlation of the position between both signals.

- The charge-integrated signals of the scintillation detectors are checked for correlations to suppress events where nuclear reactions have occurred.
- The signals of neighboring anodes of the TEGIC detector as well as the correlation of the energy loss  $\Delta E$  in this detector and the charge-integrated signals from the scintillation detectors can identify nuclear reactions as well as pile-up events by the analysis of the pulse shape and the amplitude.
- The charge-states of the ions may change while passing detector matter or the Al-degraders. Therefore, the timing information of the PPAC at F5 is used to measure the TOF between F3 and F5 as well as between F5 and F7 which allow for a test whether the charge-state has changed after passing the degrader.
- Correlations of the magnetic rigidities  $B\rho_{35}$  and  $B\rho_{57}$  as well as between the time-of-flight  $\text{TOF}_{35}$  and  $\text{TOF}_{57}$  serve to clean up the PID as the fixed width of the degrader and the  $A/Q$  ratio defines the range of the  $B\rho$  and for the TOF.
- Multiple-hit events in PPAC detectors occur due to  $\delta$ -electrons as well as destruction or decay of the nucleus during the flight. These events are identified by timing signals of the PPAC detectors to either side of the delay line  $T_{1,2}$ . The sum of both  $T_{\text{sum}} = T_1 + T_2$  is a detector constant independent from the position such that a deviation from this sum indicates a multiple-hit event.
- The particle tracks are checked for their ion-optical consistency at different foci by checking correlations of positions and angles by means of the transfer matrix elements.

Cleaning up the PID according to these background contributions, a resolution of  $\Delta A=0.24$  (FWHM) and  $\Delta Z=0.47$  (FWHM) was obtained. Due to this resolution more than 98% of implanted nuclei are within an ellipse that does not overlap with the PID of a neighboring nucleus. The resolution of the  $A/Q$  was further improved by a slewing correction of the timing signals of the scintillation detectors which accounts for the timing jitter with  $t_{\text{corr}} = t + \tau_{\text{slew}}$  where  $t$  is the measured time. The delay  $\tau_{\text{slew}}$  originates from the use of leading-edge discriminators.

After the identification, the experimentally measured cross sections were determined. The production cross section of the nucleus  $^{100}\text{Sn}$  is  $(7.5 \pm 0.5 \pm 3.8_{\text{sys}}) \times 10^{-10}$  mb in the present experiment [Cel+16] which is in agreement with  $(7.4 \pm 1.7 \pm 3.7_{\text{sys}}) \times 10^{-10}$  mb of a similar setting used in the experiment by Suzuki [Suz13] ( $\rightarrow$  Fig. 2.6). Thus, Celikovic et al. [Cel+16] suggests a dependence on the energy or target thickness to explain the differences between the experiments at GSI and RIKEN ( $\rightarrow$  Sec. 2.1.1). The optimum target thickness regarding to maximize the production cross section and transmission of nuclei was determined by LISE++ calculations [TB08] which employ the empirical parameterization of production cross sections EPAX3.01 [Sü12]. The parameters have been adjusted in order to fit the experimental results by Hinke et al. [Hin+12] in this approach which accounts for secondary reactions. In the  $^{100}\text{Sn}$  setting, 69.5% of the generated  $^{100}\text{Sn}$ -isotopes could reach the WAS3ABi detector plane according to the LISE++-calculations. The comparison of the experimental results shows that the estimates from EPAX are consistent at  $N=Z$  and  $N=Z-1$  whereas deviations occur for  $N=Z-2$   $^{94}\text{Cd}$  and  $^{92}\text{Ag}$ . The production cross sections of  $N \leq Z$  nuclei are summarized in Figure 2.6.

Isotope	Cross section (mb)
$^{100}\text{Sn}$	$(7.5 \pm 0.5) \times 10^{-10}$
$^{99}\text{Sn}$	$(4.2 \pm 0.8) \times 10^{-11}$
$^{98}\text{In}$	$(13.7 \pm 0.3) \times 10^{-9}$
$^{97}\text{In}$	$(1.3 \pm 0.2) \times 10^{-10}$
$^{95}\text{Cd}$	$(1.0 \pm 0.1) \times 10^{-9}$
$^{94}\text{Cd}$	$(2^{+3}_{-1}) \times 10^{-11}$
$^{93}\text{Ag}$	$(3.3 \pm 0.2) \times 10^{-9}$
$^{92}\text{Ag}$	$(3^{+2}_{-1}) \times 10^{-11}$

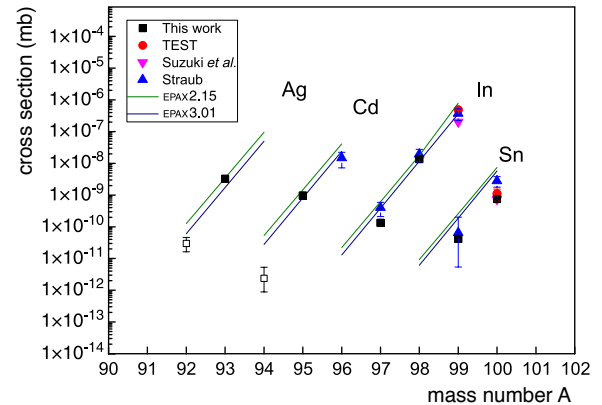


**Figure 2.6:** Comparison of measured and predicted production cross sections of nuclei from the  $N=Z$  line and beyond with statistical uncertainties as determined by Celikovic et al. [Cel+16].

## 2.4 The Detector Setup for Decay Spectroscopy

The decay spectroscopy of the exotic nuclei is performed after they pass the final focal plane F11 with the WAS3ABi/EURICA spectrometer which is designed to study fundamental properties of nuclei and its isomeric states. The implantation detectors of WAS3ABi allow for the study of the half-lives of the  $\beta$ -decay and combined with the  $\beta$ -absorbers the  $Q_{\beta}$ -values are measured. Further decay channels such as direct and

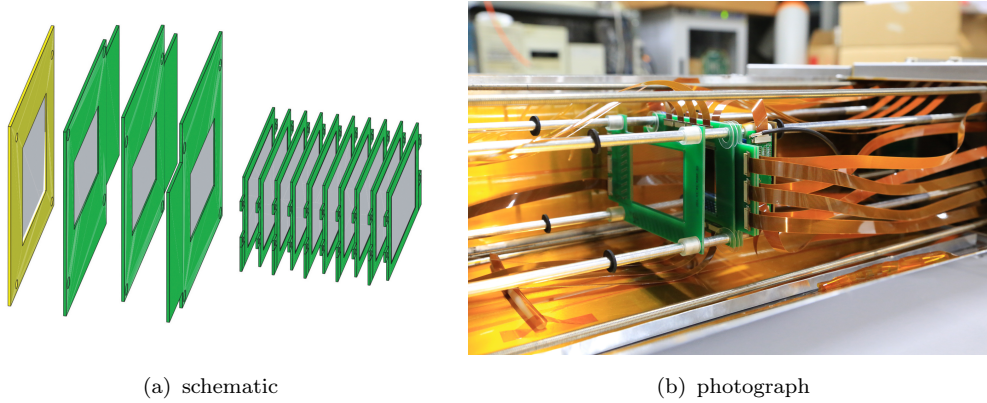


**Figure 2.7:** Schematic and photograph of the WAS3ABi-detectors. Three highly segmented implantation detectors are followed by a positron calorimeter of ten stacked detectors. The yellow detector marks a position detector which was placed in front of the setup to monitor the beam position. The detectors are separated by plastic washers. The photograph shows the Si-detectors and its readout cables mounted on an Aluminum structure.

$\beta$ -delayed proton emission are important observables due to their effect in the network calculations of the astrophysical rp-process. These decay channels can also be detected by the WAS3ABi detector. The study of isomeric decay schemes and the derivation of level schemes requires the detection of  $\gamma$ -radiation which is performed with the EURICA  $\gamma$ -ray-spectrometer surrounding the WAS3ABi ( $\rightarrow$  Sec. 2.4.3). The determination of the physical observables requires a proper calibration of the detector signals which is presented in combination with the introduction of the detector setup and its readout.

### 2.4.1 The Silicon Detector Array WAS3ABi

The Wide-range Active Silicon-Strip Stopper Array for Beta and ion detection (WAS3ABi) is a modification of the SIMBA detector which was designed at TUM<sup>6</sup> [Ste09]. SIMBA was used during the RISING campaign at GSI [Bec+05; Pie+07]. The WAS3ABi consists of three highly segmented double-sided silicon strip detectors for implantation followed by ten stacked single-sided silicon strip detectors which serve as a calorimeter in coherence with the implantation layers. In front of these detectors, a position detector was located to monitor the beam position and profile.

Both setups are designed to perform  $\beta$ -delayed  $\gamma$ -spectroscopy while the difference in their configuration results from the beam energies which were utilized. Compared to the present work, the primary beam energy in the experiment was three times higher ( $E_{\text{GSI}} = 1$  AGeV [Str10]). Thus, the penetration depth for the fragments in silicon was larger and an additional stack of silicon detectors in front of the implantation zone could be used in the GSI experiment [Hin+12].

The method of  $\beta$ -delayed  $\gamma$ -spectroscopy is motivated in the unambiguous study of decay channels by the identification of  $\gamma$ -emission from the daughter nucleus. At the same time, it allows to study the half-lives of isomeric states of implanted nuclei as the delayed  $\gamma$ -emission is also recorded during the implantation.

The decay products remain unstable and continuously trigger the data acquisition by subsequent decay events. The high-granularity afforded by X- and Y-strips allows to require correlated decay events to occur within a spatial window to discriminate back-

<sup>6</sup>Technische Universität München

ground events. A decollimator at the final focus was used to illuminate the entire detector area, so that implantation events are well-distributed and the suppression of the correlation background is maximized.

While the time measurements of decay events is performed from the difference between the timestamps of an implantation event and the corresponding decay event, the energy deposit from single events are obtained by summing up the energy deposit of single strips. The silicon detectors with mass density  $\rho_{\text{Si}} = 2.306 \text{ g/cm}^3$  and a mean energy loss of  $\sim 330 \text{ keV}$  in one detector strip cannot absorb all  $\beta^+$ -particles within the implantation layers because positron energies can reach more than  $10 \text{ MeV}$  depending on the  $Q_\beta$ -value of the decay. Therefore, ten  $\beta$ -absorbers expand the implantation volume with the focus on the determination of the  $Q_\beta$ -value of  $^{100}\text{Sn}$ .

### The Implantation Detectors

The WAS3ABi consists of four different detector units: Double-sided Silicon Strip Detectors (DSSD), with a thickness of  $1 \text{ mm}$  and a segmentation into  $60$  strips vertically (X-direction) by  $40$  strips horizontally (Y-direction) with a width of  $1 \text{ mm}$  each, form the implantation zone in the WAS3ABi detectors ( $\rightarrow$  Fig. 3.6). In front of this implantation zone, the XY-detector was installed. The effective granularity of the implantation detectors was reduced from  $3 \times 2400$  pixels to  $7160$  pixels since one pair of strips was connected to one readout channel. Advantage from this high granularity was taken as the beam was broadened at the last focal plane in order to distribute nuclei across the complete detector area resulting in a nice suppression of the correlation background. Around  $80\%$  of decay events from a certain nucleus are contained within a correlation window of  $3 \times 3$ -pixels and  $57\%$  are contained within one pixel resulting in a maximum background suppression.

Both, the energy and timing signals of each channel of the DSSDs are individually read-out. The energy signals of strips in X-direction were amplified by pre-amplifiers designed at the RIKEN Nishina Center while the signals of the strips in Y-direction were amplified by commercial Mesytec pre-amplifiers<sup>7</sup>. This has allowed for a consistency check of the energy deposit which was measured by different readout systems and a redundant determination of the implantation depth. The mean energy resolution of both sides, X and Y, is determined to  $39 \pm 8 \text{ keV}$  (FWHM) and  $38 \pm 7 \text{ keV}$  (FWHM), respectively. Implantations have clear signals with an energy deposit of several GeV per strip and the implantation affects a large number of strips ( $\sim 10$ - $15$ ) unlike decay events. The data acquisition is started when a signal has crossed the trigger threshold  $E_{\text{thr}}$ . As the charge-signal is proportional to the energy deposit, the slope of the leading-edge of the energy signal correlates with the energy amplitude such that a smaller charge-signal reaches the discriminator thresholds at a later time. Since the highest energy deposit occurs in the strip where a nucleus has passed or was implanted, the position of the implantation is determined by the fastest timing signal in the DSSDs. The detector layer in which the nucleus was eventually stopped is discriminated by the characteristic energy deposit of implantations layer-by-layer. Additionally, if such an energy deposit was observed in the first layer of the  $\beta$ -calorimeter, this event was rejected because this indicates a destruction of the nucleus during the implantation where the residues have passed through further detector layers. More than  $94\%$  of the  $N = Z$  nuclei were stopped

<sup>7</sup>16-channel logarithmic pre-amplifier, model MPR-16

Nucleus	DSSD A	DSSD B	DSSD C	SSSD 1
<sup>100</sup> Sn	63	1950	12	21
<sup>98</sup> In	76	11008	82	149
<sup>96</sup> Cd	127	17275	167	269
<sup>94</sup> Ag	104	15641	255	274
<sup>92</sup> Pd	122	11671	284	224
<sup>90</sup> Rh	47	4566	124	99

**Table 2.2:** Number of implantations in the specific implantation detectors DSSD A, B, C for  $N = Z$  nuclei. The implantations are concentrated into DSSD B. The first SSSD layer served as a veto for implantations which have been destroyed during the stopping process.

in the expected detector layer ( $\rightarrow$  Tab. 2.2) and thus, the analysis of the  $Q_\beta$ -values was constrained to this detector ( $\rightarrow$  Sec. 3.4). The implantation position and depth were monitored online and regarding the proper definition of the implantation depth, a variable Al-degrader was utilized just in front of the WAS3ABi.

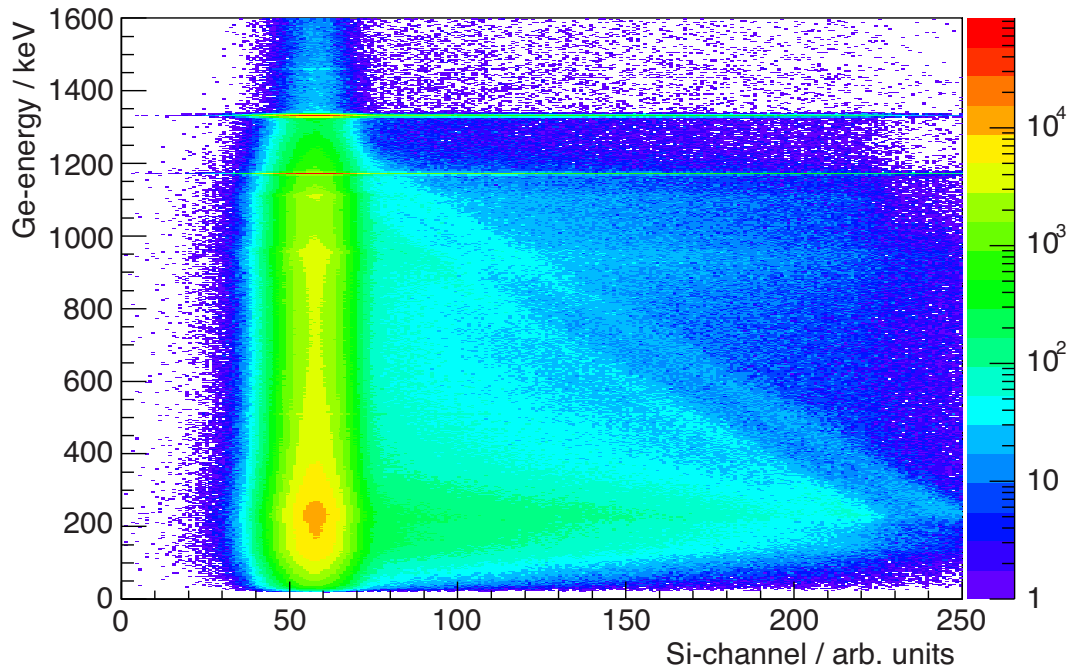
### The $\beta$ -Calorimeter and Event Tracking

The second part of the WAS3ABi detectors is the  $\beta$ -calorimeter which consists of ten SSSD-detectors with a thickness of 1 mm each. The detector front sides are divided into 7 strips, vertically (X-direction) while the detector backsides are not segmented. They are mounted directly behind the implantation area expanding the detector geometry in order to stop positrons up to energies of  $E < 5$  MeV ( $\rightarrow$  Fig. 3.5). This is larger than the  $Q_\beta$ -value of <sup>100</sup>Sn but it does not prevent the  $\beta^+$ -particles from detector escape because of gaps between the detectors and only one side of the the implantation zone is equipped with such a calorimeter.

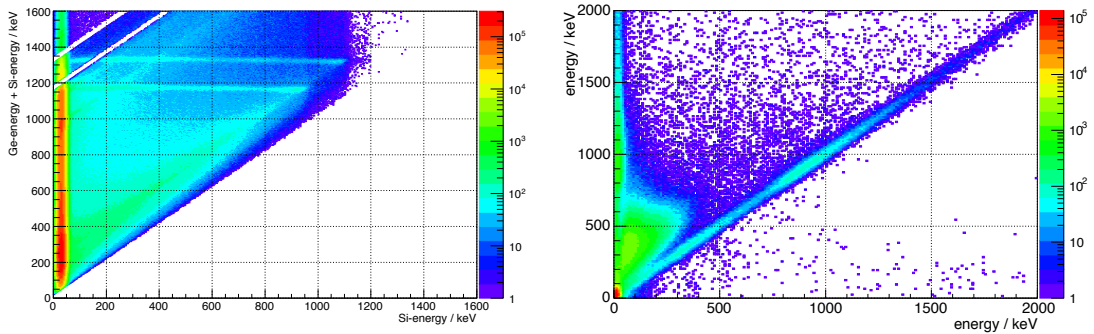
Compared to implantation events the energy scale of decay events is orders of magnitude smaller such that the determination of the summed energy of such an event is facile since no saturation occurs in the linear range of the pre-amplifiers. However, the signal of particles with small energies is in the range of the noise level. For that reason, it is experimentally delicate to set the trigger threshold that “real” events with the smallest energies are also measured while minimizing the noise. Therefore, the threshold energies  $E_{\text{thr}}$  were conservatively chosen as  $E_{\text{thr}} > 100\text{keV}$ . This is clearly above the noise level ( $\approx 50$  keV) and prefers incomplete summation over adding noise because it is advantageous to compare a simulation with the same thresholds rather than considering the noise in the simulation ( $\rightarrow$  Sec. 3.4.2). Other effects which contribute to the energy sum of decay particles are bremsstrahlung by Compton-scattering and annihilation radiation when positrons recombine with electrons before being stopped. This radiation could have been distinguished if the positrons made coherent tracks in terms of a pattern analysis. However, the study using the **Geant4**-simulation unambiguously shows that multi-scattering between different detector layers occurs such that  $\gamma$ -radiation cannot be generally distinguished from the energy deposit by positrons ( $\rightarrow$  Sec. 3.4.2).

## 2.4.2 Energy Calibration of the Si-Detectors in WAS3ABi

The energy calibration of the Si-detectors was performed by exploiting the Compton-scattering of  $\gamma$ -rays from a <sup>60</sup>Co-source and the well-calibrated energies of the HPGe-detectors. The HPGe-detectors were already setup and calibrated using a standard <sup>152</sup>Eu-source. For the WAS3ABi calibration, the <sup>60</sup>Co-source was placed as close as



(a) correlation of HPGe and DSSD



(b) reconstructed energies

(c) X-Y-correlation

**Figure 2.8:** Calibration of Si-detectors using the Compton-scattering-method. The Compton-edge and correlations between Si-detectors and HPGe-detectors are clearly visible (top) where the calibration parameters are derived by a linear fit of the diagonal lines. The reconstructed energy sum of deposit in Ge- and Si-detectors shows the correlation of the sum with the transition energies of  $^{60}\text{Ni}$  as well as the correlation of energies from the readout of X-sides and Y-sides of Si-detectors, which is a bisecting line, indicating that the calibration of Si-detectors is fine.

possible to the Si-detectors to maximize the amount of scattered  $\gamma$ -rays. The  $^{60}\text{Co}$ -source emits two  $\gamma$ -rays with energies of  $E_{\gamma}^{4+} = 1173 \text{ keV}$  and  $E_{\gamma}^{2+} = 1332 \text{ keV}$  which originate from the de-excitation cascade of  $^{60}\text{Ni}$  after the  $\beta$ -decay of  $^{60}\text{Co}$  ( $\rightarrow$  Fig. 2.9). The energy of Compton-scattered  $\gamma$ -rays in WAS3ABi is partially deposited in a Si-detector strip and in a HPGe-detector of EURICA. Therefore, each scattered  $\gamma$ -emission from the source should enable a clear energy correlation in both detector directions. This correlation is clearly visible in Figure 2.8(a) where the energy deposit in HPGe-detectors and one SSSD channel in X-direction is plotted. The two horizontal lines represent the absorption of non-scattered radiation in the HPGe-detectors. The correlation of radiation which was scattered in the Si-detectors before absorption in the Ge-detectors is given by the diagonal lines where the end of the lines at higher Si-detector energies defines the Compton-edge  $E_C = h\nu - E_{e^-} = \frac{h\nu}{1+2h\nu/m_0c^2}$  ( $\rightarrow$  Fig. 2.8(a)). The energies of the Si-detectors are then derived by a linear fit to the diagonal lines. The energy resolution of these detectors is directly represented by the width of the Gaussian profile of the diagonal lines resulting in  $\sim 40 \text{ keV}$  (FWHM) for 1173 keV and 1332 keV. After the energy calibration has been completed for all strips in both directions, X and Y, the consistency of the analysis was checked by the reconstructed sum of energies from Ge- and Si-detectors as well as the correlations of  $E_x$  and  $E_y$  shown in Figure 2.8(c). The two horizontal lines at the energies which agree with the emission from the  $^{60}\text{Co}$ -source in the reconstructed energy sum ( $\rightarrow$  Fig. 2.8(b)) indicates that a linear calibration works well. The reconstructed energy sum was obtained by adding up the energy of the HPGe-detectors and a strip of the Si-detectors. The differences to both sides of the diagonal in the X-Y-correlation arises due to a zero suppression which was only applied to the readout of the strips in X-direction.

In the analysis, the strict correlation of energy measurements on both sides of the Si-detectors is used to clean up the event selection concerning the correlation of implantation and decay events.

### 2.4.3 The EURICA Spectrometer

The Euroball-RIKEN Cluster Array (EURICA) is a high resolution  $4\pi$ - $\gamma$ -ray-spectrometer. The drawing of the detector setup is shown in Figure 2.10. The mechanical structure consists of three rings arranged by inclination angles of 51 deg, 90 deg and 129 deg with respect to the beam-line. Each ring can carry up to five clusters of seven High Purity Germanium (HPGe) detectors or six  $\text{LaBr}_3(\text{Ce})$  detectors each. The detectors were placed as close as possible to the WAS3ABi box. In the present experiment, 47 HPGe-detectors and 18  $\text{LaBr}_3(\text{Ce})$ -detectors were used. While the former detectors have an energy resolution of  $\Delta E = 2.89 \text{ keV}$  at 1333 keV, the latter ones have a much better timing resolution (150 ps - 400 ps [Glo+05]). In the framework of this thesis,  $\beta$ -delayed  $\gamma$ -spectroscopy was performed. Hence, the  $\text{LaBr}_3(\text{Ce})$ -detectors were not considered in the analysis as they contribute more to the systematic uncertainties than is gained by the improvement of statistical uncertainties due to their low energy resolution corre-

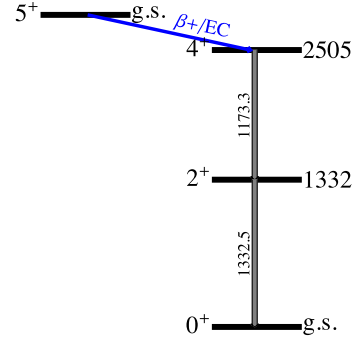


**Figure 2.9:** Level scheme of  $^{60}\text{Co}$ . Energies in keV.

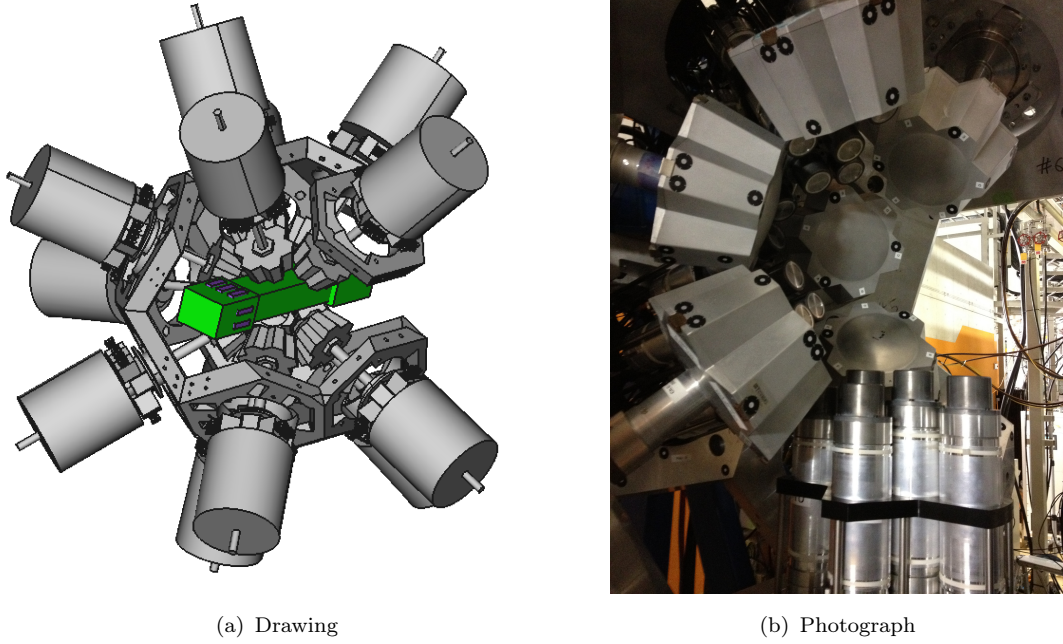


**Figure 2.10:** The EURICA spectrometer is arranged in a  $4\pi$  geometry and consists of 84 HPGe-detectors in 12 clusters of 7 detectors each and 18 LaBr(Ce) detectors in 3 clusters of 6 detectors each. The green box in the middle marks the position of the WAS3ABi Si(Li)-detectors. The photograph shows one half of the EURICA spectrometer: 6 clusters of HPGe-detectors (polygonal shapes) and 3 clusters of LaBr(Ce)-detectors (circular shapes).

sponding to a much worse signal-to-noise background ratio.

The signals of each of the HPGe-detectors are split into two channels which are read out using two separate branches, a digital branch for energy measurements and an analog branch for timing measurements. The signals from the energy branch are processed by the digital gamma finder (DGF) modules [LLC]. The clock frequency of the DGF modules was 40 Mhz (25 ns step size) with a recording time of 100  $\mu$ s when the DAQ is triggered. EURICA is equipped with its own data acquisition but is triggered by the Si-detectors because one is interested in the  $\gamma$ -radiation which is correlated with implantations or decays. The timing measurement using the second pre-amplifier output is used to derive the time of the  $\gamma$ -detection subsequent to the implantation or the decay event. This output was sent to an analog timing branch which was composed of a timing filter amplifier (TFA), a constant fraction discriminator (CFD) and a time-to-digital-converter (TDC) circuit. In the last step, the signal of the CFD was split. One branch was sent to a short-range TDC module with a range of 1.2  $\mu$ s and 0.31 ns digital time resolution [Sö+13]. The other branch was sent to a long-range TDC module with a range of 800  $\mu$ s with 0.73 ns digital time resolution. Due to the energy-dependent absorption cross section  $\sigma_a$  of Compton-scattering, which is described by the Klein-Nishina formula, the energy of

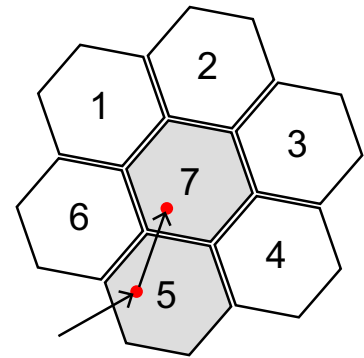


**Figure 2.11:** Schematic of the addback method which is applied to neighboring crystals of the HPGe-detectors. The red dots represent the interaction center of a scattered  $\gamma$ -ray. If they are coincident by 400 ns, both are summed up to a single energy.

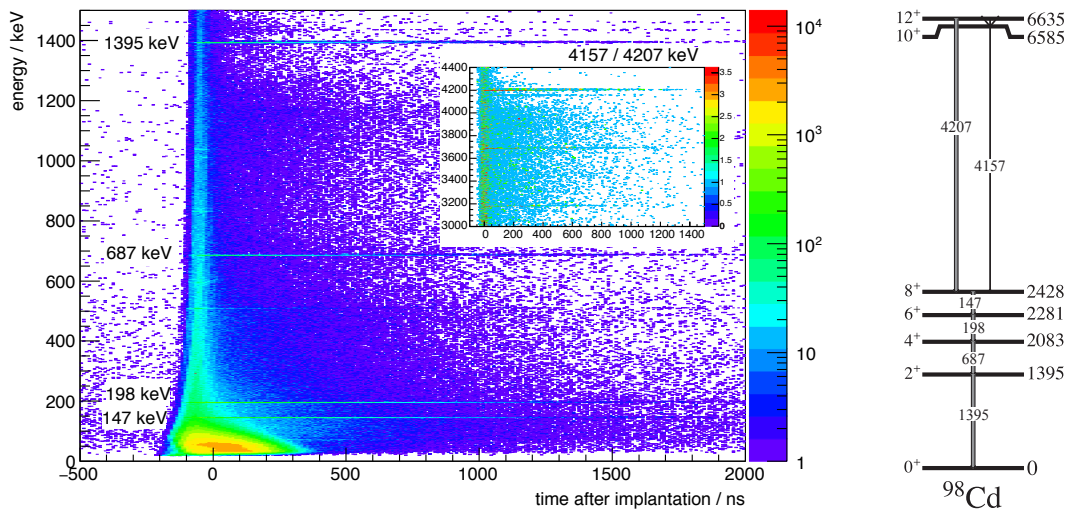


**Figure 2.12:** Energy-vs-time plot of delayed  $\gamma$ -radiation from  $^{98}\text{Cd}$  nuclei and the level scheme as reported by Blazhev et al. [Bla+10]. The red horizontal square marks for which event selection coincidences are considered while the the time window for coincidences is defined by  $\pm 200$  ns with respect to the corresponding time of the gated event.

the  $\gamma$ -emission is more likely to be deposited in two neighboring crystals for higher energies. The so-called “addback” method was applied in order to find energy deposited in crystals which originates from a single incident  $\gamma$ -ray. Thus, energy depositions in neighboring crystals which are coincident by a time window of 400 ns are summed up or remained unchanged otherwise. This method increases the detection efficiency at higher energies ( $\rightarrow$  Sec. 2.4.4).

### 2.4.4 The Detection Efficiency

Although the EURICA spectrometer covers a large solid angle, the geometry is not closed. Compton-scattering, escape of  $\gamma$ -emission and the recovery time of the detectors incorporates incomplete energy measurement. The energy-dependent fraction of unobserved  $\gamma$ -radiation is accounted for by an efficiency factor  $\epsilon_{\gamma}(E_{\gamma})$ . This factor is determined by an absolute energy calibration from coincident  $\gamma$ -emission in  $^{98}\text{Cd}$  which originates from the cascading de-excitation of the  $8^+$  and  $12^+$  isomeric states by E2-transitions. The level scheme of  $^{98}\text{Cd}$  is shown in Figure 2.12 with the core-excited, isomeric  $10^+$  and  $12^+$ -states with excitation energies above the shell gap. The energy-vs-time plot of the  $\gamma$ -emission clearly shows the delay of the transitions with regard to the time of implantation. Thus, the coincidence of two transitions is defined by a time window of 400 ns which is the uncertainty introduced by the time walk at low energies. This aberration is a classical delay problem. The rise time of signals is constant but the slope differs according to the energy amplitude such that the trigger threshold is reached earlier for high energy signals ( $> 300$  keV) than for low energy signals. The magnitude of the shift was determined by the time difference between the baseline and the maximum intensity for a certain energy. The non-linear shift was corrected by a polynomial model of second order in  $\frac{1}{E}$ .

Due to high transfers of angular momenta and energies during the production, many excited states are populated in fragmentation but only the long-lived isomeric states are

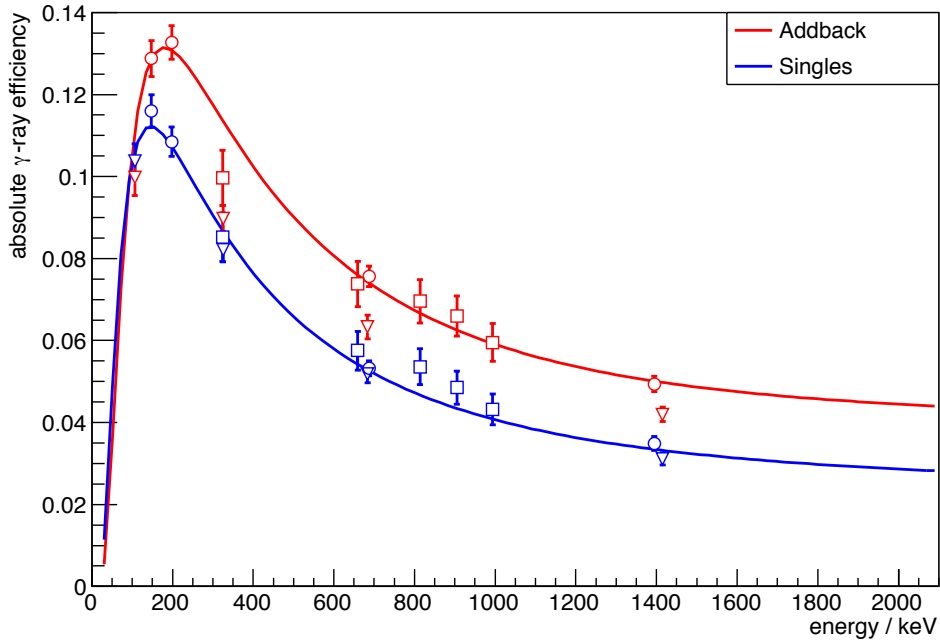


**Figure 2.13:** Efficiency calibration curve of the HPGe-detectors for energy deposited in single detectors (blue) and the addback method applied (red). The circles, squares and triangles label the efficiencies which are derived from cascading transitions in  $^{98}\text{Cd}$ ,  $^{94}\text{Pd}$  and  $^{96}\text{Pd}$ , respectively.

observed in the EURICA spectrometer as the states with short half-lives ( $< 50$  ns) are already depopulated during the flight through the BigRIPS.

In the efficiency calibration, the transitions with energies 147 keV, 198 keV, 687 keV and 1395 keV, which start from the  $8^+$  isomer, were used to study its coincidences. If one of these energies are measured, the other transitions must have also occurred because they belong to the same cascade. Hence, the energy dependent  $\gamma$ -detection efficiency is given by the ratio of the number of coincidences of a cascading transition  $N_C(E_{\text{coin}})$  when  $N_G(E_{\text{gate}})$  transitions at the gate energy  $E_{\text{gate}}$  were observed.

$$\epsilon_\gamma = \frac{N_C(E_{\text{coin}})}{N_G(E_{\text{gate}})} \quad (2.8)$$

Both numbers have to be corrected for random coincidences which is performed by considering the adjacent areas in energy aside from the corresponding line. To increase the number of points for the fit of the efficiency curve this method has also been applied to  $^{94,96}\text{Pd}$  which have similar cascades of de-excitation. The results are shown in Figure 2.13 and the efficiency curve results from a fit of an empirical model with parameters  $\alpha_i$  [Rei13]

$$\epsilon_\gamma(E) = \left( \alpha_1 E + \frac{\alpha_2}{E} \right) \cdot \exp\left( \alpha_3 E + \frac{\alpha_4}{E} \right) \quad (2.9)$$

The determination of the  $\gamma$ -efficiency is important as the determination of the branching ratios depends on the calibration and in particular, the scenario for the level scheme of  $^{100}\text{In}$  has to be concluded from the study of  $\gamma$ -energies ( $\rightarrow$  Sec. 4.2).

## 2.5 The Detector Readout

The readout of the silicon detectors had to handle both, very small signals which occur in decay events and large signals of several 10 GeV which are deposited in the implantation of nuclei. Each detector strip was read out separately so that overall 299 channels were read out for the implantation detectors and 80 channels are read out for the  $\beta$ -absorbers. At first, in-house designed, charge-sensitive linear preamplifiers (CS AMP-3) were used to amplify the charge signal from each of the 60 silicon strips in X-direction while the commercial Mesytec linear-logarithmic pre-amplifiers (MPR-32) were used to amplify the charge signals from the Y-strips. Thus, both, the small and large signals could be used, by employing two independent readout systems. However, in this experiment the implantation position in X-Y direction was derived from the timing signals of the strips. Therefore, the information about the energy deposition of implantations is of minor interest.

The amplified signals of X- and Y-sides were sent to pulse shaping filter amplifiers (Caen N568B, Mesytec STM-16+). Here, the signals were split into a timing and an energy signal. The latter was sent to a peak-sensing ADC unit (Caen 785V) which converted the analog signal into a 16-bit digital signal. The former output channel was sent to leading edge discriminators (LeCroy 4413) to generate a logic signal in order to perform the time measurement by using long-range multi-hit TDCs (Caen VX1290A-2eSST) with a time gate of 10  $\mu$ s. Once the readout is triggered the detector system is not available for further event detection for the period of the signal decay time referred to as detector recovery. In particular, in case of saturation, which occurs during the implantation, the recovery becomes easily large. Eventually, an average dead time of  $\approx 400 \mu$ s was achieved resulting in a total dead time of 4.3% of the beam-on-target time. A schematic of the readout system of the WAS3ABi detectors and the triggering system is shown in Figure 2.14.

In contrast to the implantation detectors, the position detectors were read out by using a resistive chain which has four channels (two for each direction). The signals are amplified and sent to the ADCs, equal to the signal processing of the X-directions, allowing for the determination of the position from the ratio of the energy signals. Behind the  $\beta$ -absorbers, a veto detector was placed serving as hardware discrimination of the light particle background. If a sufficient amount of energy was deposited in this detector the DAQ trigger was prevented as only light particles (e.g. deuterons) and positrons with energies above 5 MeV are able to pass 13 mm of silicon.

The readout of the EURICA spectrometer has already been introduced in Section 2.4.3 which is identical to the one which had been used during the RISING campaign which was discussed in detail by Pietri et al. [Pie+07]. The data acquisitions of BigRIPS, WAS3ABi and EURICA were used independently in order to optimize the recovery time of the data acquisition system. Thus, the different DAQs were synchronized by using a Logical Unit for Programmable Operation (LUPO) which assigns a unique timestamp to each event in each DAQ. When the time of flight and all delay times are properly known, data from the particle identification, implantations and decays are related by the correlation of their timestamps.

The electronic readout of the present experimental setup has several triggers which start the DAQs when a certain threshold is reached. Regarding the energy calibration of the Si-detectors, the energy deposit in both, WAS3ABi or EURICA, triggered the DAQ<sup>W</sup>

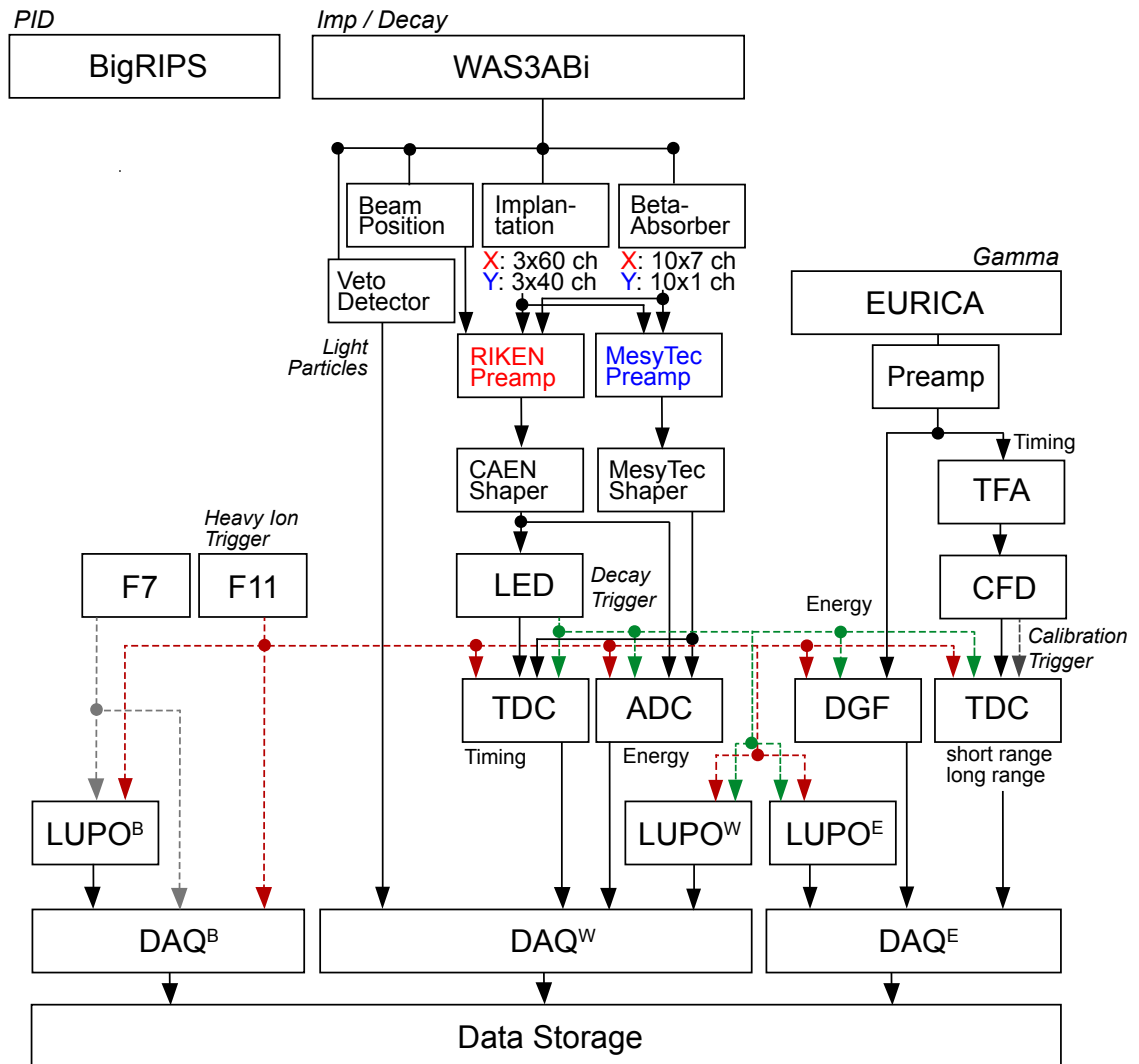


**Figure 2.14:** The WAS3ABi/EURICA readout and the implementation how to discriminate between implantation and decay events with the heavy ion trigger at the focal plane F11. The DAQ was only triggered if the veto detector, which identifies light particles, has not been triggered. The implantation detectors trigger the independent EURICA DAQ as well. The dashed lines represent a different trigger logic during the calibration and during the experiment - Short cuts, ADC: analog-to-digital converter, CFD: constant fraction discriminator, DAQ: data acquisition, DGF: digital gamma finder, LED: leading-edge discriminator, LUPO: logic unit for programmable operation, TFA: timing filter amplifier, TDC: time-to-digital converter

---

and DAQ<sup>E</sup>. The gray dashed line in the EURICA column of the readout schematic indicates the trigger for the calibration of the HPGe-detector which starts only DAQ<sup>E</sup>. Another trigger which is not used during the beam-on-target time, starts DAQ<sup>B</sup> at the focal plane F7 which is used for the purpose of beam calibration. In contrast, during the experiment the readout was only started by the heavy ion trigger at F11 and by the implantation detectors of the WAS3ABi. While the trigger at F11 starts DAQ<sup>B,W,E</sup>, the trigger by the implantation detectors starts only DAQ<sup>W,E</sup> such that events are classified as implantations and decays, respectively. The decay events are further distinguished according to their patterns in the energy deposition ( $\rightarrow$  Sec. 3.2).

# 3 Analysis

In this chapter, the methods of the determination of the half-lives and the  $Q_\beta$ -values are introduced. All analysis steps are based on a proper spatial correlation of implanted ions and their corresponding decays. In particular, in case of long half-lives or low energy deposit in the detectors, the background contribution and systematic uncertainties of the model assumptions have to be properly taken into account. For instance, the energy loss and the distribution throughout the detector is characteristic for every particle type. However, radiation of different type cannot be disentangled if it was observed within the same event in a single detector. The recovery time of the data acquisition, detector thresholds and electron capture led to decays remaining unobserved and consequently corrections for these losses have to be introduced. Since any specific analysis method is associated with systematic uncertainties, different methods are used in order to test the models.  $^{98}\text{Cd}$ , which is a nucleus in the region of  $^{100}\text{Sn}$  whose half-life and  $Q$ -value is precisely known, has been used to test and compare different analysis techniques with respect to their reliability and systematic uncertainties.

## 3.1 Half-Life Analysis

According to the law of radioactive decay, the half-lives of a nucleus are derived straight forward from the measured activity. However, it becomes difficult to infer conclusions of the half-life experimentally as several decay processes from the same decay chain contribute to the experimental spectrum. In  $\beta$ -spectroscopy, radioactivity from daughter decays and background decays from products of previously implanted nuclei also contribute to the total spectrum. Hence, it is essential to use a probability distribution which incorporates all significant processes of the decay chain as well as the background rate.

This issue has been addressed in previous works by considering decay scenarios which are possible with regard to the observation of a number of events with  $\leq 3$  decay correlations within a fixed time window [Sch95b; Sto02; Hin+12]. In the construction of the probability density, every combination of event sequences within a decay chain was considered. It starts with the parent nucleus and considers whether the decay has occurred or whether it has not occurred multiplied by the probability that it has been observed. In this work, a similar approach is used by considering only the first decay correlations in order to verify the determination of the half-life of  $^{100}\text{Sn}$ .

Apart from this method, the binned maximum likelihood method (MLH-method) is usually employed, which has the same characteristics as the unbinned MLH-method. It is easier to handle because the number of factors in the product of the probability density is tremendously reduced. This method is applicable due to a sufficiently large number of implantations in most of the cases which allows for a sufficiently small binning. In this section, the properties of the MLH-method are introduced and explained by the example of the radioactive decay.

### 3.1.1 The Maximum Likelihood Approach (MLH)

Suppose a sample  $(x_i)$  of a stochastically independent random variable  $X$  which is distributed according to the probability density function (p.d.f.)  $f(x, \alpha)$  where  $\alpha$  is a set of unknown parameters. The MLH-method maximizes the density function

$$\mathcal{L}(\alpha) = \prod_i f(x_i, \alpha) \quad (3.1)$$

The function  $f(x_i, \alpha)$  is the probability density with a set of model parameters  $\alpha$ . The most likely set of parameters results in a maximum of  $\mathcal{L}(\alpha)$ . Since sums are usually easier to handle than products, the log-likelihood function is defined as

$$\ell(\alpha) = \ln [\mathcal{L}(\alpha)] = \sum_i \ln[f(x_i, \alpha)] \quad (3.2)$$

and the maximum condition is defined by its first and second derivative

$$\left. \frac{\partial \ell(\alpha)}{\partial \alpha} \right|_{\alpha_{\max}} = 0 \quad \wedge \quad \left. \frac{\partial^2 \ell(\alpha)}{\partial \alpha^2} \right|_{\alpha_{\max}} < 0 \quad (3.3)$$

The likelihood expressions above represent a probability to find a set  $(x_i)$  by  $N$  measurements where the  $(x_i)$  are the observed (unbinned) values. If the number of events is large, they are represented in a histogram of  $M$  bins with constant bin size  $\omega = \frac{x_{\omega} - x_0}{M}$  and the variation of the p.d.f is small within the bin size, the unbinned MLH-analysis can be used equivalently to a binned MLH-analysis [Cou00]. The equality of both methods is derived according to Adye [Ady98]. The (measured) bin contents  $n_b$  and the integral of the model function  $f_b$  are given by

$$n_b = \int_{x_0 + \omega(b-1)}^{x_0 + \omega b} \sum_{i=1}^N \delta(x - x_i) dx \quad f_b = \int_{x_0 + \omega(b-1)}^{x_0 + \omega b} f(x_i, \alpha) dx \quad (3.4)$$

where  $f(x_i, \alpha)$  does not need to be normalized in a sense of a probability density that  $\int f(\alpha) d\alpha = 1$  because it is interpreted as a parameterization of the histogram shape [Cou00]. The main assumption in the binned MLH-method is that a bin contents' underlying distribution is Poissonian. Then, the histogram likelihood is written as

$$\mathcal{L}_b(\alpha) = \prod_{b=1}^M \frac{f_b^{n_b} e^{-f_b}}{n_b!} \quad \rightarrow \quad \ell_b(\alpha) = - \sum_{b=1}^M (n_b \ln f_b - f_b - \ln n_b!) \quad (3.5)$$

After substituting definitions of  $n_b$  and  $f_b$  into equation (3.5) the expressions of the binned and unbinned MLH-method are compared.

$$\ell_b(\alpha) = \sum_{i=1}^N \left[ \int_{x_0 + \omega(b-1)}^{x_0 + \omega b} \delta(x - x_i) dx \right] \left[ \ln \left( \int_{x_0 + \omega(b-1)}^{x_0 + \omega b} f(x_i, \alpha) \right) \right] \quad (3.6)$$

$$= \sum_{i=1}^N \int_{x_0}^{x_{\omega}} \delta(x - x_i) \ln(\omega f(x_i, \alpha)) dx \quad (3.7)$$

$$= \sum_{i=1}^N \ln f(x_i, \alpha) - N \ln \omega \quad (3.8)$$

Obviously, the first term in equations (3.8) and (3.2) is equal and the constant term  $N \ln \omega$  has no effect on the maximum position of the log-likelihood  $\ell_b(\alpha)$ . Thus, the binned and unbinned MLH-approach yield the same results if the bin contents are Poissonian.

Besides the most likely parameter set  $\alpha^*$  of a set  $(x_i)$ , the reliability of the fit result  $\alpha^*$  is given by its confidence intervals which are obtained by considering the momenta of a distribution.

Momenta are defined as the expectation values of a power in the random variable as  $\langle X \rangle = \int m(x)p(x)dx$  with  $m(x) = x^k, k \in \mathbb{N}$ . The momenta of first and second order are the most important ones as they yield the mean value  $\mu(X, \alpha)$  and the variance  $V(X, \alpha) = \sigma^2(X, \alpha)$  [Bul79].

Regarding the variance, these integrals can be complicated. But according to the *central limit theorem*, the standard deviation converges to a Gaussian distribution as the sample size becomes large ( $N \geq 30$ ). Then, the standard deviation is given in terms of the log-likelihood function by

$$\sigma^2(\alpha^*) = \left( \frac{\partial^2 \ell(x_1, \dots, x_n | \alpha)}{\partial \alpha^2} \Big|_{\alpha=\alpha^*} \right)^{-1} \quad (3.9)$$

This holds no longer when the sample size becomes smaller ( $N < 30$ ) so that explicit integrals as shown in Equations (3.10, 3.11) have to be calculated.  $\epsilon$  denotes the level of significance and it defines the probability of finding the true value within the confidence interval [Sch+84]. Then, the lower and upper limits  $\alpha_{l,u}$  of the best-estimator  $\alpha^*$  are defined as

$$\int_{\bar{x}=1/\hat{\alpha}}^{\infty} \mathcal{L}^*(\alpha_l, \bar{t}) dt = \frac{\epsilon}{2} \quad (3.10)$$

$$\int_{\bar{x}=0}^{1/\hat{\alpha}} \mathcal{L}^*(\alpha_u, \bar{t}) dt = \frac{\epsilon}{2} \quad (3.11)$$

### 3.1.2 Example: The p.d.f. of the Radioactive Decay

The MLH-method is applied to the radioactive decay where  $(x_i) = (t_i)$  denotes the set of event decay times correlated with an implantation, and  $\alpha$  corresponds to the decay constant  $\lambda = \frac{1}{\tau}$  with the lifetime  $\tau$ . Suppose,  $f(x_i, \alpha) = p(t_i, \lambda) = \lambda \cdot \exp(-\lambda t_i), \lambda > 0$ . Radioactive decay is a stochastically independent process. Thus, the likelihood function is

$$\mathcal{L}(\lambda) = \prod_i p(\lambda, t_i) = \lambda^N \exp\left(-\lambda \sum_i^N \bar{t}_i\right) \quad (3.12)$$

The best-estimator  $\tau^*$  and the standard deviation  $\sigma_\tau$  are given by the first and second derivative as described in the previous paragraph resulting in

$$\tau^* = \frac{1}{N} \sum_i t_i \quad \sigma(\tau^*) = \frac{\tau}{\sqrt{N}} \quad (3.13)$$

This is a surprisingly simple result as the best maximum likelihood estimator is given by the mean of the measured decay event times. This holds for a pure exponential decay and if further components are present, the p.d.f is changed.

For a small number of events, the uncertainties cannot be estimated by a Gaussian but

the integrals (3.10) are used according to Schmidt et al. [Sch+84]. For a sample size  $N > 2$  the lower and upper limits are further approximated according to Eadie et al. [Ead+71] and the result for the  $1\sigma$ -confidence interval  $\lambda_l < \lambda < \lambda_u$  is

$$\lambda_l = \frac{\bar{t}}{1 + 1/\sqrt{N}} \quad \lambda_u = \frac{\bar{t}}{1 - 1/\sqrt{N}} \quad (3.14)$$

If  $N \leq 2$ , this approximation is not applicable anymore and the Gaussian integral  $\int_z^\infty \frac{1}{\sqrt{2\pi}} e^{-x^2/2} dx$  has to be solved explicitly. In case of the exponential distribution the ratios of the limits with the MLH estimator are given by  $\lambda_l^{N=2}/\lambda_m = 0.606$ ,  $\lambda_u^{N=2}/\lambda_m = 2.82$ ,  $\lambda_l^{N=1}/\lambda_m = 0.543$  and  $\lambda_u^{N=1}/\lambda_m = 5.79$ . This case finds its application in the determination of uncertainties of the half-lives of  $N = Z - 2$  nuclei which show only 1 and 2 decay correlations, correspondingly ( $\rightarrow$  Sec. 4.1.1).

### 3.1.3 The Bateman Equations

The likelihood of the radioactive decay just derived is only valid for distinguishable radioactive decays from a parent state to a stable state of the daughter nucleus. However, the decay products are often radioactive, too. This contributes to the shape of the spectrum and has to be considered in the fit model for a proper estimation of the observables which results in a set of coupled differential equations, the Bateman equations:

$$\frac{dN_1(t)}{dt} = -\lambda_1 N_1(t) \quad (3.15)$$

$$\frac{dN_i(t)}{dt} = -\lambda_i N_i(t) + \lambda_{i-1} N_{i-1}(t) \quad (3.16)$$

$$\frac{dN_k(t)}{dt} = \lambda_{k-1} N_{k-1}(t) \quad (3.17)$$

The first line is just the law of radioactive decay while the second line represents the evolution of a population of  $N_i(t)$  nuclei of species  $i$  at time  $t$  decaying by a rate  $\lambda_i$  to its daughter nucleus with a population  $N_{i+1}(t)$ . The last line prescribes the growth of a population by the decay of its parent nuclei.

Bateman [Bat10] has solved these equations and the solution of the evolution of the  $i$ -th species with  $N_{i>1}(0) = 0$  is generally given by

$$N_n(t) = \frac{N_1(0)}{\lambda_n} \sum_{i=1}^n \lambda_i \left( \prod_{j=1, i \neq j}^n \frac{\lambda_j}{\lambda_j - \lambda_i} \right) e^{-\lambda_i t} \quad (3.18)$$

The evolution of the p.d.f of the first three components is shown in Figure 3.1. In the analysis, the sum is cut off where the correlation window<sup>1</sup>  $t_c \ll \lambda_i^{-1}$  so that, in fact, the  $i$ -th daughter component cannot be distinguished from a constant background contribution. Apart from daughter decays, several nuclei have isomeric states with another decay constant as the ground state (e.g. the decay of  $^{98}\text{In}$  and  $^{94}\text{Ag} \rightarrow$  Sec.4.1.2). Then, the solution in equation (3.18) is applied to each isomeric state separately. Eventually, decays are governed by the Bateman equations but dead time losses, and losses in detection efficiency or electron capture make events not observable altering the p.d.f. The

<sup>1</sup>The time range within which decay correlations were assigned to implantations ( $\rightarrow$  Sec. 3.2).

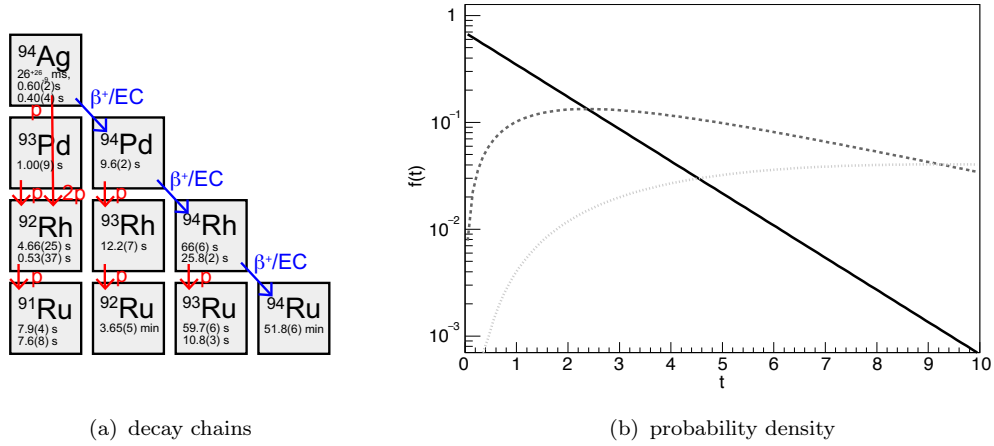


**Figure 3.1:** a) Schematic of radioactive decay chains starting from  $^{94}\text{Ag}$ . b) Probability density of parent (solid), daughter (dashed) and grand daughter (dotted) decay with half-lives of 1.0 s, 3.0 s and 10.0 s, respectively.

losses of electron capture are considered by the nucleus-dependent branching ratios of electron capture  $b_{\text{EC}}^i$  of the  $i$ -th component of the decay chain while the losses which are associated with the detection efficiency are represented by a constant factor  $\epsilon_{\text{det}}$ .

### 3.1.4 Analysis from First Decay Correlations

The method described above is appropriate if all decay correlations subsequent to an implantation are considered in the time spectrum. However, the p.d.f. is changed, if the half-lives are derived by considering only the first decay correlation after an implantation event. This method is particularly useful if daughter decay schemes are not well-known or daughter half-lives are rather short.

Then, the p.d.f. is constructed applying the conventions by Schneider [Sch95b] who has constructed the probability density for the radioactive decay of nuclei when  $N \leq 3$  decay correlations are observed within a time window  $t_c$  and a background rate  $b_r$  which is assumed to be constant. This is applied to one decay correlation which occurs certainly and a time window which is defined by the occurrence of the first correlation where the decay constant of the parent and daughter decay are given by  $\lambda_1$  and  $\lambda_2$ , respectively. Regarding a first decay correlation, there are six contributions in the p.d.f. if the decay chain is considered up to the daughter decay.

$$D_1 O_1 B_0 + D_1 \overline{O}_1 B_1 + \overline{D}_1 B_1 + D_1 \overline{O}_1 D_2 O_2 B_0 + D_1 \overline{O}_1 \overline{D}_2 B_1 + D_1 \overline{O}_1 D_2 \overline{O}_2 B_1 \quad (3.19)$$

where  $B_{1,0}$  are the probabilities whether the first decay correlation is a background event or whether it is not a background event,  $D_i$  denotes the probability for the parent and daughter decays to occur within a time range  $dt$  and  $\overline{D}_i$  denotes the probability that the corresponding decay has not occurred until a certain time  $t$ .  $B_r$  is given by a Poissonian distribution  $(\lambda_b \cdot t_c)^r e^{-\lambda_b \cdot t_c}$  with the background rate  $\lambda_b$ .  $O_i, \overline{O}_i$  are the probabilities whether a certain decay is observed if it has occurred or whether it is not. This is composed of the fraction of electron capture  $\epsilon_{\text{EC}}$  and the detection efficiency of a correlation decay within a certain detection area  $\epsilon_A$  around the implantation position which was set to 1 pixel in the case of  $^{100}\text{Sn}$  because it yields the best signal-to-noise

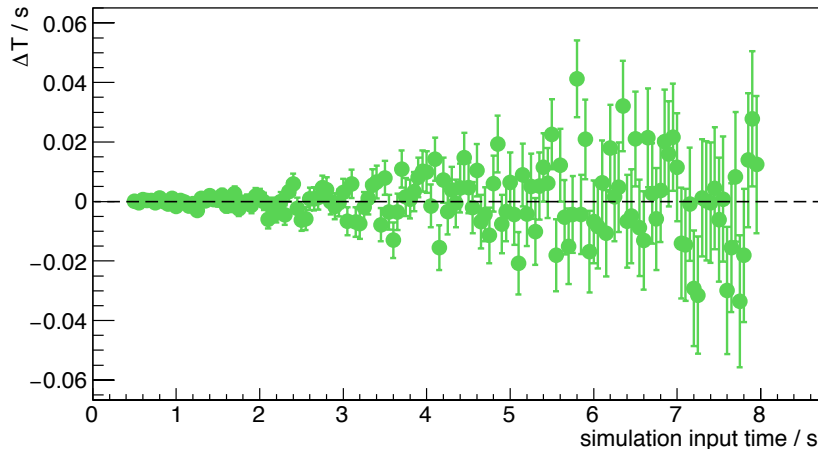


**Figure 3.2:** Differences  $\Delta T$  between the input of Monte Carlo simulations of decay curves and the corresponding fit results for the half-life of the parent nucleus in a decay chain with two components, parent decay and daughter decay. Both components have an electron capture branching of  $b_{\text{EC}}^{\text{par}} = 0.115$  and  $b_{\text{EC}}^{\text{dau}} = 0.151$ , respectively and the half-life of the daughter  $T_{1/2}^{\text{dau}} = 10$  s is fixed.

ratio. The probabilities  $D_i$  and  $\overline{D}_i$  are given by the Bateman-Equations ( $\rightarrow$  Eqn. (3.18)) and are explicitly shown in Appendix C.

This method was applied to  $^{100}\text{Sn}$  in order to perform a consistency check with the binned MLH-method ( $\rightarrow$  Sec. 4.1.3) when the half-lives are extracted by considering all decay correlations within a fixed time window.

### 3.1.5 Test of the Half-Life Analysis

The reliability of the determination of the half-lives is checked by means of the MLH-method with a Monte-Carlo simulation and the half-life fit is applied to a time spectrum which contains all decay correlations as well as a  $\gamma$ -gated time spectrum in the case of  $^{98}\text{Cd}$ .

In the simulation, a time spectrum is generated by considering a parent decay and the subsequent daughter decay with different electron capture branches. The generated distribution is used to determine the half-life by the MLH-method. Afterwards, the resulting fit values are compared with the simulation input ( $\rightarrow$  Fig. 3.2). Uncorrelated fluctuations of the residuals around zero represent a model being in good agreement with the observation. The increase of the statistical uncertainties of the differences with the half-lives is attributed to the constant sample size of  $2 \cdot 10^6$  decays for each simulation. The fraction of the daughter component of the total spectrum becomes larger with an increasing half-life of the parent component when a fixed time window of 20 s is considered in the simulations. Hence, the number of actual parent decays which contribute to the half-life fit decreases being reflected in higher statistical uncertainties. As self-consistency of the method is evident, the half-life of  $^{98}\text{Cd}$  is determined in order to show that precisely and accurately known half-life values can be reproduced ( $\rightarrow$  Fig. 3.3). At first, the half-life was derived by considering all decay correlations within a time window of 30 s. The fit model includes a constant background, the decay component of  $^{98}\text{Cd}$  and the daughter decay of  $^{98}\text{Ag}$  which has a half-life of 47.5(3) s [Nat16a]. Contributions starting from grand daughter decays are negligible as the half-life of the

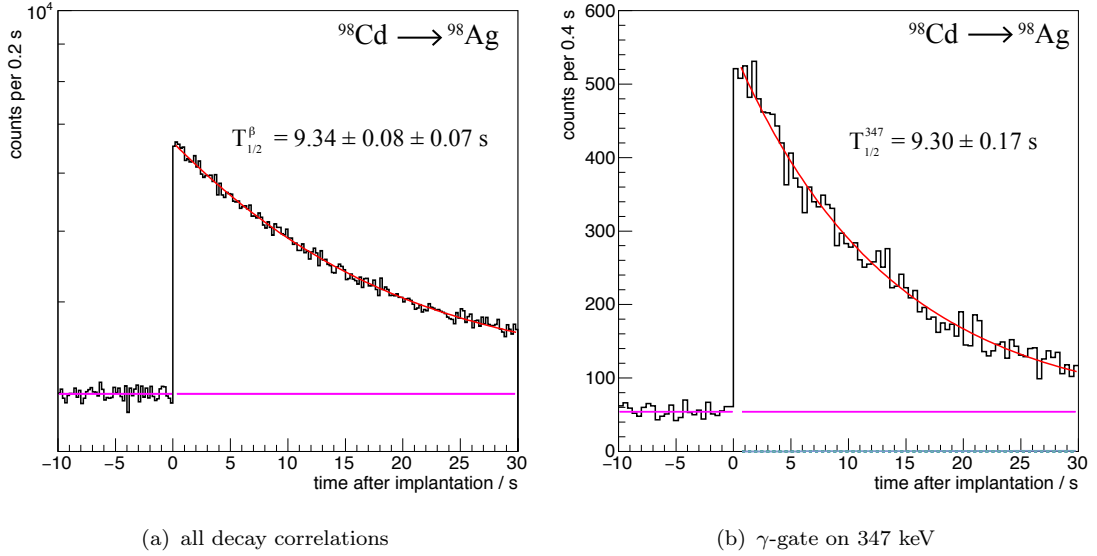


**Figure 3.3:** Determination of the half-life of  $^{98}\text{Cd}$  as a benchmark test with a model which considers the parent and daughter component as well as a constant background (magenta). The fit result is shown in red. a) Time spectrum from all implantation-decay correlations within a single detector pixel. The uncertainties are associated with those of the fraction of electron capture and the statistical uncertainties, respectively. b) Half-life fit by requiring coincident  $\gamma$ -emission with an energy of 347 keV from the daughter nucleus  $^{98}\text{Ag}$ .

grand daughter is already 17.7 min [Nat16a]. The half-life results in  $9.34 \pm 0.08 \pm 0.07$  s. The systematic uncertainty is dominated by the precision of the known  $Q_{\beta}$ -value and a resulting branching ratio for the electron capture channel which modifies the contribution of the daughter component. Secondly, the half-life was determined by requiring  $\gamma$ -emission from the de-excitation of the daughter nucleus  $^{98}\text{Ag}$  with an energy of 347 keV. In this case the fit of the half-life results in  $9.30 \pm 0.17$  s. Both values are consistent with the literature value of 9.2(3) s [Pl+92].

### 3.1.6 The Background Evaluation

Decay products of previous implantations and radioactivity within the detector structure contribute to the decay events depending on the intensity of the secondary beam. The background rate was determined by studying the number of decay events which has occurred before the implantation. As the time window is small compared to the time when beam intensity has changed, this rate is assumed to be constant. The background rate was determined by the implantation history and this result is used as a fixed component in the actual half-life fit. In the first approach, the background rate is determined by a constant fit while in the second approach, the p.d.f of the background is given by the Poissonian distribution describing the probability to find  $r$  background events in a time window  $t_c$  with a background rate  $\lambda_{\text{bgd}}$  ( $\rightarrow$  Sec. 3.1.4). The background rate of a pixel is determined to  $\lambda_{\text{bgd}} = 0.04 \frac{\text{cts}}{\text{pixel}\cdot\text{s}}$ .

## 3.2 Event Discrimination of Implantation and Decay Events

In this experimental setup, exotic nuclei were produced by fragmentation of a stable beam and implanted into Si-detectors for decay spectroscopy ( $\rightarrow$  Cpt. 2). Regarding the different nature of decays and implantations, the events are distinguished by their pulse shapes, multiplicities and the trigger logic. With regard to a positron tracking the identification of different types of radiation within the Si-detectors are discussed.

### 3.2.1 Implantation & Decay

Nuclei are identified during their flight through the BigRIPS separator using also the beam tracking detectors which are positioned in the focal plane F11 just in front of the implantation setup. Since the geometry of the beam-line and the time-of-flight of fragments are well-described, the corresponding identifications from the BigRIPS DAQ and WAS3ABi/EURICA DAQ are sharply correlated in time. Implantation events differ from decay events by 1) the trigger at F11, 2) the number of strips in Si-detectors which show energy deposit, and 3) the energy amplitudes. Ultimately, events are discriminated by the first condition. Besides the fragments of interest, light particles are produced in the abrasion-stage as discussed in Chapter 2. Those with the correct magnetic rigidity reach the detector plane of WAS3ABi. The energy loss of these particles in the TEGIC detector at F11 is below the trigger threshold that they are not identified as an implantation of an ion. However, due to a large penetration depth, the light particles are very likely to pass the whole bunch of Si-detectors which is identified by a veto detector. If light particles have not reached the veto detector, they are another source of background which is identified by their straight track through the Si-detectors with a characteristic energy deposit of  $\sim 1$  MeV in at least eight layers. This also allows them to be removed from the analysis, improving the signal-to-noise ratio ( $\rightarrow$  Fig. 3.6).

### 3.2.2 Positrons & Protons

After discrimination of all events from particles being injected after passing the BigRIPS separator, the remaining events comprise  $\beta$ -decays, proton emissions and  $\gamma$ -emissions resulting in an energy deposit in the Si-detectors while the environmental background from cosmic radiation is very little. In particular, the absorption and scattering cross sections for  $\gamma$ -emission in the Si-detectors are small. However, the contribution to the detector response is not negligible which is discussed below. The energy deposit of  $\beta^+$ -particles and protons in Si-detector strips as derived from a **Geant4**-simulation ( $\rightarrow$  Sec. 3.4) are shown in Figures 3.4. Protons with an energy of 1.9 MeV are stopped within a single strip in either direction while positrons are likely to pass several strips or layers until they are stopped. The fraction of 1% of the protons which has multiplicity 2 in a single detector is attributed to events which are very close to a neighboring strip. Thus, proton events are selected by requiring an energy deposit of  $E_{\text{strip}}^{x,y} > 1500$  keV in both detector readouts, X and Y (single pixel energies). Since  $\beta$ -delayed protons originate in the proton decay from an excited state well above the proton separation which is populated by a  $\beta$ -decay, the energy deposition in these events contains a contribution which is

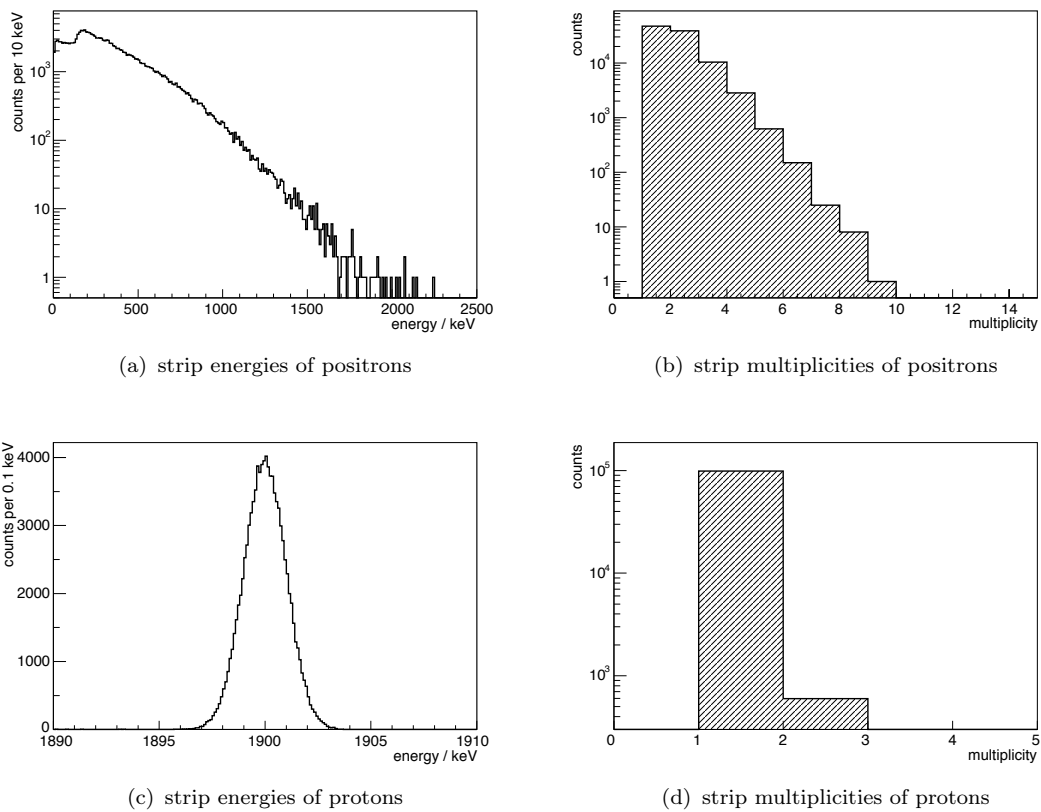


**Figure 3.4:** a) Simulated energy deposit of  $\beta^+$ -particles in a single strip for a Gaussian distribution with  $\mu = 1.9$  MeV,  $\sigma = 0.1$  MeV. The spatial distribution is homogeneous throughout the detector plane which was placed in the center of the middle implantation detector ( $\rightarrow$  Fig. 3.5). b) Number of strips showing energy deposit above  $E_{\text{thr}} = 100$  keV. c) Simulated energy deposit of protons in a single strip for a Gaussian distribution with  $\mu = 1.9$  MeV,  $\sigma = 0.01$  MeV. The spatial distribution is homogeneous throughout the detector plane which was placed in the center of the middle implantation detector ( $\rightarrow$  Fig. 3.5). d) Number of strips showing energy deposit above  $E_{\text{thr}} = 100$  keV.

associated with the emitted positron in the same strip. Events in the same energy range as  $\beta p$ -events but without a track of a positron are candidates for a direct proton decay. However, the energy distribution or coincident  $\gamma$ -emission is utilized to decide on the character because the positron could be hidden in the same pixel. Since direct protons can also occur at energies in the range of  $\beta$ -particles (e.g.  $^{94}\text{Ag}$ ), they populated a peak in this range. Hence, the WAS3ABi-setup enables the study of the decay channels  $\beta$ ,  $\beta p$  and proton radioactivity, each of which is present in the region around  $^{100}\text{Sn}$ . If the number of correlations is sufficiently high, ultimately coincident  $\gamma$ -emission is used to confirm a decay channel. The use and analysis of  $\gamma$ -emission in the daughter nucleus is explained in the next section.

## 3.3 The Correlation Technique for Implantation and Decay Events

Events are discriminated as described in the previous section. Correlating  $\gamma$ -radiation with implantation or decay events is essential with regard to the unambiguous identification of the PID of implantations or to associate the observed decays. The observables of the corresponding decay channels can be correctly extracted. As events were recorded in different DAQs, the correlation of the independent DAQ systems was managed by the assignment of a unique timestamp to each recorded event. Then, the implantation as well as the PID are easily correlated since the delay between events within the BigRIPS and WAS3ABi data acquisition systems is well-known from the simulation of the separator with the transmission tool LISE++. Eventually, the implantations are correlated with subsequent decay events by their timestamps which takes advantage of the high granularity of the Si-detectors that the time between two subsequent implantations into the same pixel is significantly extended.

### 3.3.1 Isomeric Transitions

In fragmentation reactions, a large amount of angular momentum and energy can be transferred to the heavy residue. The resulting nuclei are produced in their ground states as well as in excited states. The fraction of a species which is generated in its excited states, depends on the production mechanism. During the decay of the initially populated excited states, the decay cascades can decay to the ground state or populated isomeric states. If the half-life of the isomeric state is sufficiently long, the fragment can be implanted in WAS3ABi while being in the isomeric state and will decay after the implantation. This will allow for the study of the half-life,  $\gamma$ -transitions and decay branches of the isomer while other decay modes (e.g. proton-decay) are also possible in some cases. When the implantation has triggered the DAQ, a gate for  $\gamma$ -detection is open for 100  $\mu\text{s}$  for the EURICA detectors. Gamma-radiation which originates in the de-excitation of isomeric states is detected and the time of the radiation detection after the implantation is measured. Then, the half-life of isomeric states is extracted from the measured decay curve. Furthermore, the analysis of the  $\gamma$ -spectra and  $\gamma$ - $\gamma$ -coincidences allows to study the excited states of the implanted nucleus which are populated by the decay of the isomer.

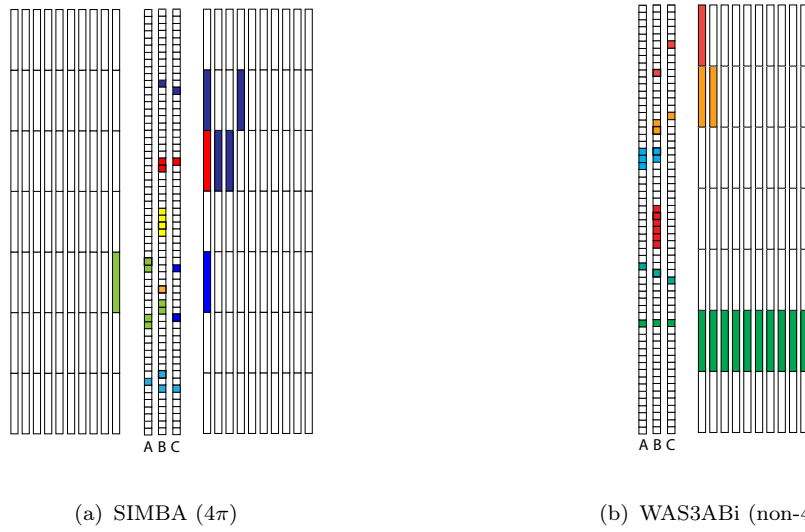


**Figure 3.5:** Sectional view of the Si-detectors in the SIMBA and WAS3ABi setups. Channels marked with the same color belong to one event. Squares in bold show the implantation position. A corresponding simulation output to study multiple-scattering and energy deposition in the WAS3ABi array is shown in Figure 3.6.

### 3.3.2 Detection of the $\beta$ -Decay

In contrast to  $\gamma$ -emission,  $\beta$ -decays are detected within the same detector in which the implantation was recorded. Since decay products of previous implantations remain unstable, they continuously keep on triggering the Si-detectors resulting in background events. The positron of the  $\beta^+$ -decay starts at the position of the implantation. In most cases the decay signal is observed in the same pixel where the implantation was recorded. If the implantation is close to the strips' border, the neighboring strip may trigger the data acquisition rather than the strip of its origin. Therefore, a spatial condition is applied that  $\beta$ -decays correlated to an implantation need to be within the range of a few neighboring strips relative to the position of implantation resulting in a  $3 \times 3$  spatial correlation matrix. A reduction of this window to single pixel correlations  $1 \times 1$  causes a loss in the number of true correlations but minimizes the background and improves the signal-to-noise ratio. The detection efficiency of the single pixel correlation is  $\epsilon_{\text{det}}^{\text{1pix}} = 0.57$ . The analysis of the implantation depth reveals that no less than 94% of the  $N=Z$  nuclei were implanted into DSSD B and the implantation plane is almost at this detector's center ( $\rightarrow$  Tab. 2.2). Therefore, implantations and correlations in DSSD A and DSSD B were neglected in the  $Q_\beta$ -analysis because the increase of the systematic uncertainties is higher than the decrease of the statistical uncertainties. Furthermore, in the study of the  $Q_p$ -values from the  $\beta p$ -branch in  $^{98}\text{In}$ , the energy loss of positrons in single strips has to be considered to extract the energy of the proton because both, the  $\beta^+$ -particle and the proton deposit their energy in the same detector area as they originate from the same implantation. This is corrected by the mean energy loss of  $\beta^+$ -particles in single strips of  $\bar{E} = 337$  keV which is obtained by considering a **Geant4**-simulation with a spatial distribution and energy distribution of  $^{98}\text{Cd}$  ( $\rightarrow$  Sec. 3.4).

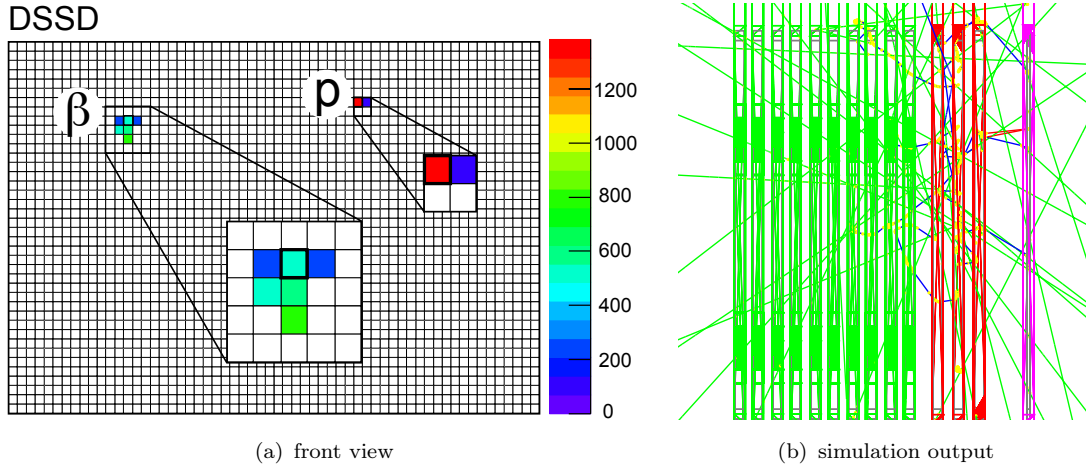


**Figure 3.6:** Schematic front view for energy deposit of events in a single DSSD-detector and visual output of the *Geant4*-simulation of the WAS3ABi setup. The front view shows characteristic energy distributions of  $\beta$ - and  $\beta p$ -decays which are used to discriminate these decay channels. The simulation shows how positrons scatter within the detector structure (blue) and  $\gamma$ -emission by bremsstrahlung and annihilation (green). The vertical lines in green, red and magenta represent the SSSD, DSSD and XY-detectors, respectively.

## 3.4 Determination of $Q_\beta$ -Values

The  $Q_\beta$ -value is the observable which has the strongest influence on the determination of the transition strength  $\mathcal{B}_{GT}$  because the phase space integral  $f(Z', Q_\beta)$  scales with the fifth power of  $Q_\beta$  where  $Z'$  denotes the proton number of the daughter nucleus. Ideally, the total energy of a decay positron would be reconstructed by summing the energies of all interactions of the positron in the detectors. However, since the detector provides only partial solid angle coverage, this is clearly not possible. Hence the detector response has to be carefully studied using a *Geant4*-simulation [Ste09]. In case of a  $4\pi$ -geometry, the deviation between the actual  $Q_\beta$ -spectrum and the experimental spectrum due to bremsstrahlung and annihilation radiation is small. However, even in this case the shape of the spectrum is altered and it is important to study the influence of this effect on the  $Q_\beta$ -value. Additionally, the shape of the energy spectrum of  $\beta^+$ -particles is dominated by partially absorbed positrons due to the asymmetric detector geometry of the WAS3ABi. Therefore, a  $\chi^2$ -test is introduced to derive the  $Q_\beta$ -value from a comparison of experimental and simulated spectra.

### 3.4.1 Positron Tracking & The Detector Response

The standard method to determine the  $Q_\beta$ -value of a certain decay is given by the measurement of the complete spectrum of electrons or positrons which are distributed according to the Fermi function. Hence, the experimental spectrum which is obtained by summation of all single strip energies throughout the detector is compared to the three-particle kinematics. An experimental solution was given by the calorimeter of the SIMBA-setup ( $\rightarrow$  Fig. 3.5). The implantation detectors are surrounded by two  $\beta$ -absorbers and  $\beta^+$ -particles with energies up to 5 MeV are stopped enabling the determination of  $Q$ -values in the range of up to 10 MeV [Ste09; Hin10; Mos+15; WBM15] implying a  $4\pi$ -geometry for positrons which originated from the  $\beta$ -decay of  $^{100}\text{Sn}$ . However, at the RIBF facilities the primary beam energy reaches only 345 A MeV (compared

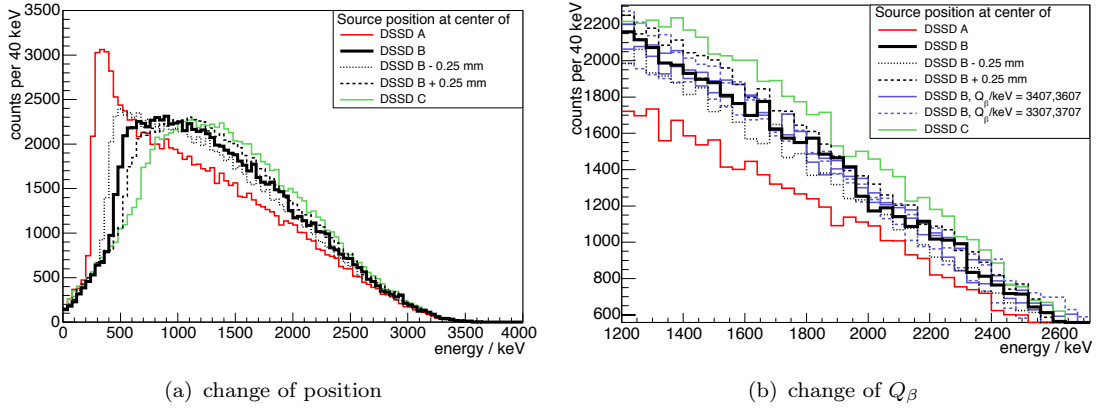


**Figure 3.7:** Analysis of the effect on the energy distribution by a variation of the position of the positron source in Z-direction. a) Variation of the implantation plane with an input spectrum with  $Q_\beta = 3507$  keV. b) Comparison of the variation of the position with the variation of  $Q_\beta$  by 100 keV and 200 keV, respectively.

to 1 AGeV at the FRS of GSI). This is not sufficient to penetrate a  $\beta$ -calorimeter in front of the implantation detectors. Thus, the  $4\pi$ -coverage is not available in the present experiment and even  $\beta^+$ -particles at low energies ( $\sim 300$  keV) can leave the detector depending on the direction of emission. The restriction of the event selection to a single detector will not solve the problem since  $\beta$ -particles with energies  $E_\beta = 500$  keV already scatter around different detector layers and the  $Q_\beta$ -spectrum would be distorted. Contrarily, demanding the first layer to not show energy deposit, when summing up energies from closed tracks to the opposite direction, applies a bias to the  $Q_\beta$ -spectrum because low energy positrons might be collected completely until DSSD A whereas the fraction of losses for high energy positrons is unknown. Examples of tracks from the simulation and the occurrence of multiple-scattering are shown in Figure 3.6.

The study of the spatial distribution of  $\beta^+$ -particles reveals that multiple-scattering between different detector layers and energy deposited by bremsstrahlung and annihilation radiation cannot be discriminated by a pattern analysis. The distances between groups of neighboring strips is shown in Figure 3.9(a) where a group of strips is defined by neighboring strips with an energy deposition above the threshold energy  $E_{\text{thr}}$  in each strip. In both cases, when strip groups are considered within the same detector or across adjacent detectors, a considerable fraction of events shows gaps between groups of strips by more than two strips. Furthermore, the simulation shows that gaps between the Si-detectors themselves of around 1 mm are another source of particle escape which is also possible for positrons starting from rather central regions in the Si-detectors ( $\rightarrow$  Fig. 3.6). Therefore, the distances between strip groups across detectors are not a proper measure for positron tracking and a pattern analysis is not applicable. Hence, the detector response has been studied using simulations, which depends on the energy of the positrons and on the position of implantations in the WAS3ABi detectors. The experimental distribution in each of the spatial detector coordinates was used in order to generate a source for the decay positrons concerning a realistic simulation ( $\rightarrow$  Fig. 3.8(a)). Additionally, the effect of a change of the source plane is studied in Figure 3.7. Only by a shift of more than 0.25 mm from the center of detector DSSD B, the detector response starts changing strongly. Therefore, the source plane was placed at the detector center in good approximation. Even though the contribution of bremsstrahlung and annihilation

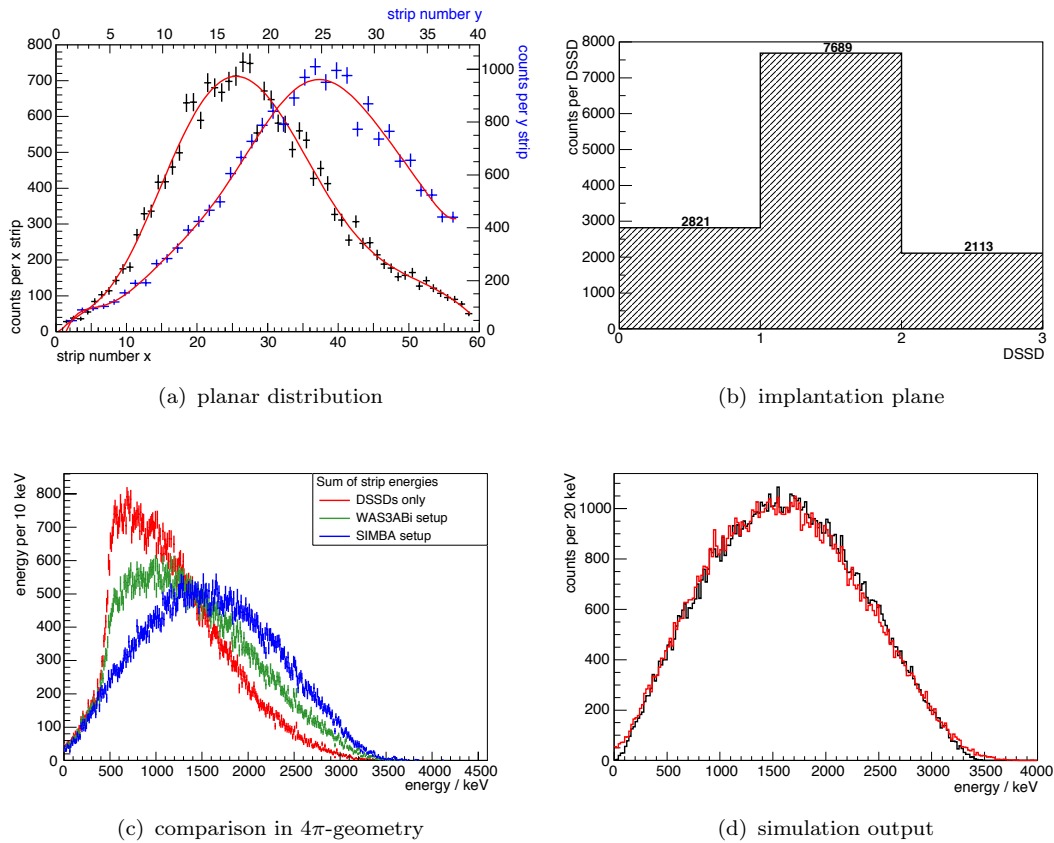


**Figure 3.8:** a) Horizontal and vertical distribution of implanted  $^{98}\text{Cd}$  ions serving as input for the **GEANT4**-simulation. b) Distribution of the energy deposition from decay events throughout the DSSDs if the correlated ion was implanted into DSSD B. c) Simulation output when summing up the energy deposit in the DSSD detectors only (red), according to the WAS3ABi setup (blue) and according to the SIMBA setup (green) d) Comparison of the simulation input and output in a  $4\pi$ -geometry (SIMBA) to study the effect of bremsstrahlung and annihilation radiation. The input source was a point source at the center of DSSD B.

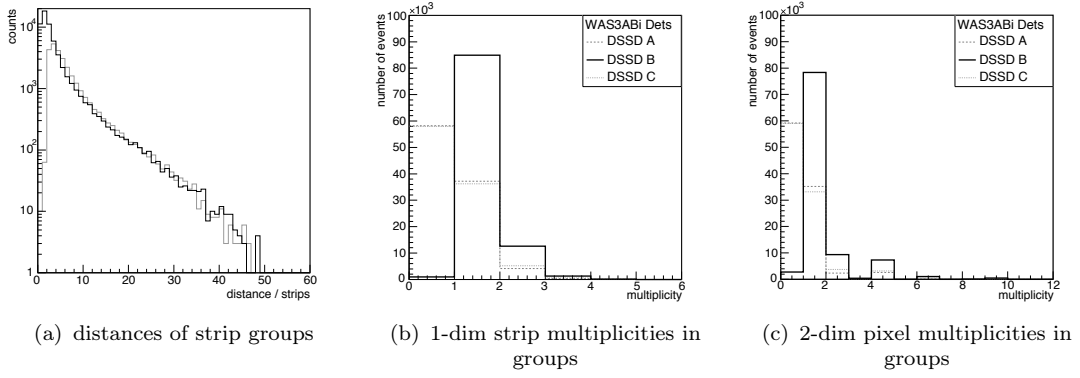


**Figure 3.9:** The analysis of multiple-scattering of  $\beta^+$ -particles across the Si-detectors layers shows that a large fraction of decay events cannot be discriminated by a coherent track in the WAS3ABi-detectors. a) Size of gaps between different strip groups within the same DSSD (black) and across neighboring detectors (gray). b,c) The size of coherent groups of strips in terms of strips.

radiation is small compared to the uncertainty introduced by incomplete energy deposition, a systematic uncertainty of  $\sim 200$  keV was introduced in the experiments using the SIMBA setup. In the present work, this uncertainty is treated because the physical effects are taken into account by the simulation. The differences of the input and output spectrum which is only distorted by bremsstrahlung and annihilation radiation is shown in Figure 3.8(d).

Secondly, the simulation was used to compare the response functions of the WAS3ABi and SIMBA geometries. The complete energy deposit within DSSD and SSSD detectors was determined. Energies of each strip were summed up and the result is shown in Figure 3.8(c). As an exercise, the sum of single strip energies, which considers only DSSD detectors, was also determined. It is obvious how the escape of positrons drives the shape of the spectrum and a fit of the input  $Q_\beta$ -spectrum with  $Q_\beta = 3507$  keV is unfeasible without a simulation.

### 3.4.2 The $\chi^2$ -Method

Previously, arguments were given that the detector response is non-trivial due to the calorimetric properties of the setup. Figure 3.8(a) shows the spatial distribution of implantations in X- and Y-direction with Gaussian centroids by  $\mu_x = 26.3$  mm,  $\sigma_x = 10.2$  mm and  $\mu_y = 25.2$  mm,  $\sigma_y = 9.6$  mm, respectively. Regarding the simulation input, the spatial distribution of implantations throughout the detector was approximated by using a high order polynomial. The mean implantation depth in DSSD B was derived by the analysis of the energy deposit in its neighboring detectors using its correlated decay events ( $\rightarrow$  Fig. 3.5). Supposing the isotropic angular distribution of  $\beta^+$ -particles, the asymmetry  $\eta$  in the number of events which show energy deposit in either DSSD A or DSSD C was used as a measure for how far from the detector center nuclei are stopped. The asymmetry is defined by  $\eta = \frac{N_A - N_C}{N_A + N_C}$  yielding  $0.44 \pm 0.02$  mm for the mean implantation depth in DSSD B for  $^{98}\text{Cd}$  with an uncertainty which originates from the statistical uncertainty of the number of events with energy deposition in either DSSD A or DSSD C. Therefore, the source plane was placed at the center of DSSD B in good approximation with a Gaussian distribution in X- and Y-direction. The probability distribution of positrons is given by the phase space function of the transition rate of

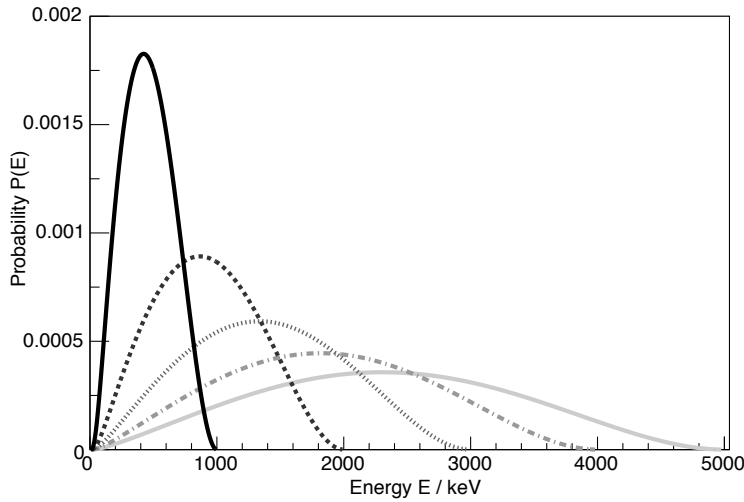


**Figure 3.10:** Phase space distribution of the  $\beta^+$ -particles with an  $\beta$ -endpoint energy of 1 MeV to 5 MeV.

the  $\beta$ -decay

$$p(\epsilon, \epsilon_0) = N \cdot \epsilon \sqrt{\epsilon^2 - 1} (\epsilon_0 - \epsilon)^2 \cdot \mathcal{F}(Z', \epsilon_0) \quad (3.20)$$

with the normalization constant  $N$  given by  $\int_{\epsilon_{\min}}^{\epsilon_{\max}} p(\epsilon, \epsilon_0) = 1$ , and  $\epsilon = (\epsilon_i)$  denotes the set of measured energy depositions.  $\epsilon_0 = Q_\beta$  denotes the  $\beta$ -endpoint energy which is the free fit parameter. Finally,  $\mathcal{F}(Z, \epsilon)$  represents the  $Q$ -dependent and  $Z$ -dependent Fermi-function which accounts for Coulomb effects between the positrons and the daughter nucleus ( $\rightarrow$  Fig. 3.10). It was analytically derived by Fermi [Fer34] and an approximation for non-relativistic particles was derived by Mott and Massey [MM33] as

$$\mathcal{F}(Z', \epsilon) \approx \frac{2\pi\nu}{1 - e^{-2\pi\nu}} \quad \nu = -\frac{Z'\alpha}{v_\beta/c} \quad (3.21)$$

where  $\alpha$  is the fine-structure constant and  $v_e$  is the velocity of the emitted  $\beta^+$ -particle. The energy distribution is simulated according to this distribution for the number of present  $Q_\beta$ -components, correspondingly. If more than one decay channel contributes to the positron spectrum, they are considered according to their branching ratios. The simulated spectra are normalized to the number of events in the background corrected experimental spectrum and compared to the experimental spectrum by a  $\chi^2$ -test for each value of  $Q_\beta$

$$\chi^2 = \sum_{i=k}^n \frac{|f_s(\epsilon) - f_e(\epsilon)|^2}{\sigma_e^2(\epsilon)} \quad (3.22)$$

where  $f_{s,e}(\epsilon)$  describes the simulated (s) and experimental (e) distribution at the positron energy  $\epsilon$ , correspondingly. They are obtained by summing up the single strip energies throughout the Si-detectors.  $f_e(\epsilon)$  is corrected for the background contribution by subtracting a  $Q_\beta$ -spectrum which is obtained from negative time correlations normalized to the time range of correlations which are positive in time. The comparison runs from the  $k$ -th to the  $n$ -th bin which is the *range of interest*, the nominator is the squared difference of simulated and experimental bin contents and  $\sigma_e$  is the statistical uncertainty of the experiment. The standard deviation  $\sigma_e$  is the Gaussian sum of the uncertainties of

the  $Q_\beta$ -spectrum generated by decay correlations positive in time and of the background spectrum. The simulation is treated to be statistically exact as the size of the simulation population  $N = 10^5$ . However, the standard deviation of  $\chi^2$  which originates from the statistical uncertainties of the simulation is determined by performing the test with 30 different samples of the same size at a given  $Q_\beta$ -value. The  $Q_\beta$ -value which minimizes  $\chi^2(Q_\beta)$  is the best-fitting value while the  $1\sigma$  confidence interval is given by the limits  $Q_\beta^{l,u}$  which are derived by solving  $\chi^2(Q_\beta) = \chi_{\min}^2(Q_\beta) + 1$  [Cou00].

### 3.4.3 Test of the $\chi^2$ -Method with $^{98}\text{Cd}$

The method described above is tested with the rather well-known nucleus  $^{98}\text{Cd}$ . The  $0^+$  ground state of this nucleus decays dominantly into the  $1^+$ -state at 1691-keV of  $^{98}\text{Ag}$ . In literature, the  $\log(ft)$  of this transition is known as  $\log(ft)=3.3$ , corresponding to a  $\beta$ -endpoint energy of  $(2717 \pm 40)$  keV [SH03] and 2707 keV from the NNDC database [Nat16a]. Events were selected by the strong  $\gamma$ -transition from this  $1^+$ -state to the  $2^+, 3^+$ -state in  $^{98}\text{Ag}$  where the contribution of the background line at 1176 keV is negligible. This results in a  $Q_\beta$ -spectrum which represents the  $\beta$ -decay of a single decay channel.

Thus, the  $\chi^2$ -method was applied by varying the  $Q_\beta$ -value of the simulation in steps of 100 keV in the range from 2300 keV to 3200 keV where a minimum establishes around 2800 keV. The results are shown in Figure 3.12 where the minimum is approximated by a parabolic fit of the  $\chi^2$ -plot yielding  $Q_\beta = (2787 \pm 32 \text{ stat. } +10_{-150} \text{ sys.})$  keV with systematic (sys.) and statistical (stat.) uncertainties, respectively, while the systematic uncertainties are not independent of the statistical uncertainty. The former one was determined by fitting the energy spectrum with respect to different ranges ( $\rightarrow$  Fig. 3.11). Later, the same procedure is applied to the analysis of  $^{100}\text{Sn}$  in Section 4.4.1 ( $\rightarrow$  Fig. 4.23). Here, one limit of the fit range was fixed at either 400 keV or 2400 keV and the other limit was varied from either 1600 keV to 2400 keV or 400 keV to 1200 keV, respectively. The range between the minimum and the maximum of the best-fitting

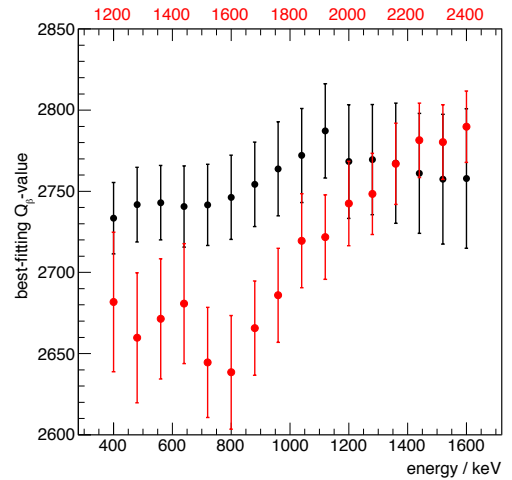


**Figure 3.11:** Analysis of the systematic uncertainty of the  $Q_\beta$ -value by varying the upper (red) and lower limits (black) of the fit range while the lower (400 keV) and upper limits (2400 keV) are fixed, respectively. The energies of the scales denote the end of the corresponding variable limit.

$Q_\beta$ -values is 300 keV. However, the largest deviations occur when the limits of the fit range reach the maximum of the experimental distribution which is very sensitive to the spatial distribution of implantations in the Si-detectors. The variation of the fit range further away from this region yields equal values within their statistical fluctuations such that the method is robust for a wide range.

Since  $\gamma$ -transitions with lower energies ( $\sim 100$  keV) are strongly converted, electrons from internal conversion also contribute to the spectrum. This is apparent by the strong enhancement at lower energies which is associated with the energy deposition by conversion electrons originating from the transition with energies of 61 keV and 107 keV in

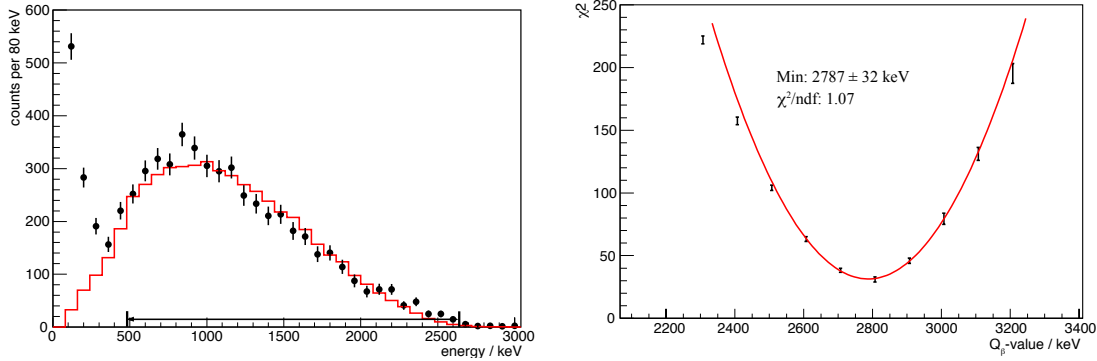


**Figure 3.12:** a) Experimental spectrum of positron energy deposit in Si-detectors (black) and a **Geant4**-simulation (red) normalized to the integral number of the experimental spectrum. The arrow marks the range of the spectra which was used for the  $\chi^2$ -test. The strong peak at lower energies is associated with conversion electrons from  $\gamma$ -transitions at 61 keV and 107 keV in  $^{98}\text{Ag}$ . b)  $\chi^2$ -values of the comparison of the experiment and simulations at different  $Q_\beta$ -values. At the minimum, the reduced- $\chi^2$  equals 1.07 and the confidence intervals are given where  $\chi^2_{\min} \pm 1$ .

$^{98}\text{Ag}$ . The total conversion coefficients are calculated with the BrIcc calculator [Nat16a] for each transition. It yields 1.78 (5) and 1.14 (3) corresponding to the probability of conversion  $I_e = \frac{\alpha_{\text{tot}}}{1 + \alpha_{\text{tot}}}$  of  $I_e^{61 \text{ keV}} = 0.640$  (6) and  $I_e^{107 \text{ keV}} = 0.533$  (6), respectively. Then, the average contribution of conversion electrons to the  $Q_\beta$ -spectrum is  $\bar{E}_e = 96$  (1) keV and the corrected  $Q_\beta^{\text{corr}}$ -value is

$$Q_\beta^{\text{corr}} = (2691 \pm 33_{\text{stat.}}) \text{ keV} \quad (3.23)$$

which is in good agreement with the literature value mentioned above. The  $\chi^2$ -method has been successfully verified and can be applied with regards to the determination of the  $Q_\beta$ -value of  $^{100}\text{Sn}$  ( $\rightarrow$  Sec. 4.4.1). However, the number of  $^{100}\text{Sn}$  nuclei is much lower so that a  $\gamma$ -gate on the transitions in  $^{100}\text{In}$  would decrease the number of available events dramatically. Therefore, in the case of  $^{100}\text{Sn}$ , the spectrum was generated from all decay correlations and the contribution by the fragmented daughter decay  $^{100}\text{In} \rightarrow ^{100}\text{Cd}$  with respect to the time window was taken into account. Thus, the probability density accounting for this is generally written as

$$p(\epsilon, \epsilon_0) d\epsilon = N' \cdot \left[ \left( f_m \sum b_i^m \cdot p(\epsilon, \epsilon_0 + O_i) \right) + \left( f_d \sum b_j^d \cdot p(\epsilon, \epsilon_0 + O_j) \right) + \dots \right] d\epsilon \quad (3.24)$$

where  $f_{p,d}$  represent the contribution of decays originating from parent (p) and daughter (d) decays, respectively, and the branching ratios of decay channels of a certain nucleus are denoted by  $b_i^{p,d}$ . Thus, if the level scheme, the branching ratios and the subsequent decay products of a nucleus are well-known, this method can be also used to determine the  $Q_\beta$ -value of any nucleus without a specific selection by using a  $\gamma$ -gate.

# 4 Decay Spectroscopy

Decay spectroscopy is a powerful tool to study isomeric states, decay schemes, reaction energies, transition rates and branching ratios. In this experiment, a large number of nuclei in the region of  $^{100}\text{Sn}$  was produced up to the most exotic species. After identification, they were implanted into the WAS3ABi/EURICA-spectrometer where the  $\beta$ -decay, the  $\gamma$ -transitions and proton-decays were studied in prompt and delayed correlations.

The main task is the determination of fundamental properties of nuclei close to the proton dripline. In particular, the Gamow-Teller transition strength  $\mathcal{B}_{\text{GT}}$  of  $^{100}\text{Sn}$  is of great interest as discussed in Chapter 1. The results of the half-life analysis, the determination of the  $Q_\beta$ -value and the implications on the level scheme of  $^{100}\text{In}$  from the decay spectroscopy of  $^{100}\text{Sn}$  are presented in this chapter. Since the number of generated nuclei was much higher than in previous experiments, the impact on the improvement of uncertainties and the results are very interesting.

## 4.1 Determination of Half-Lives

The combination of  $Q_\beta$ -values, branching ratios, excitation energies and half-life measurements yields valuable information about the transition matrix elements and binding energies in the vicinity of the  $N = Z$ -line and the proton dripline. It indicates the number of isomeric states that Fermi and Gamow-Teller transitions are distinguished in coherence with the  $\gamma$ -spectroscopy. In the vicinity of  $^{100}\text{Sn}$ , half-lives of many nuclei are either undetermined or have large statistical uncertainties and with regard to the  $\log(ft)$ -values or rp-process calculations, the accurate and precise determination of this observable is desirable. The determination of the half-lives has been performed by using the MLH method ( $\rightarrow$  Sec. 3.1.1).

### 4.1.1 $N = Z - 2$ Nuclei

The nuclear chart in this region is further extended by the observation of four  $N = Z - 2$  nuclei in this experiment. The isotopes  $^{96}\text{In}$ ,  $^{94}\text{Cd}$ ,  $^{92}\text{Ag}$  and  $^{90}\text{Pd}$  were newly discovered [Cel+16] through the particle identification of the BigRIPS separator ( $\rightarrow$  Fig.2.5). Additionally, one event was identified to be  $^{98}\text{Sn}$ . However, this event was not properly implanted into WAS3ABi as expected from LISE++ calculations [TB08] and the signal was detected in the most outer strip of the Si-detectors, indicating that the nucleus has been destroyed during the implantation. This argument accounts also for the difference between the number of identifications and implantations of the other  $N = Z - 2$  nuclei ( $\rightarrow$  Tab. 4.1). However, the other nuclei show correct implantations in the center of the Si-detectors so that improper identification can be ruled out.

Since the separation energies  $S_p$  are already negative and the proton dripline has been

predicted to be found at  $^{97}\text{In}$  [FGG13], the observation of  $^{96}\text{In}$  is particularly interesting. In a first attempt, this “stability” is explained by the  $T = 0$   $pn$ -pairing correlations which contribute to the attractive part of the interaction and the Coulomb-barrier which hinders instantaneous proton emission in  $^{96}\text{In}$ .

Regarding the event selection to determine the half-lives of the exotic species, decay

$^A\text{X}$	Identified	Implanted	Correlated	Half-Live $T_{1/2}$ / ms
$^{98}\text{Sn}$	1	(1)	0	—
$^{96}\text{In}$	2	1	1	$25_{-12}^{+119}$ (24.4)
$^{94}\text{Cd}$	6	4	2	—
$^{92}\text{Ag}$	10	3	2	$17_{-8}^{+32}$ (18.0)
$^{90}\text{Pd}$	4	1	1	$58_{-28}^{+276}$ (56.4)

**Table 4.1:** Half-lives of the  $N = Z - 2$  nuclei determined by the mean  $\tau$  of decay correlations within a time window of 200 ms after the implantation. The uncertainties of rare events are derived according to Schmidt et al. [Sch+84]. The numbers in squares are the results using the unbinned MLH-method which considers the daughter decay and a constant background rate. A complete list of the events with the corresponding correlation times is shown in Appendix D Table D.1.

events were chosen within a correlation window  $t_c < 200$  ms after the implantation under the assumption that these decays proceed much faster than their daughter nuclei. The best estimator of the lifetime  $\tau$  of the exponential distribution is given by the mean of the measurements according to the MLH-method ( $\rightarrow$  Sec. 3.1.1) and the half-life is given by  $T_{1/2} = \tau/\ln(2)$ . The complete compilation of the correlated times of the  $N = Z - 2$  nuclei is listed in Appendix D. The comparison of decay correlations being negative and positive in time with respect to the implantation shows that decay events which occur right after the implantation events are very likely to originate from the decay of the parent or a daughter nucleus of the implantation. The results of the half-lives are listed in Table 4.1 where the uncertainties of rare events are determined according to Schmidt et al. [Sch+84].

As a remark, the decay times of even-even nuclei which are associated with the corresponding nuclei are in the range of its  $\beta$ -decay daughters which show a fast component such that these correlations possibly originate from the daughter decays of  $^{94}\text{Ag}$  or  $^{90}\text{Rh}$  and the parent decay has occurred within the detector dead time of  $\sim 0.4$  ms.

### 4.1.2 $N = Z - 1$ Nuclei

$N = Z - 1$  nuclei can decay by both, Fermi and Gamow-Teller transitions. Particularly, these nuclei decay into the isobaric analogue state (IAS) of its mirror nucleus by a Fermi transition as the spin and angular momentum remain unchanged. If both, the half-life  $T_{1/2}$  and the  $Q_\beta$ -value are precisely known, the CVC can also be tested in the region around  $^{100}\text{Sn}$  or, an upper limit of the corresponding  $Q_\beta$ -value can be inferred for these nuclei with the assumption of the validity of the CVC ( $\rightarrow$  Sec. 1.4) in first approximation. However, since the nuclear spin does not vanish for these nuclei the transition between the IAS can also be mediated by a Gamow-Teller  $\beta$ -decay. Thus, the  $\mathcal{B}_{\text{F,GT}}$ -values cannot be isolated without an additional measure in this case. In particular,  $^{99}\text{Sn}$  has a closed proton shell and only one hole in its neutron shell such that this nucleus

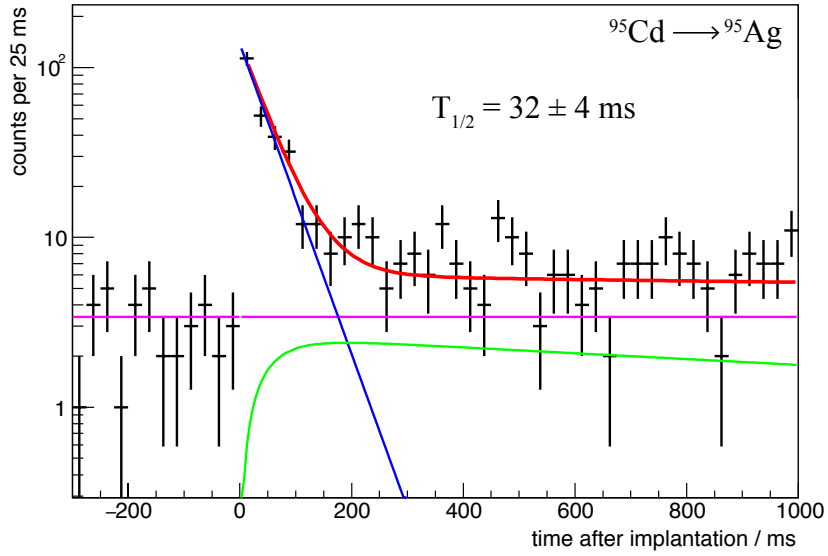


**Figure 4.1:** Half-life fit of the  $N=Z-1$  nucleus  $^{95}\text{Cd}$ . The parent, daughter and background components are shown in blue, green and magenta, respectively, while the fit result is the red curve. The resulting fits of the half-lives of all  $N=Z-1$  nuclei are shown in Figure D.4 ( $\rightarrow$  App. D).

is interesting with regards to the study of single particle energies. In this region, direct proton emission becomes competitive to  $\beta^+$ /EC-decay because the proton separation energies  $S_p$  decrease while approaching the proton dripline. In spite of a limited number of  $N=Z-1$  nuclei, the half-lives are precisely determined with unprecedented precision and the  $\beta p$ -ratios are determined as well ( $\rightarrow$  Sec. 4.1.5).

$^{93}\text{Ag}$ ,  $^{95}\text{Cd}$ ,  $^{97}\text{In}$  and  $^{99}\text{Sn}$  were newly discovered in the experiment at GSI reported by Eppinger, Hinke, et al. [EH+08], but only the half-lives of nuclei of  $^{95}\text{Cd}$  and  $^{97}\text{In}$  have been determined [SH+10] because the other nuclei have only been identified and not properly implanted. Thus, half-lives of  $^{93}\text{Ag}$  and  $^{99}\text{Sn}$  were assigned to a lower limit given by the TOF of the FRS fragment separator. In the present work, the high production rate of the RIBF allowed the determination of the half-lives of all observed  $T_z = -\frac{1}{2}$  nuclei with well-defined statistical uncertainties except for  $^{93}\text{Ag}$  because of its proton instability which will be discussed below. The half-lives are determined by using the binned MLH-method with a three-component model

$$A_{\text{tot}}(\lambda, t) = A_{\text{par}}(\lambda, t) + A_{\text{dau}}(\lambda, \lambda_d, t) + b_{\text{const}} \quad (4.1)$$

where  $A_{\text{par,dau,tot}}$  denotes the activity of the parent and daughter nucleus, respectively, as given by the solution of the Bateman Equations ( $\rightarrow$  Sec. 3.1.3).  $\lambda_d$  is the decay constant of the daughter nucleus and  $b_{\text{const}}$  denotes the constant background component which was derived from decay correlations occurring before the implantation of interest (implantation history). The background component was applied as a fixed component in the actual fit. The resulting fit in case of  $^{95}\text{Cd}$  is shown in Figure 4.1 and the half-lives of all  $N=Z-1$  nuclei are summarized in Table 4.2. The constancy of the  $\mathcal{F}t$ -values ( $\mathcal{F}t = 3072.27 \pm 0.72\text{s}$  [HT15]) implies  $Q_\beta$ -values which are equal within their statistical uncertainties meaning that the mass differences between mirror nuclei has to be very similar and pairing correlations, particularly  $pn$ -pairing, has a strong impact on the transition matrix element.

$^A\text{X}$	$Q_{\text{EC}} / \text{MeV}$	$T_{1/2}$	Literature
$^{99}\text{Sn}$	$12.6^{+0.7}_{-0.4}$	$27 \pm 6 \text{ ms}$	$> 200 \text{ ns}$ [SH+10]
$^{97}\text{In}$	$12.1^{+0.5}_{-0.4}$	$33 \pm 6 \text{ ms}$	$26^{+47}_{-10} \text{ ms}$ [SH+10]
$^{95}\text{Cd}$	$12.2^{+0.4}_{-0.3}$	$32 \pm 4 \text{ ms}$	$73^{+53}_{-28} \text{ ms}$ [SH+10]
$^{93}\text{Ag}$	$12.6(7)^\#$	—	—
	$1.05^*$	$228 \pm 16 \text{ ns}$	$> 200 \text{ ns}$ [SH+10]
$^{91}\text{Pd}$	$12.1^{+0.5}_{-0.4}$	$33 \pm 4 \text{ ms}$	$> 1 \mu\text{s}$ [Nat16a]

**Table 4.2:** Summary of the half-lives of  $N = Z - 1$  nuclei fitted by the binned MLH-method. The hashed  $Q_{\text{EC}}$ -value of  $^{93}\text{Ag}$  is calculated by considering the mass differences to its  $\beta$ -decay neighbor [WAW+12] serving as an upper limit. The  $Q$ -value with an asterisk is the  $Q_p$ -value for the proton decay of  $^{93}\text{Ag}$  derived from the relation between half-lives and  $Q_\beta$ -values according to Delion, Liotta, and Wyss [DLW06].

### Analysis of $^{93}\text{Ag}$

Along the  $N = Z - 1$  line, one observes a deficit in the number of identifications of  $^{93}\text{Ag}$  in the PID plot ( $\rightarrow$  Fig. 2.5) which obviously deviates from the trends of less exotic nuclei. Moschner et al. [Mos+15] has already pointed out that  $^{93}\text{Ag}$  decays possibly by direct proton emission, resulting in  $^{93}\text{Ag}$  decaying already during its flight and the arriving fragments must be the daughter nuclei of  $^{92}\text{Pd}$ . Thus,  $^{93}\text{Ag}$  is removed by the cleaning cuts in the PID of the BigRIPS separator when its charge-state changes or being deflected away from the implantation detectors resulting in less implantations than expected ( $\rightarrow$  Sec. 2.3)

Accordingly, a half-life fit of decay events which correlates with the PID of  $^{93}\text{Ag}$  should result in the half-life of the  $^{92}\text{Pd}$  which is reported as  $0.7^{+0.4}_{-0.2} \text{ s}$  [Wef+00],  $1.0^{+0.3}_{-0.2} \text{ s}$  [Wef+07] and measured as  $1.25 \pm 0.03 \text{ s}$  in this experiment ( $\rightarrow$  Sec. 4.1.3). The fit of the decay curve ( $\rightarrow$  Fig. 4.3) from the experiment yields  $T_{1/2}(^{93}\text{Ag}) = (1.66 \pm 0.50_{\text{stat.}} \pm 0.06_{\text{sys.}}) \text{ s}$ . The high statistical uncertainty arises due to the small number of implantations with the PID of  $^{93}\text{Ag}$  and the systematic uncertainty arises from different half-lives of the slow daughter component which are known for the decay of  $^{92}\text{Rh}$  ranging from 2.9 s to 5.6 s. Nevertheless, this result is in agreement with the value of the half-life of  $^{92}\text{Pd}$  and certainly different from  $\sim 30 \text{ ms}$  which would be expected for the  $\beta$ -decay from the  $Q_\beta$ -value analysis.

Therefore, the half-life of  $^{93}\text{Ag}$  could not be derived from the decay spectroscopy. Assuming that the ratio of identified neighboring nuclei with the same  $T_z$  is constant for  $N = Z$  and  $N = Z - 1$  nuclei, the half-life is determined by the number of nuclei which have

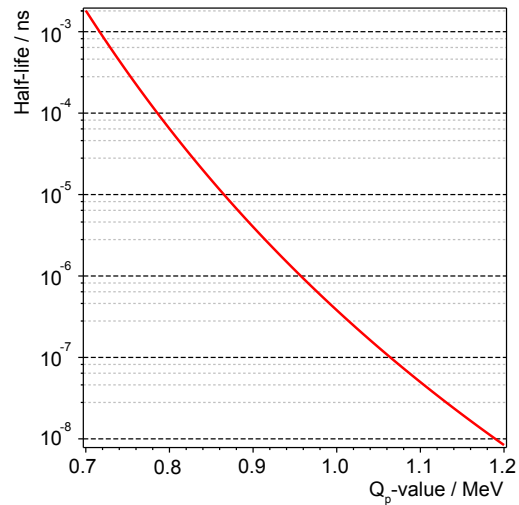


**Figure 4.2:** Extrapolation of the  $Q_p$ -value of  $^{93}\text{Ag}$  by exploiting the correlation of the  $Q_p$ -value and the reduced half-life according to Delion, Liotta, and Wyss [DLW06] in analogy to the Geiger-Nuttall law.

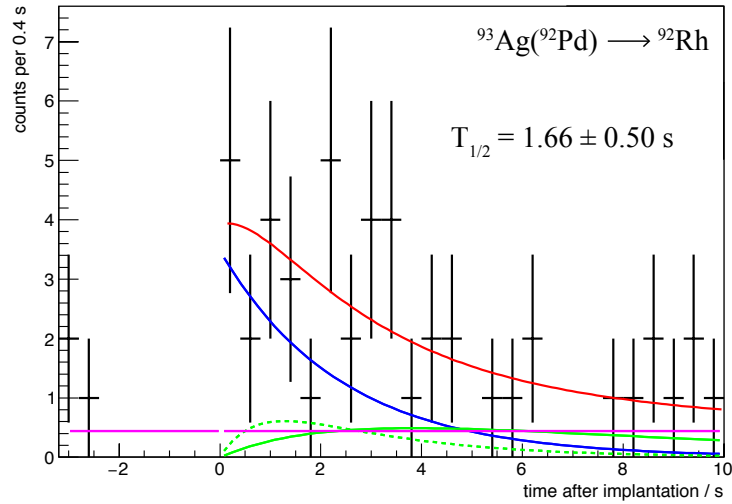


**Figure 4.3:** Determination of the half-lives of the decay products which correlate with implantations of  $^{93}\text{Ag}$ . The daughter component which is shown in the fit uses the half-lives of the corresponding decay channels of  $^{92}\text{Rh}$  as used in the determination of the half-life of  $^{92}\text{Pd}$  ( $\rightarrow$  Sec. 4.1.3). The fit result, the parent component, the daughter component and the background component are represented by the red, blue, green and magenta curves, respectively. The dashed and solid green lines correspond to different decay channels of  $^{92}\text{Rh}$ .

arrived at the detector plane and the number of actually produced nuclei by Celikovic et al. [Cel+16] who reports  $T_{1/2}^{\text{p}} = 228 \pm 16$  ns.

The  $Q_p$ -value is derived by the correlation of the so-called reduced half-life  $T_{1/2}^{\text{red}}$  and the Coulomb parameter  $\chi$  which depends on the  $Q_p$ -value according to Delion, Liotta, and Wyss [DLW06]. The resulting relation between the actual half-life  $T_{1/2}$  and  $Q_p$  is shown in Figure 4.2. It yields  $Q_p = 1.05$  MeV which compares with the estimated proton separation energy  $S_p = -1.5 \pm 0.7$  MeV [WAW+12]. Since the  $\beta$ -decay of  $^{93}\text{Ag}$  is not observed in the experiment the  $Q_\beta$ -value is estimated from the mass differences calculated in AME2012 [WAW+12]. It yields  $Q_\beta^{\text{AME}} = 12.9(7)$  MeV. Another estimate is derived from the Coulomb displacement energies<sup>1</sup> between isobaric analogue states which correlates with the ratio of  $Z/A^{1/3}$  where  $Z$  is the mean proton number of the isobaric pair and  $A$  the mass number [APB97]. The correlation is linear and the coefficients are isospin-dependent which results in  $Q_\beta^{\text{Coul}} = 12.4(1)$  MeV. These numbers are consistent with the  $Q_\beta$ -values of the other  $N = Z - 1$  nuclei.

### 4.1.3 Even-Even $N = Z$ Nuclei

The half-lives of  $^{100}\text{Sn}$ ,  $^{96}\text{Cd}$  and  $^{92}\text{Pd}$  are particularly interesting. They show a clear  $m$ -pairing effect as the ground state of all three even-even nuclei is  $0^+$  which has to decay by a Gamow-Teller transition to particle-hole  $1^+$ -states in the  $\pi g_{7/2}$  and  $\nu g_{7/2,9/2}$ -shells. The half-life of  $^{100}\text{Sn}$  is the first input in the calculation of the Gamow-Teller transition strength which is determined in Section 4.4.2. The half-lives of the ground state and the  $16^+$  high-spin isomeric state of  $^{96}\text{Cd}$  gain attraction as this nucleus is the last waiting point in the rp-process before it terminates in the SnSbTe-cycle. Finally, the half-life of  $^{92}\text{Pd}$ , which is not precisely known yet, is determined serving as a benchmark for future improvements with regard to  $^{100}\text{Sn}$ .

<sup>1</sup>The Coulomb displacement energy  $\Delta E_C$  is the energy difference of two nuclei which is attributed to the difference in their nuclear charge. It is defined by  $\Delta E_C = M_{Z>} - M_{Z<} + \Delta_{\text{nH}}$  with the masses  $M_{Z>}$  and  $M_{Z<}$  of the nucleus with larger and smaller  $Z$  and the neutron-hydrogen mass difference  $\Delta_{\text{nH}}$ .

### Analysis of $^{100}\text{Sn}$

$^{100}\text{Sn}$  is the heaviest doubly-magic proton-bound  $N=Z$  nucleus in the nuclear chart. The shells of the  $N=Z=50$  nucleus, magic in proton and neutron numbers, are completely filled up to  $g_{9/2}$ . The shell structure and the properties of  $^{100}\text{Sn}$  are described in detail in the introduction ( $\rightarrow$  Sec. 1.3). Isomeric states of  $^{100}\text{Sn}$  have not been observed yet which are expected to be very short-lived in the order of nanoseconds and an isomeric  $6^+$  state would be rather a proton emitter ( $\rightarrow$  Sec. 4.3). Thus, only the decay of the ground state is observed resulting in a decay curve which is shown in Figure 4.4(a). Implantation and decay events were correlated within  $t_c = 15$  s in time and within 1 pixel, spatially. As the daughter nucleus  $^{100}\text{In}$  was determined to decay by 5.8(2) s in this experiment, consistent with previous measurements [Sze+95; Sch+95; Ple+02; Lor+12; Nat16a] and the grand daughter  $^{100}\text{Cd}$  decays by 49.1(5) s [Ple+02], only the daughter component contributes significantly to the correlation spectrum. The Bateman-Equations ( $\rightarrow$  Eqn. 3.15) determine the evolution of a population if each event of the parent and daughter components is present. However, different branching ratios of electron capture, which competes with the  $\beta^+$ -decay, in the corresponding components alter the observed fractions in the experimental spectrum. In case of the  $\beta$ -decay of  $^{100}\text{Sn}$ , the decay to the daughter nuclei  $^{100}\text{In}$  and  $^{100}\text{Cd}$  shows branching ratios for electron capture by 11.5% and 15.1% [Nat16b; Ple+02], respectively. This is taken into account by introducing an efficiency factor  $\epsilon_{\text{EC}} = (1 - b_{\text{EC}})$  which represents the losses by unobserved electron capture decays ( $\rightarrow$  Sec. 3.1). Hence, the total activity  $A_{\text{tot}}$  is described by the sum of a constant background component  $b_{\text{const}}$ , the parent and the daughter activities  $A_{\text{par,dau}}$  with the decay constant of the daughter nucleus  $\lambda_d$

$$A_{\text{tot}}(\lambda, t) = (1 - b_{\text{EC,par}}) \cdot A_{\text{par}}(A_0, \lambda, t) + (1 - b_{\text{EC,dau}}) \cdot A_{\text{dau}}(A_0, \lambda, \lambda_d, t) + b_{\text{const}} \quad (4.2)$$

with two free parameters, the amplitude  $A_0$  and the decay constant of the parent nucleus  $\lambda$ . The background constant was derived from the decay correlations before the implantation. It is considered to be exact because the variation of the background within its uncertainties is below the sensitivity of the half-life fit. The result is shown in Figure 4.4(a). It yields a half-life of

$$T_{\beta,1/2} = (1.17 \pm 0.10) \text{ s} \quad (4.3)$$

It confirms the measurements of previous experiments ( $\rightarrow$  Tab. 4.3) and the statistical uncertainties are improved by a factor of 2. In a first consistency check, the half-life is derived by an event selection of decays showing coincidences with  $\gamma$ -emission which originates from the de-excitation of  $^{100}\text{In}$  ( $\rightarrow$  Fig. 4.22). This is possible for the first time with a reasonable amount of decay correlations and the exponential fit, considering a constant background ( $\rightarrow$  Fig. 4.4(b)), yields

$$T_{\beta,1/2}^{\gamma} = (1.30 \pm 0.22) \text{ s} \quad (4.4)$$

The uncertainties are larger compared to the previous result because the loss of statistics by requiring a coincident  $\gamma$ -transition which exceeds the gain by the improvement through the background reduction. However, both results are consistent within the  $1\sigma$ -confidence intervals.

The second check for consistency was performed by considering only the first decay

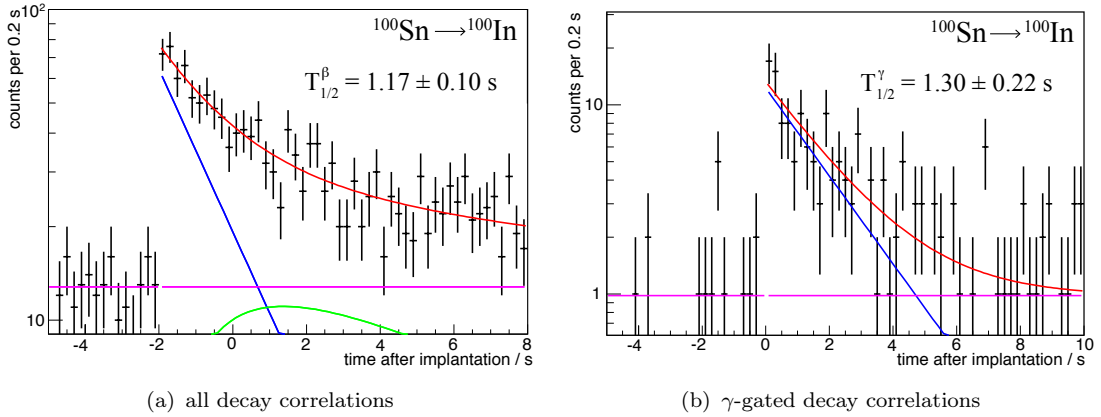


**Figure 4.4:** a) Half-life fit of  $^{100}\text{Sn}$  when it is accounted for all decay correlations within correlation windows  $t_{c,\text{imp}} = 15$  s and  $t_{c,\text{bgd}} = 10$  s for decay events and background, respectively. The spatial correlation window has a width of 1 pixel. b) Half-life fit applying a  $\gamma$ -gate on the transition energies  $E_{\gamma} = 96$  keV, 141 keV, 436 keV, 1297 keV and 2048 keV. The fit result, the parent component, the daughter component and the background component are represented by the red, blue, green and magenta curves, respectively.

correlation after an implantation instead of every correlation within a time window  $t_c$ . Then, the probability density is different from Equation (4.2). In this case, the detection probability of a decay within 1 pixel of 0.57 has to be taken into account. The probability density is constructed similar to a model of decay scenarios according to Schneider et al. [Sch+95]. In the cited work, the p.d.f was constructed on the basis of zero to three correlations within a time window while the number of correlations is one and the time window is given by the time of the implantation, here. The detailed construction is described in Appendix C. This analysis results in

$$T_{\beta,1/2}^{\text{first}} = 1.12_{-0.09}^{+0.25} \text{ s} \quad (4.5)$$

Again, the numbers are consistent. Nevertheless, the determination from the  $\gamma$ -gated event selection suggests that there might be a systematic uncertainty in the determination of the half-life by using a method without a  $\gamma$ -gate. A possible source for the difference of the values are the branching ratios of electron capture.

### Analysis of $^{96}\text{Cd}$

Already in 1971, a  $16^+$  high-spin isomer in  $^{96}\text{Cd}$  has been predicted by Peker et al. [Pek+71] which is expected at lower energies than the  $12^+$  and  $14^+$  states due to a strong influence of the isoscalar  $T=0$   $np$  interaction. Therefore, spin-gap isomerism occurs [Gra+06] since only an E6 transition to a  $10^+$ -state is possible, such that  $\beta$ - and

Reference	# Correlations	Half-life / s
Hinke et al. [Hin+12] [GSI]	159	$1.16 \pm 0.20$
Stolz [Sto02] [GSI]	8	$0.94_{-0.26}^{+0.54}$
Bazin et al. [Baz+08] [NSCL]	$\sim 40$	$0.55_{-0.31}^{+0.70}$

**Table 4.3:** Half-lives of  $^{100}\text{Sn}$  in literature.

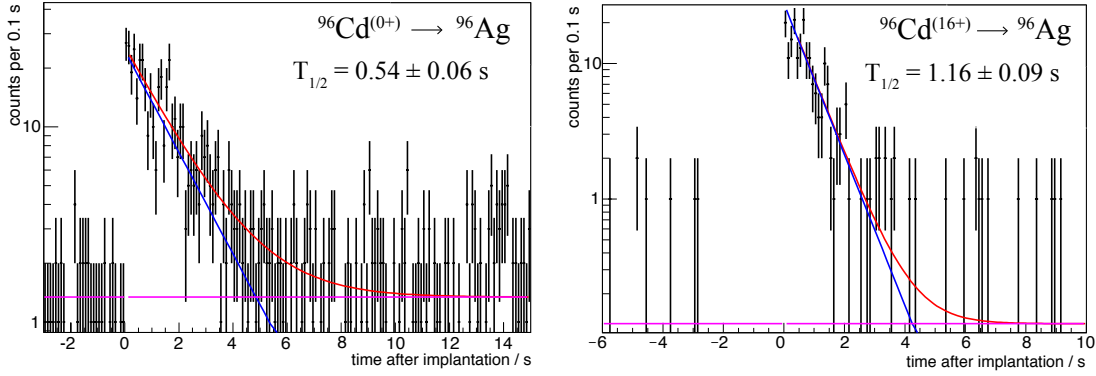


**Figure 4.6:** Time correlation plots of decay events with  $^{96}\text{Cd}$  implantations with a  $\gamma$ -gate on the transition to the  $2^+$  state with 421 keV to select the ground state transition (left) and a  $\gamma$ -gate on the cascading transitions of the  $16^+$  high-spin isomer with 667 keV, 1506 keV and 470 keV. The fit result, the parent component, and the background component are represented by the red, blue and magenta curves, respectively.

$\beta p$ -decay become competitive [Oga+83]. Evidence was obtained by Nara Singh. et al. [Nar+11] when cascading transitions from the  $15^+$ -isomer in  $^{96}\text{Ag}$  were observed in coincidence with the  $\beta$ -decay of  $^{96}\text{Cd}$  ( $\rightarrow$  Fig. 4.5). Thus,  $\beta$ -decay can proceed from the isomeric state or its ground state which is in the  $\pi\nu(g_{9/2}^{-2})$  configuration while the  $16^+$ -state has the configuration  $\pi\nu(p_{1/2}^2 g_{9/2}^{-3} g_{7/2}^1)$ .

The analysis of the isomeric states is described in detail in another thesis where the evidence for the transition  $15^+ \rightarrow 13^+$  in  $^{96}\text{Ag}$  is reported [Par16]. In the present work, events are selected by its  $\gamma$ -emission in order to extract the different decay components. At first, the half-life of the ground state of  $^{96}\text{Cd}$  is extracted which has a spin-parity assignment  $J^\pi = 0^+$  due to the even number of protons and neutrons. It decays into the  $1^+$  state of  $^{96}\text{Ag}$  which is followed by prompt  $\gamma$ -emission of 421 keV from the transition to the  $2^+$  isomeric state. In contrast the decay of the high-spin isomer is followed by delayed  $\gamma$ -emission with 470 keV, 667 keV and 1506 keV. Regarding the prompt and delayed  $\gamma$ -emission, further background reduction is achieved by requiring a time window 0 ns to 200 ns and 200 ns up to 8000 ns for the ground state decay and isomeric decay, respectively. As a proper  $\gamma$ -gated spectrum implies the absence of daughter components, the half-life was obtained by fitting an exponential model  $A_{\text{tot}}(\lambda, t) = A_{\text{par}}(\lambda, t) + b_{\text{const}}$  as was mentioned in the consistency check of  $^{100}\text{Sn}$  ( $\rightarrow$  Fig. 4.6).

$$T_{1/2}^{0^+} = (1.16 \pm 0.09) \text{ s} \quad T_{1/2}^{16^+} = (0.54 \pm 0.06) \text{ s} \quad (4.6)$$

This half-life of the ground state is much better in agreement with previously reported  $1.03_{-0.21}^{+0.24}$  s by Bazin et al. [Baz+08] than with  $0.67 \pm 0.15$  s by Nara Singh. et al. [Nar+11] which was determined from less than 20 events. The half-life of the high-spin state is also at variance with  $0.29_{-0.10}^{+0.11}$  s [Nar+11] but in agreement with the theoretical estimate of 0.5 s by Ogawa et al. [Oga+83]. Finally, consistency was checked considering  $\beta$ -delayed protons with a branching ratio of 5.5(40)% which was recently

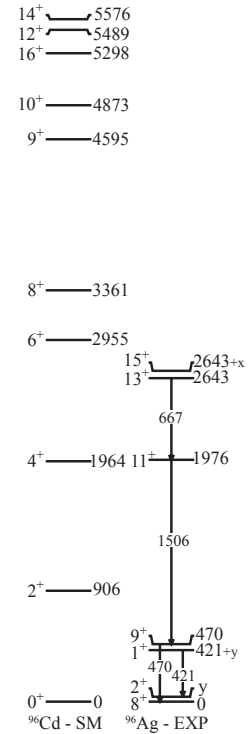


**Figure 4.5:** Calculated level scheme of  $^{96}\text{Cd}$  and experimental level scheme of  $^{96}\text{Ag}$  [Nar+11].

reported [Lor+12]. The protons are expected to originate from the daughter  $^{96}\text{Ag}$  in which two ground states are known, a  $2^+$ -state and an  $8^+$ -state with  $b_{\beta p} = 0.085$  as well as half-lives 4.40(6) s and 6.9(6) s, respectively [Bat+03]. The one-component exponential fit results in  $(5.0 \pm 0.3)$  s which is in good agreement with the weighted average of the literature values  $(5.1 \pm 0.6)$  s considering 65(20)% feeding to the  $8^+$ -state and 33(15)% feeding to the  $2^+$ -state [Bat+03].

### Analysis of $^{92}\text{Pd}$

$^{92}\text{Pd}$  is the last nucleus in a series of even-even  $N=Z$  nuclei with a sufficiently large number of implantations. The level scheme has been determined in a recent experiment at GANIL [Ced+02] where  $^{92}\text{Pd}$  was produced in a fusion-evaporation reaction, by bombarding an isotopically enriched  $^{58}\text{Ni}$  target with  $^{36}\text{Ar}$  ions. Cascading  $E2$ -transitions were measured and the comparison with theoretical calculations suggests that the isoscalar  $T=0$   $pn$ -interaction becomes dominant and the nucleus approaches the  $N=Z=50$  shell closure [Ced+02].

In contrast to  $^{96}\text{Cd}$ , isomeric states are not observed in this nucleus. Thus, the decay time distribution of  $^{92}\text{Pd}$  has been fitted by an exponential model similar to  $^{100}\text{Sn}$ . However, the decay daughter  $^{92}\text{Rh}$  has two decay branches, a fast component which decays with  $T_{1/2}^{(f)} = 0.53(37)$  s and a slow component which decays with  $T_{1/2}^{(s)} = 4.66(25)$  s. Both branches are considered by their corresponding contributions of 70% and 30%, respectively [Dea+04]. It yields

$$T_{1/2} = (1.25 \pm 0.03) \text{ s} \quad (4.7)$$

This is well-contained within the confidence interval of the value  $1.0_{-0.2}^{+0.3}$  s obtained by Faestermann et al. [Fae+02] and Kienle et al. [Kie+01] where the number of implantations was two orders of magnitude smaller. The improvement by a factor of 10 in precision, when the statistics is larger by a factor of  $\sim 100$ , is reasonable and gives a reference point on the requirements on future experiments with the aim to further narrow down the uncertainties of the observables in  $^{100}\text{Sn}$ .

### 4.1.4 Odd-Odd $N=Z$ Nuclei

The odd-odd nuclei along the  $N=Z$  line in the vicinity of  $^{100}\text{Sn}$  gain high interest as they show both, GT-transitions and Superallowed Fermi transitions. The latter occurs because all these nuclei have a low-lying  $I^\pi = 0^+$ ,  $T=1$ -state which decays into the isobaric analogue state of its  $N=Z+1$  neighbor. This results in high transition probabilities due to a large overlap of the initial and final wave functions. In this case,  $\gamma$ -emission of the daughter nucleus is not expected. This is  $T=1$ /state is particularly interesting because nucleons usually couple to the lowest isospin  $T=0$  in its ground state. The fact that a  $T=1$ -state is well below a  $T=0$ -state is attributed to the Wigner-energy. In contrast, the GT-transition proceeds from an isomeric state to excited states in its daughter nucleus. The de-excitation is observed through the correlated  $\gamma$ -emission of the daughter nucleus ( $\rightarrow$  Fig. 4.8(d)). The present analysis contributes with regard to a better understanding of the level and decay schemes of these nuclei which have not unambiguously derived yet.

### Analysis of $^{98}\text{In}$

Apart from the determination of the half-lives of different states, this experiment enabled the analysis of the  $Q_\beta$ -values of both, the Fermi-decay and GT-decay in  $^{98}\text{In}$ . The

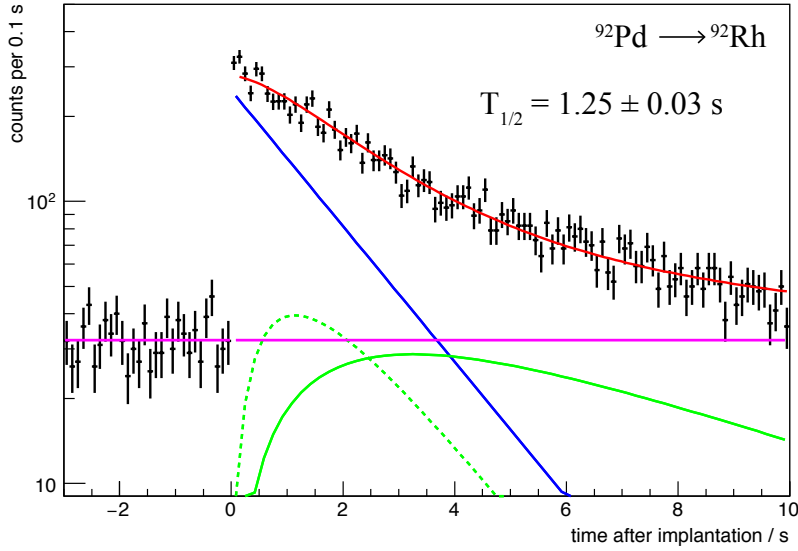


**Figure 4.7:** Determination of the half-life of  $^{92}\text{Pd}$ . The fit model consists of the exponential parent decay, two decay components of the daughter nucleus  $^{92}\text{Rh}$  and a constant background. The fit result, the parent component, the daughter component and the background component are represented by the red, blue, green and magenta curves, respectively. The dashed and solid green lines correspond to different decay channels of  $^{92}\text{Rh}$  by  $T_{1/2}^{(f)} = 0.53(37)$  s and  $T_{1/2}^{(s)} = 4.66(25)$  s, respectively.

former is determined by using the CVC hypothesis that all Superallowed Fermi decays have the same  $\mathcal{F}t = 3072.27 \pm 0.72$  [HT15] while the latter is determined by the analysis of the  $\beta p$ -decay into  $^{97}\text{Ag}$ .

The half-lives are determined by using the MLH-method as explained in Section 3.1. The timing-correlation of implantation and decay events clearly shows two exponential components, a fast and a slow one ( $\rightarrow$  Fig. 4.9).

Therefore, the correlated  $\gamma$ -emission was studied in the range of 0 ms to 200 ms and 0.2 s to 4.0 s where the fast component does not influence the spectrum for times  $t > 200$  ms  $\approx 7 \cdot T_{1/2}^{0+}$ . There is no correlated  $\beta$ -delayed  $\gamma$ -emission ( $\rightarrow$  Fig. 4.8(c)) which corresponds to the short time range ( $\rightarrow$  Fig. 4.8(a)) such that this component is attributed to the Fermi-decay. In contrast, the event selection corresponding to the slow component ( $\rightarrow$  Fig. 4.8(b)) shows coincident  $\gamma$ -emission from  $^{98}\text{Cd}$  ( $\rightarrow$  Fig. 4.8(d)) which is attributed to the Gamow-Teller decay.

The fit model for the combined fit employs two parent components, its daughters and a constant background. Further components are not considered due to the correlation time window  $t_c \ll T_{1/2, \text{granddaughter}}$

$$A_{\text{tot}}(\lambda_1, \lambda_2, t) = A_{\text{par},s}(\lambda_s, t) + A_{\text{par},f}(\lambda_f, t) + A_{\text{dau},s}(\lambda_s, \lambda_d, t) + A_{\text{dau},f}(\lambda_f, \lambda_d, t) + b_{\text{const}} \quad (4.8)$$

This yields

$$T_{1/2}^{\text{T}=1} = (29 \pm 1) \text{ ms} \quad T_{1/2}^{\text{T}=0} = (0.86 \pm 0.04) \text{ s} \quad (4.9)$$

The Gamow-Teller decay is isolated by a gate on the  $\gamma$ -transitions at 147 keV, 198 keV, 687 keV and 1395 keV in  $^{98}\text{Cd}$ . The half-life is derived by using an exponential model with a constant background resulting in

$$T_{1/2}^{\gamma, \text{T}=0} = (0.88 \pm 0.07) \text{ s} \quad (4.10)$$

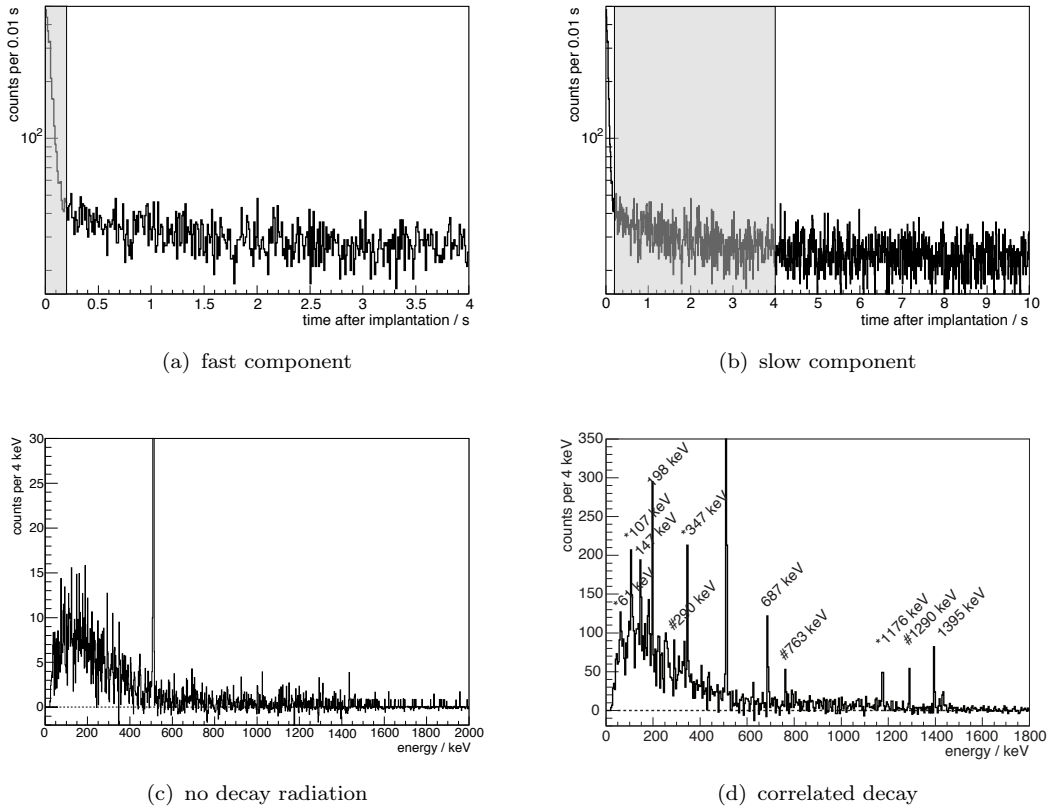


**Figure 4.8:** a) Time distribution of decay correlations of  $^{98}\text{In}$  with an event selection by a time window (gray area) from 0 s to 0.2 s. b) Time distribution of decay correlations of  $^{98}\text{In}$  with an event selection by a time window from 0.2 s to 4 s (gray area). c) Background corrected correlated  $\gamma$ -emission according to the timing gate in Figure a). d) Background corrected correlated  $\gamma$ -emission according to the timing gate in Figure b).

The correlated  $\gamma$ -emission of decay events of  $^{98}\text{In}$ , which are labeled by hashed numbers in Figure 4.8(d), agrees with the transitions known for  $^{97}\text{Ag}$  [Lip+05] rather than  $^{98}\text{Cd}$ . This indicates the  $\beta p$ -decay channel which is confirmed by requiring the energy deposition in the strips of the Si-detectors to be above 1.5 MeV in both directions ( $\rightarrow$  Fig. 4.10(c)). This gate identifies proton emission because only the  $\gamma$ -emission remains which is associated with the de-excitation of  $^{97}\text{Ag}$ . Certainly, this suggests that the  $\beta$ -decay proceeds into high-lying states in  $^{98}\text{Cd}$ , well above the proton separation energy. The half-life measurement allows to infer whether it proceeds from the same  $T=0$ -state as the Gamow-Teller  $\beta$ -decay mentioned above or from another state in  $^{98}\text{In}$ . The fit is performed by using the same exponential model as in the case of the  $\gamma$ -gated selection yielding

$$T_{1/2}^p = (0.87 \pm 0.06) \text{ s} \quad (4.11)$$

This agrees with the previous values of the slow component. In conclusion, the  $\beta p$ -branch also proceeds from the same isomeric  $T=0$ -state of  $^{98}\text{In}$  ( $\rightarrow$  Fig. 4.10(b)). Both decay components are in good agreement with the half-lives determined in previous experiments [Str10; Lor+12; Kie96; Baz+08] which are listed in Table 4.4. The analysis by Straub [Str10] resulted in 32(6) ms and 0.86(21) s, respectively, who has obtained the most precise results until this experiment. The uncertainties of the half-lives are improved by more than a factor of 3 by the present analysis. Furthermore, Lorusso

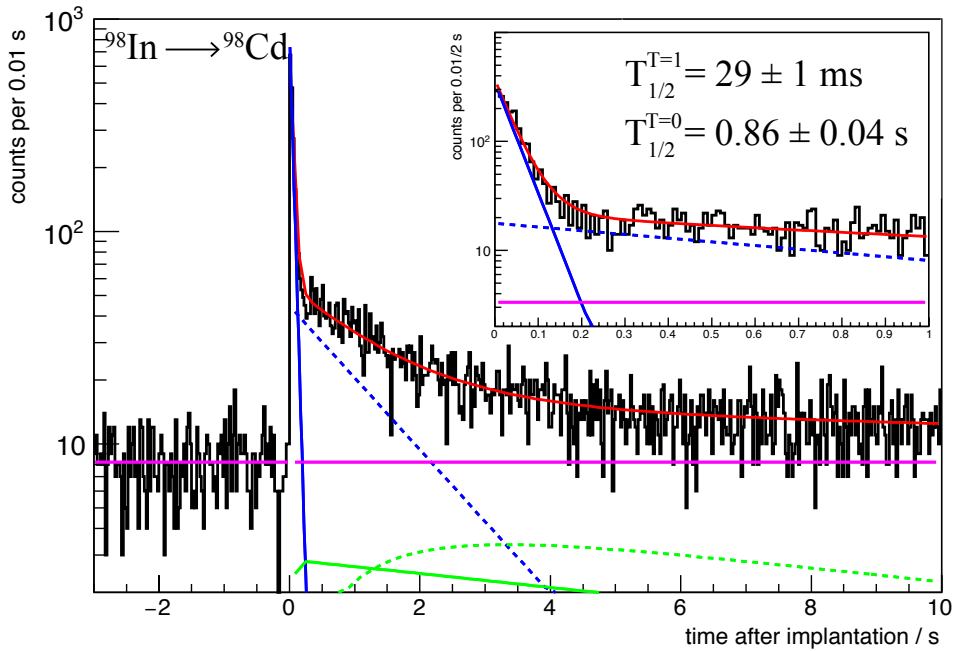


**Figure 4.9:** Determination of the half-lives in  $^{98}\text{In}$ . Combined fit of the fast and slow components. The fit result, the parent component, the daughter component and the background component are represented by the red, blue, green and magenta curves, respectively. The solid blue and green lines are associated with the fast component while the corresponding dashed lines belong to the slow component. Half-life fits for the  $\gamma$ -gated event selection as well as for the event selection by  $\beta$ -delayed protons are shown in the Appendix ( $\rightarrow$  Fig. D.1).

et al. [Lor+12] has reported two decay components in the  $\beta p$ -branch, too, in analogy to the non gamma-gated decay spectrum. However, they suggested a fast  $\beta p$ -component from the ground state of  $^{98}\text{In}$  in the half-life fit to their own surprise. Certainly, the time spectrum of decay correlations which are attributed to a  $\beta p$ -event do not show two components ( $\rightarrow$  App. D Fig. D.1).

### The $Q_{\text{EC}}$ -Value of $^{98}\text{In}$

Compared to its  $N=Z$  neighbor  $^{100}\text{Sn}$ , the  $\beta$ -decay of  $^{98}\text{In}$  proceeds by both, Fermi- and GT-transitions. In this case, the transition strength cannot be derived from the  $\log(ft)$ -value if the branching ratio is not well known. Furthermore, the Fermi-decay component cannot be separated by a  $\gamma$ -gate because it proceeds from ground state to ground state. Therefore, the corresponding  $Q$ -values are determined by using the CVC and the  $\beta p$ -decay of the isomeric  $T=0$  state. This allows to derive the splitting of the  $T=0$  and  $T=1$  states of  $^{98}\text{In}$ .

The  $Q_{\text{EC}}^{T=1}$  of the ground state is calculated using the LOGFT-calculator [Nat16b] and the half-life  $T_{1/2}^{T=1} = (29 \pm 1)$  ms by taking  $\mathcal{F}t = 3072.27 \pm 0.72$  [HT15] resulting in  $Q_{\text{EC}}^{T=1} = (12.5 \pm 0.1)$  MeV.

In contrast, the determination of the  $Q_{\beta}$ -value of the isomeric  $T=0$  state needs a more careful analysis. At first, the energy level of this state is derived which results from considering the  $\beta p$ -decay channel into  $^{97}\text{Ag}$  ( $\rightarrow$  Fig. 4.10(b), schematically  $\rightarrow$  Fig. 1.7). It is determined by adding up four contributions: 1) the proton separation energy  $S_p$  of  $^{98}\text{Cd}$ , 2) the excitation energy  $E(\frac{21}{2}^+)$  of the  $\frac{21}{2}^+$ -state in  $^{97}\text{Ag}$ , 3) the  $Q_p$ -value of

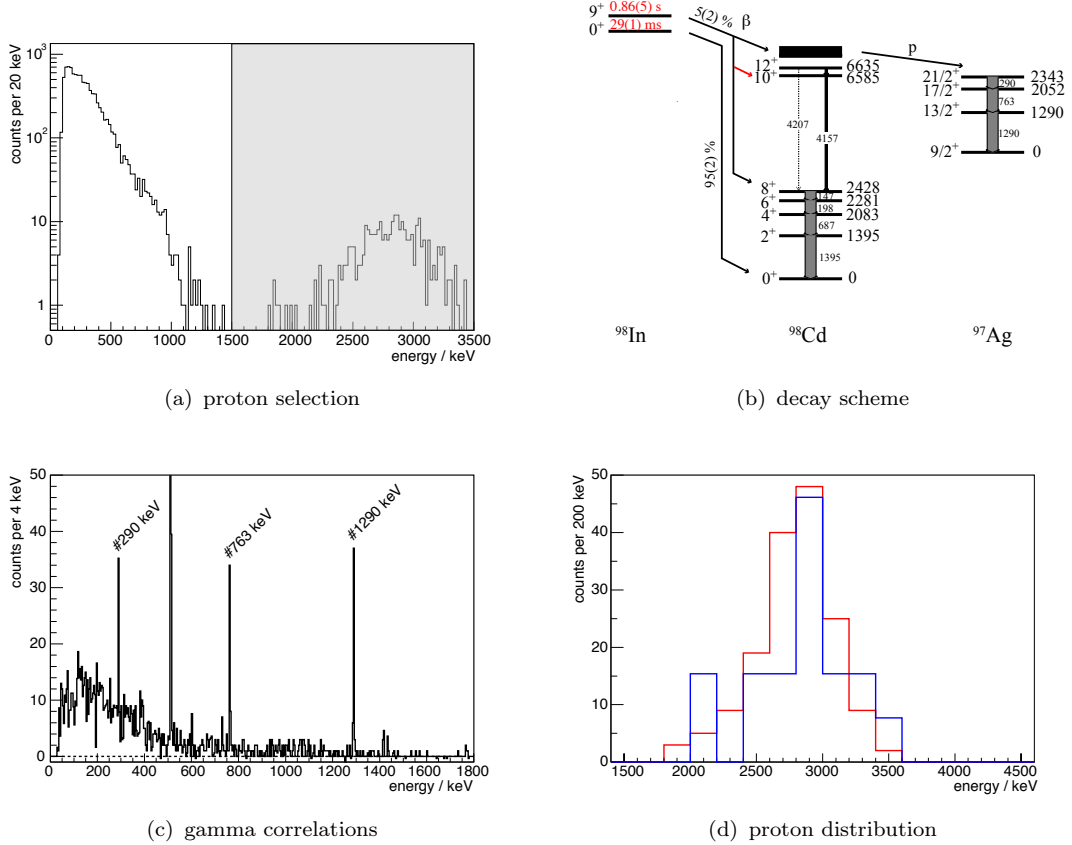


**Figure 4.10:** a) Distribution of single pixel energies. b) Decay scheme of  $^{98}\text{In}$  with the ground state transition and fragmented transition strength from the isomeric state. The red arrow labels that the evidence for the  $9^+ \rightarrow 10^+$  transition was found by one coincidence of emission with energies of 147 keV, 198 keV and 4157 keV. The  $\beta p$ -branch proceeds via the core-excited states in  $^{98}\text{Cd}$ . c) Correlated  $\gamma$ -emission according to the energy gate of Figure a) d) Comparison of all  $\beta$ -delayed protons (red) with those obtained by requiring emission of the 511 keV in the HPGe-detector.

$^{98}\text{Cd}$  and 4) the  $Q_{\beta}$ -value of  $^{98}\text{In}$ . 1)  $S_p = 4.10 \pm 0.13$  MeV is determined by the mass difference taken from the mass evaluation [WAW+12] and 2)  $E(\frac{21}{2}^+) = 2343$  keV from the level scheme of  $^{97}\text{Ag}$  [Lip+05]. 3) is taken from this experiment by the measurement of the energy loss  $\Delta E_p$  of protons within the Si-detectors ( $\rightarrow$  Fig. 4.10(d)) where  $Q_p$  is given by the upper limit of the proton spectrum  $3.5 \pm 0.1$  MeV. The value is accompanied by a systematic uncertainty of the mean energy loss of electrons in single strips from the  $\beta$ -decay. Eventually, the  $Q_{\text{EC}}^{9^+}$ -value for the  $\beta$ -decay of the  $\beta p$ -branch into high-lying states is determined by the ratio of the intensities  $\mathcal{I}$  of the  $\beta^+$ -channel and the sum of all channels:  $I_{\beta^+}/I_{\text{tot};\beta^+,\text{EC}}$  [FGG13]. The latter ratio has been determined by considering the number of  $\beta$ -delayed protons with a  $\gamma$ -gate on the emission of 511 keV and without a  $\gamma$ -gate ( $\rightarrow$  Fig. 4.10(d)). The efficiency corrected ratio is  $\frac{131 \pm 10}{160}$  resulting in  $Q_{\text{EC}}^{\beta p} = (3.9 \pm 0.5)$  MeV with statistical uncertainties which are introduced by the efficiency correction. The summation of these components results in  $E^{T=0} \geq (13.8 \pm 1.0)$  MeV concluding that the  $0^+$ -state lies below the  $9^+$ -state

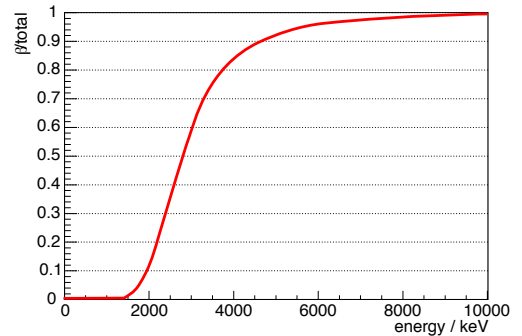


**Figure 4.11:**  $Q_{\text{EC}}$ -dependence of the ratio of the  $\beta$ -intensities  $I_{\beta}$  to total intensities  $I_{\text{tot}}$  of  $^{98}\text{In}$  calculated with the LOGFT-calculator [Nat16b].

Reference	Fermi / ms	Gamow-Teller / s
Kienle [Kie96]	$32_{-11}^{+32}$	$1.2_{-0.4}^{+1.2}$
Lorusso et al. [Lor+12]	$47(13)^{(\beta)}$	$1.27(30)^{(\beta)}$
Lorusso et al. [Lor+12]	$135(65)^{(\beta p)}$	$1.27(30)^{(\beta p)}$
Bazin et al. [Baz+08]	$47 \pm 13$	$0.66 \pm 0.40$
Straub, Hinke, et al. [SH+10]	$32 \pm 6$	$0.86 \pm 0.21$

**Table 4.4:** Half-lives of  $^{98}\text{In}$  in literature.  $(\beta)$  and  $(\beta p)$  labels the results of the half-life fits with an event selection of all  $\beta$ -correlations and  $\beta$ -delayed protons by Lorusso et al. [Lor+12], respectively.

$E_{T=1} < E_{T=0}$  separated by  $1.3(10)(-5)$  MeV. Thus, the  $Q_\beta$ -value for the transition from the  $T=1$  state to the  $8^+$  in  $^{98}\text{In}$  is given by  $(11.4 \pm 1.0)$  MeV. In coherence with this analysis, the  $\beta$ -decay of  $^{98}\text{In}$  to the  $10^+$  core-excited state was observed in the  $\gamma$ - $\gamma$  coincidence analysis ( $\rightarrow$  App. D, Fig. D.2). This is another strong indication that the isomeric state of  $^{98}\text{In}$  is associated with a spin-parity of  $9^+$  and the isospin  $T=0$ .

### Analysis of $^{94}\text{Ag}$ and $^{90}\text{Rh}$

The  $N=Z=47, 46$  nuclei with three and four holes in the  $\pi\nu g_{9/2}$ -orbitals have the same characteristics in their decay curves as  $^{98}\text{In}$  ( $\rightarrow$  Fig. 4.13) and the same method for analysis is used. Concerning the fast and slow component, a fit applying two independent exponentials, the corresponding daughters and a constant background was employed. Furthermore,  $^{94}\text{Ag}$  is very interesting as direct<sup>2</sup> one-proton (1p) and two-proton (2p) emission has been reported by Mukha et al. [Muk+06a] and questioned by Pechenaya et al. [Pec+07] later. The result was very surprising because 2p-radioactivity is only predicted for even- $Z$  nuclei by Mukha et al. [Muk+06a] and Pechenaya et al. [Pec+07] has put tight constraints to the validity of this scenario by  $Q$ -value arguments and a detailed analysis of the  $\gamma$ -transitions in  $^{92}\text{Rh}$ , where  $\gamma$ -lines occurring at  $E_\gamma = 565$  keV and 833 keV, have not been observed. Strong deformation of  $^{94}\text{Ag}$  which was required for the scenario described by the experimental results of Mukha et al. [Muk+06a] is at variance with shell model calculations by Ragnarsson and Carlsson [RC06].

$^{94}\text{Ag}$  is a nucleus with two known isomeric states with a spin-parity assignments  $7^+$  and  $21^+$  [La +02; Muk+04] ( $\rightarrow$  Fig. 4.12). In order to derive the half-lives, the same model as for  $^{98}\text{In}$  is used ( $\rightarrow$  Eqn. (4.8)) since the difference of the mean of half-lives of the isomeric states  $0.55(6)$  s and  $0.40(4)$  s which are known in literature [Nat16a; Muk+05; Ple+04; La +02; Ple+94], respectively, is statistically not significant. The  $\gamma$ -spectroscopy of  $^{94}\text{Ag}$  also reveals that the  $21^+$ -isomeric state is populated with a very small branching ratio such that the slow component of the time spectrum is attributed to the  $7^+$ -state. The fit resultS

$$T_{1/2}^{0+} = (28 \pm 2) \text{ ms} \quad T_{1/2}^{7+} = (0.51 \pm 0.02) \text{ s} \quad (4.12)$$

The more precise half-life from this analysis for the GT-transition agrees with the literature value of the  $7^+$  isomeric state. Here, The value of the slow component is also checked for consistency with the results by applying a  $\gamma$ -gate to those  $\gamma$ -transitions which occur

<sup>2</sup>Radioactivity that does not result in prompt nuclear reactions or following  $\beta$ -decay.

subsequent to a GT-transition of  $^{94}\text{Ag}$  in  $^{94}\text{Pd}$  ( $E_\gamma = 324.0$  keV, 659.1 keV, 813.8 keV, 905.3 keV). It results

$$T_{1/2}^{\gamma,7^+} = (0.49 \pm 0.02) \text{ s} \quad (4.13)$$

and the same fit to the beta-ion correlation time spectrum obtained from  $\beta p$ -events yields

$$T_{1/2}^{\beta p} = (0.44 \pm 0.05) \text{ s} \quad (4.14)$$

Both values are consistent with the slow component. The plots corresponding to this fits are attached in Appendix D ( $\rightarrow$  Fig. D.1)

The half-life analysis of odd-odd  $N = Z$ -nuclei is concluded by considering the decay curve of  $^{90}\text{Rh}$  which also show a fast and slow component with the same characteristics. A detailed analysis of this nucleus was performed for the first time and the half-life result in

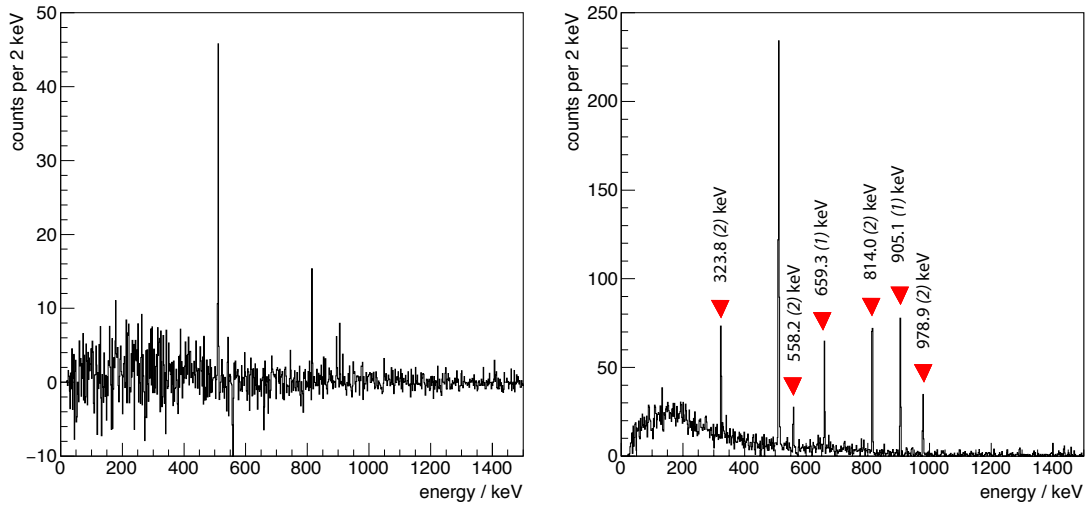
$$T_{1/2}^{0^+} = (27 \pm 1) \text{ ms} \quad (4.15)$$

$$T_{1/2}^{5^+} = (0.50 \pm 0.03) \text{ s} \quad (4.16)$$

$$T_{1/2}^{\gamma,5^+} = (0.58 \pm 0.06) \text{ s} \quad (4.17)$$

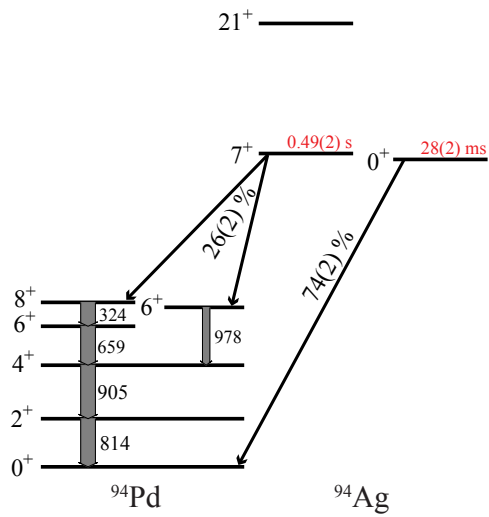
$$T_{1/2}^{\beta p} = (0.49 \pm 0.10) \text{ s} \quad (4.18)$$

The statistics were sufficiently high that in this case the consistency check by a  $\gamma$ -gated and  $\beta p$ -gated selection was also performed. The results of the combined fit are shown in Figure 4.13(b). The plots of the  $\gamma$ - and  $\beta p$ -gated event selection are attached to Appendix D ( $\rightarrow$  Fig. D.1). The results are very similar to what is obtained in case of  $^{94}\text{Ag}$  which concludes that the change of the matrix element by the removal of two  $pn$ -pairs is very small. Furthermore, the level scheme of  $^{90}\text{Rh}$  has not been studied in detail yet as no precise information was found in the standard database of nuclear physics [Nat16a] and literature. In this work, the  $\gamma$ -spectroscopy as well as the decay curve suggest the existence of an isomeric state in  $^{90}\text{Rh}$ .  $\beta$ -spectroscopy allows to conclude the spin-parity of the isomeric state. Regarding the conclusion, the level scheme of the daughter nucleus  $^{90}\text{Ru}$  was studied ( $\rightarrow$  Fig. 4.12(d)). It was derived by Heese et al. [Hee+94] in a fusion-evaporation experiment who has assigned the level ordering according to the intensities which were measured with the Ge-detector array OSIRIS. Here,  $\gamma$ -emission lines are correlated with the  $\beta$ -decay of  $^{90}\text{Rh}$ . Two emission lines at 1163 keV and 1363 keV attract attention since they have not been reported yet while three known dominant transitions with energies of 738 keV, 886 keV and 900 keV are also observed. The coincidence analysis ( $\rightarrow$  App. D Fig. D.2) shows that the latter ones belong to the same cascade. The absolute intensities suggest that the transitions with 738 keV and 900 keV are associated with the lowest energy levels since they have the highest intensities and 886 keV as well as 1163 keV have similar but lower intensities. The  $\gamma$ -emission with 946 keV as known from literature, was not observed and the analysis of the broadening of a the 511-keV line does not enable the confirmation of the transition from the  $8^+$ -state with 512 keV. If the level scheme would be true, a similar number of events at 512 keV and 946 keV would be expected. Therefore, the transition with 886 keV was moved to above the 900 keV transition and is associated with the  $6^+ \rightarrow 4^+$  transition in  $^{90}\text{Ru}$ . Another transition which is unknown was observed at 1316 keV. The analysis of a decay window from 0 s to 1.0 s as well as 1.0 s to 3.0 s reveals similar intensities (3 counts) of this transition in both time windows. Considering a half-life of 0.50(3) s, this emission would not

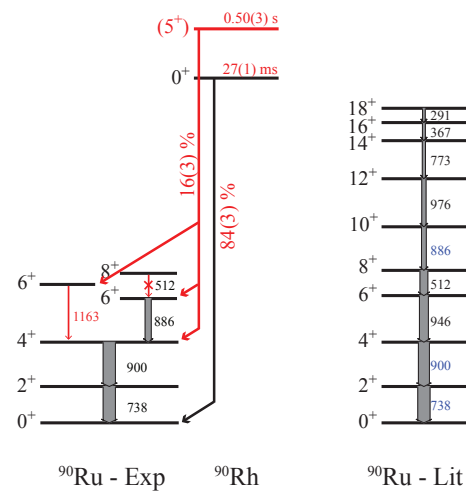


(a)  $^{94}\text{Ag}$  -  $t_c$ : 0 s to 0.2 s

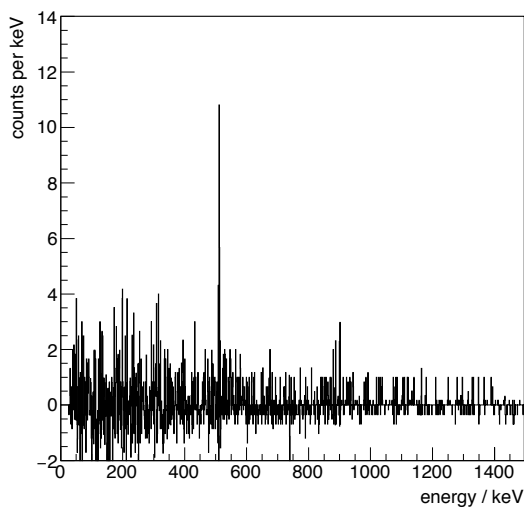
(b)  $^{94}\text{Ag}$  -  $t_c$ : 0.2 s to 2.7 s



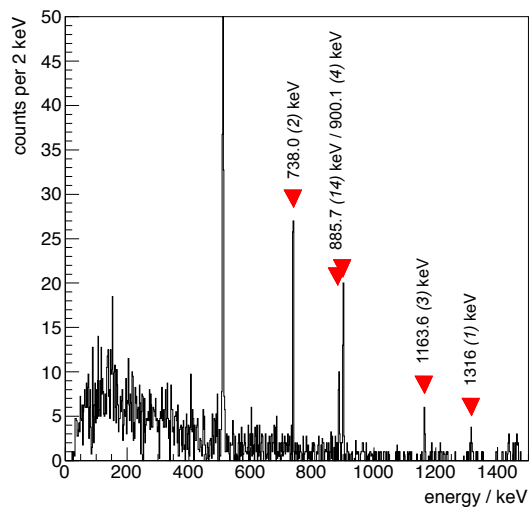
(c)  $^{94}\text{Ag}$  - decay scheme



(d)  $^{90}\text{Rh}$  - decay scheme

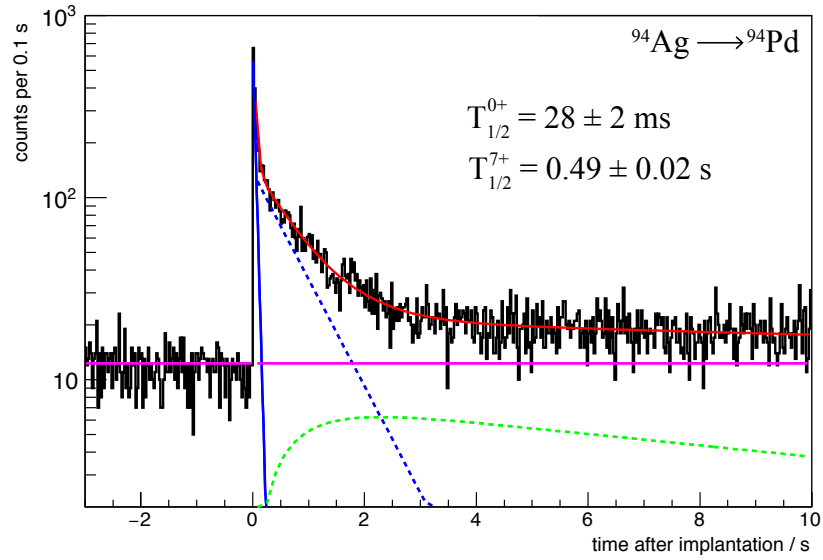
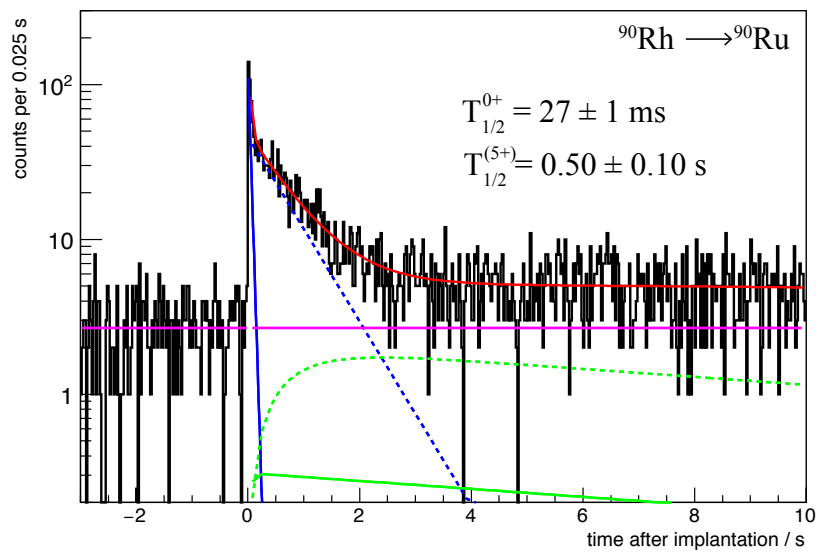


(e)  $^{90}\text{Rh}$  -  $t_c$ : 0 s to 0.2 s



(f)  $^{90}\text{Rh}$  -  $t_c$ : 0.2 s to 2.7 s

**Figure 4.12:**  $\gamma$ -spectroscopy of  $^{94}\text{Ag}$  (upper row) and  $^{90}\text{Rh}$  (lower row). The left panels are background corrected  $\gamma$ -spectra correlated with the short decay component while the right panels show the correlated  $\gamma$ -emission of the slow component. In case of  $^{90}\text{Rh}$ , the spin-parity of the isomeric state is assigned tentatively to be  $5^+$  for the first time.

(a)  $\beta$ -decay of  $^{94}\text{Ag}$ (b)  $\beta$ -decay of  $^{90}\text{Rh}$ 

**Figure 4.13:** Determination of half-lives in  $^{94}\text{Ag}$  and  $^{90}\text{Rh}$  where the shape corresponds to the odd-odd  $N=Z$   $^{98}\text{In}$ . The solid blue and green lines are associated with the fast component while the corresponding dashed lines belong to the slow component. Half-life fits for the  $\gamma$ -gated event selection as well as for the event selection by  $\beta$ -delayed are shown in the Appendix ( $\rightarrow$  Fig. D.1).

be expected in the later time window. However, the analysis of the background shows no transitions with this energy. Hence, this emission is expected to be associated with a daughter decay. The same analysis was performed with the emission line at 1163 keV which vanished after 1.0 s such that this transition is assigned to the level scheme of  $^{90}\text{Rh}$ . With regard to the selection rules of the  $\beta$ -decay and the intensity which is similar to the transition with 886 keV, this emission is tentatively assigned to originate from a second  $6^+$ -state ( $\rightarrow$  Fig. 4.12(d)).

All things considered, there is certainly a branch in the  $\beta$ -decay of  $^{90}\text{Rh}$  which decays into the  $4^+$ -state of  $^{90}\text{Ru}$ . Assuming a Gamow-Teller transition, the selection rules allow for a  $4^+$ ,  $5^+$  and  $6^+$ . Thus, by the analogy of the heavier even-even  $N=Z$  nuclei  $^{94}\text{Ag}$  and  $^{98}\text{In}$ , the spin-parity  $5^+$  is tentatively assigned to  $^{90}\text{Rh}$  which would be generated by the  $pn$ -coupling of a  $g_{9/2}$ -proton with a  $g_{9/2}$ -neutron with  $J_{\pi,\nu} = \pm 5/2$  while the remaining nucleons couple to zero with spins  $\pm 9/2$  and  $\pm 7/2$ , correspondingly.

So far only  $\beta$ -delayed  $\gamma$ -emission,  $\beta^-$ ,  $\beta p$ -decay were discussed. The discussion of the 1p- and 2p-radioactivity in  $^{94}\text{Ag}$  was also targeted in the present analysis ( $\rightarrow$  Fig. 4.15) which is controversially discussed as mentioned above. At first, the probability to find a 2p-decay in the present experiment is considered with a branching ratio of 0.5% and proceeding from the  $21^+$  isomeric state of  $^{94}\text{Ag}$  to the  $11^+$ -state as reported by Mukha et al. [Muk+06a]. The fraction of nuclei which proceed by the 1p-decay was reported to 4.1% by the same authors. The transitions occur at sharply defined energies and they were mentioned to be observed in peaks at 0.8 MeV and 1.0 MeV (1p) as well as 1.8 MeV (2p). Considering the correction for the detector recovery time of about 4.3% and that no more than 1% of the decays proceeds from the  $21^+$  state, 1 count is expected to originate from a 2p-transition on maximum where a sample size of 17000 implantations is considered. The correlated  $\gamma$ -emission cannot be used to confirm such a transition because the summed  $\gamma$ -efficiency of transitions which occur in  $^{92}\text{Rh}$  is around

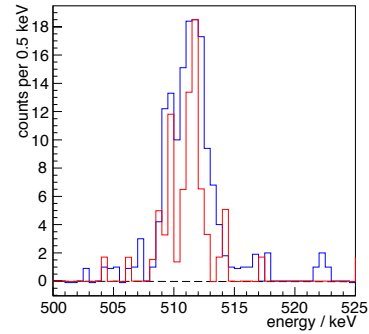


**Figure 4.14:** Comparison of the  $\gamma$ -emission of the fast and slow component. The  $\gamma$ -spectrum of the fast component has only emission at 511 keV as expected for a Fermi decay. This component is normalized according to the time windows 0-0.1 s (fast component) and 1.0-3.0 s (slow component) and their branching ratios. No broadening due to a 512 keV transition is visible.

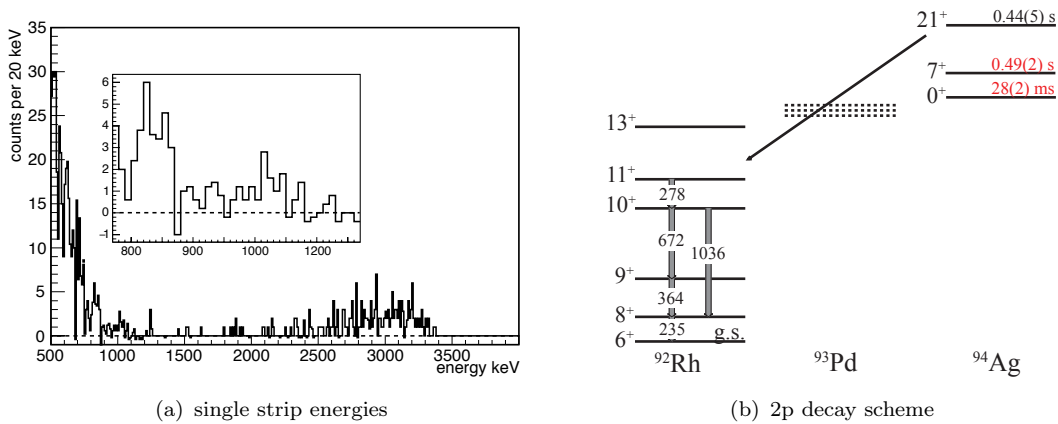


**Figure 4.15:** a) Energy deposit in Si-detectors regarding the search for the 1p- and 2p-emission in  $^{94}\text{Ag}$ . b) Decay scheme for 2p-emission from  $^{94}\text{Ag}$  decaying into  $^{92}\text{Rh}$ .

Si-energy / keV	t / s	$E_\gamma$ / keV	decay channel
1849	0.67	274,349,740	$\beta p$
1869	5.00	683,1270	—
1911	1.91	269,763	—
1969	0.21	79, 91, 184	—

**Table 4.5:** Gamma-energies correlated with the characteristic energy deposit in Si-detectors which are assigned candidates of 2p-decay in  $^{94}\text{Ag}$ .

10%. Nevertheless, an event-by-event analysis of the correlated  $\gamma$ -emission of decays with  $\Delta E \sim E_{2p}$  was performed. The results are listed in Table 4.5 where only one candidate is associated with  $\beta p$ -decay.

Likewise, in the case of the 1p-radioactivity  $7 \pm 1$  cts are expected in total by two possible channels of 1p transitions. In the spectrum of single pixel energies of the Si-detectors ( $\rightarrow$  Fig. 4.15(a)) of decay events, which correlate with  $^{94}\text{Ag}$ , two peak-like structures are present at the energies of  $\sim 0.8$  MeV and  $\sim 1.0$  MeV. However, they cannot be significantly distinguished from the fluctuations which are introduced by the background correction.

### 4.1.5 Determination of the $\beta p$ -Branching Ratios

The  $\beta p$ -channel is an important ingredient regarding the exact calculation of the isotopic abundances as generated in the rp-process. Furthermore, the decay scheme can be concluded as only states above the proton separation energy are allowed such that the  $\beta p$ -channel can proceed. The protons are stopped within a very small range which does usually not exceed more than one pixel and they are discriminated as described in Section 3.2.2. The correlation time window was chosen from 0.2 s to 5 s after the corresponding implantations according to the half-life of the parent nucleus. The background of these decay correlations is generated by the decay of less exotic nuclei with weaker  $\beta p$ -branches so that only a few background events contribute to the energy spectrum. In Figure 4.16, the correlated  $\beta p$ -spectra of  $^{98}\text{In}$  are shown. The difference between the blue and the red histogram is the lower energy cut of 0 keV and 1500 keV contained within a single pixel, respectively. In this case, every energy deposition of each detector strip is booked into the histogram separately. The high energy part of the spectrum remains almost unaffected by this cut as random coincidences with proton background events are rare (black spectrum). In the determination of the  $\beta p$ -branching

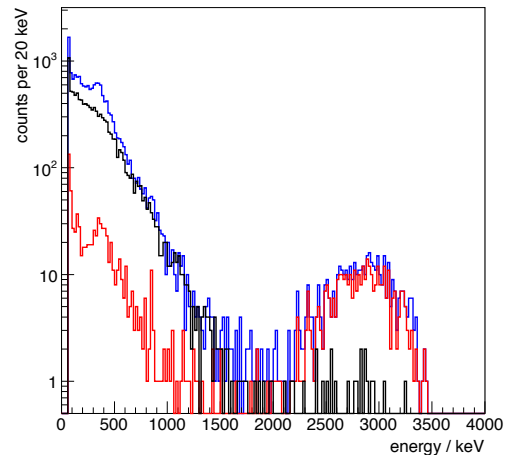


**Figure 4.16:** Spectra of single Si-strip energies for decay events correlated with the implantations of  $^{98}\text{In}$  within 10 s before (black) and 3 s after (blue, red) the corresponding implantation. The blue and red spectra are generated by requiring the occurrence of an energy deposit of  $E > 0$  keV and  $E > 1500$  keV in a single strip in both directions, X and Y, respectively.

ratios, the background spectrum was derived from the implantation history. Additionally, contributions from  $\beta p$ -decays of the daughter nucleus were considered. For instance,  $^{100}\text{In}$  has a strong  $\beta p$ -branch that all  $\beta$ -delayed protons which are correlated with  $^{100}\text{Sn}$  are expected to originate from the daughter decay. Considering the sample of decay correlations within 1 pixel corresponding to 846 implantations in the DSSD detectors,  $7 \pm 3$   $\beta$ -delayed proton-events are expected from  $^{100}\text{In}$  which is consistent with the observation of 10 events correlating with  $^{100}\text{Sn}$ . Except for  $^{96}\text{Cd}$ , the contribution of  $\beta p$ -decays from the daughter is negligible for the other  $N = Z$  nuclei. Besides  $N = Z$  nuclei, the  $\beta p$ -branching ratio of  $N = Z - 1$  nuclei was determined by using a correlation time window of  $t_c = 0.2$  s. This is sufficiently short so that the contribution of the daughter decay is negligible in the energy spectrum of  $\beta p$ -events since the half-life ( $\sim 1$  s) of the states in daughter nucleus which can decay via the  $\beta p$ -channel are long compared to the parent nucleus. Then, the  $\beta p$ -ratio was calculated by the ratio of the background corrected number of  $\beta p$ -events  $N_p$  in the energy window and the number of implantations which is accepted by the spatial and time selection  $N_{\text{tot}}$ . The results of the  $\beta p$ -branching ratios are summarized in Table 5.1 ( $\rightarrow$  Cpt. 5).

## 4.2 The Level Scheme of $^{100}\text{In}$

The level scheme of  $^{100}\text{In}$  is studied by  $\beta$ -delayed  $\gamma$ -spectroscopy in the GT-transition  $^{100}\text{Sn} \rightarrow ^{100}\text{In}$  which is explained in the introduction. It was proposed by the analysis of Hinke et al. [Hin+12] where only a very small number of correlated events was available. Therefore, the level scheme has not been derived without ambiguities and  $\gamma$ - $\gamma$  coincidences were not feasible due to a small number of implantations.

In order to study the ordering of the energy levels, calculations were performed by Grawe [Hin10], Coraggio et al. [Cor+04] as well as Stone and Walter [SW85] who proposed different scenarios which are shown in Figures 4.17 a)-c), respectively. Stone and Walter [SW85] have proposed a single decay cascade ( $\rightarrow$  Fig. 4.17(a)) which requires a strong change in the  $pn$ -interaction of the  $\pi g_{9/2} \nu g_{7/2}$ -orbitals. It was ruled out by the argument that neighboring nuclei  $^{102}\text{Sn}$  and  $^{98}\text{Cd}$  are in good agreement with this interaction [Hin+12; Lip+98; Bal+10]. Regarding the mass difference between  $^{100}\text{Sn}$  and  $^{100}\text{In}$  which is measured to  $\Delta M = 6.9 \pm 1.0$  MeV [Cha+96] and predicted to  $\Delta M = 7.03$  MeV [WAW+12], this scenario becomes unlikely as the  $Q_{\text{EC}}^a$ -value is far above this result ( $\rightarrow$  Sec. 4.4.1).

The other scenarios propose a branching of the first  $1^+$ -state into two branches with energies of 2048 keV and 1297 keV which decay into different  $2^+$ -states. In order to confirm either of these scenarios, the unique transitions, which are proposed accordingly, has to be identified. The transitions from the lowest energy levels to the ground state (labeled with x and y in the schematic) are expected to be highly converted. Therefore, rather the conversion electrons are observed with the Si-detectors than the  $\gamma$ -emission with the HPGe-detectors. However, the search for conversion electrons concerning scenarios b and c is challenging because the noise level of the Si-detectors  $E_{\text{noise}} \sim 50$  keV is in the order of the expected energies of  $E < 70$  keV while the energy resolution is  $\sim 40$  keV. This transition attracts high attention since it is the missing link to explain the level scheme by a cascade of  $M1$ -transitions from the  $1^+$  excited state to the  $6^+$  ground state. In general, gamma-transitions in  $^{100}\text{In}$  are investigated by  $\beta$ -delayed  $\gamma$ -radiation which

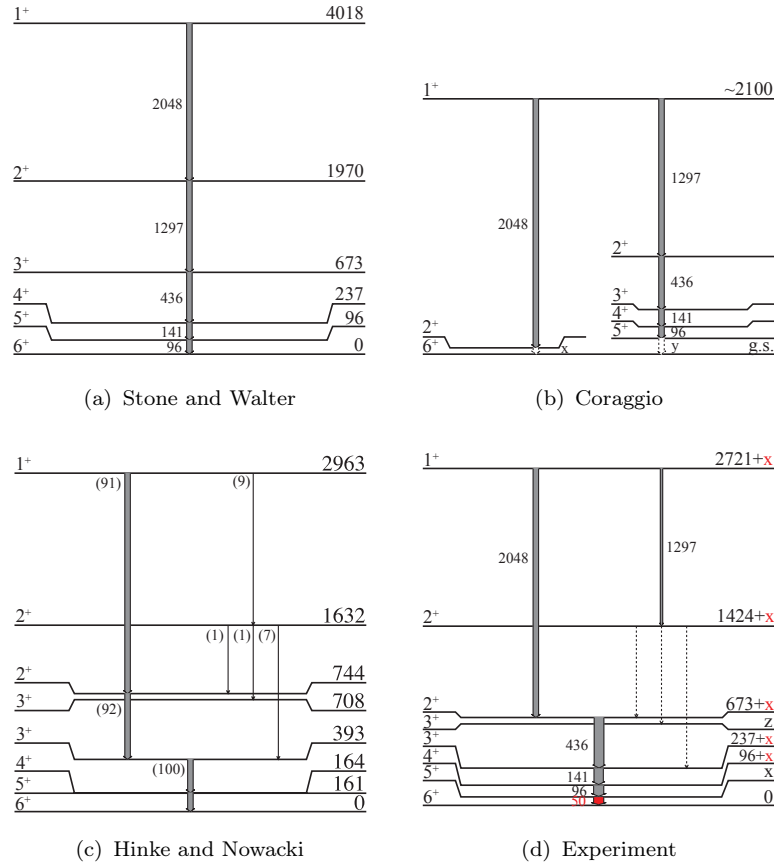


**Figure 4.17:** Possible scenarios for the level scheme of  $^{100}\text{In}$  proposed by calculations of Stone and Walter [SW85] and Coraggio et al. [Cor+04] as well as H. Grawe [Hin10] and the proposed scheme from the previous experiment by Hinke et al. [Hin+12]. Figures in brackets denote the calculated branching ratios of the corresponding transitions.

is correlated with  $^{100}\text{Sn}$ . Decay correlations were considered within 5 s after the implantation in the same pixel and its neighboring pixels on the long edges (no diagonal pixels). Due to the wider window compared to the single pixel correlations and narrower time windows the background increases. But at the same time transitions with lower intensities become feasible as the decay of  $^{100}\text{In}$  is visible by the correlated  $\gamma$ -transitions of  $^{100}\text{Cd}$  ( $\rightarrow$  Fig. 4.18). The  $\gamma$ -spectroscopy was performed with both spectra, those which are generated from the single  $\gamma$ -ray energy deposit and those which had the adback algorithm applied ( $\rightarrow$  Sec. 2.4.3). All known transitions originating from excited states in  $^{100}\text{In}$  are clearly visible. The background was accounted for by considering  $\gamma$ -emission in the implantation history. The occurrence of the emission lines which belong to the  $\beta$ -decay of  $^{100}\text{In}$  shows that the background subtraction is fine and transitions with smaller branching ratios are accessible. Besides these emission lines, there are a few “peaks” attracting attention with regards to low intensity transitions in scenario c. A detailed comparison of these lines with the background shows that strong lines occur at these energies in the background analysis. Since the peaks cannot be certainly confirmed to coincide with fluctuations which originate in the background correction, they are investigated in the range of expected transitions with low intensities. In particular, a transition with an energy of 1175.3 keV is known in  $^{99}\text{Cd}$  [Lip+02] implying a  $\beta$ -delayed proton decay of  $^{100}\text{Sn}$ . But this could not be confirmed by the study of  $\gamma$ -radiation which

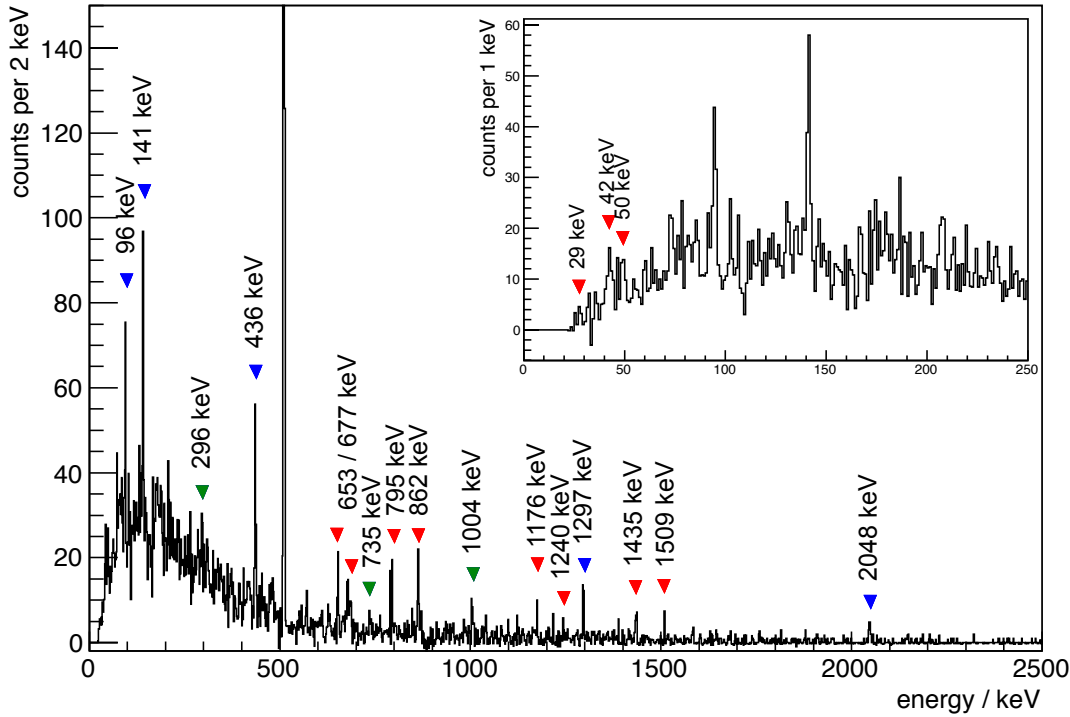


**Figure 4.18:** Background corrected  $\gamma$ -spectrum obtained from addback energies with a time window of 5 s and a spatial gate of  $3 \times 3$  Pixels. The labels mark known transitions of  $^{100}\text{In}$  (blue) and  $^{100}\text{Cd}$  (green) as well as lines which were studied with regard to suggested transitions according to the scenarios (red). Inset: Background corrected spectrum of single  $\gamma$ -energies (no addback method applied).

is correlated with  $\beta p$ -events. In the low energy range which was studied by the analysis of a  $\gamma$ -spectrum of single events (no addback), the peaks at 29 keV, 42 keV and 50 keV attract attention because they correspond to previously discussed transitions which are dominated by internal conversion. The 29 keV line is identified to originate from the X-ray emission of the  $K_\alpha$ -shell. The emission at 42 keV has a broadened structure compared to known transitions at higher energies but the emission at 50 keV has a nice shape with regard to the detector resolution. The expected intensities of both lines is  $\sim 6$  counts where the fractions of internal conversion of 86% and 80% were taken into account in the calculation. The  $\gamma$ -efficiency was estimated to 2.5% as the uncertainties of the efficiency calibration ( $\rightarrow$  Fig. 2.13) are large with regard to the steep slope at low energies. Thus, the intensity of the emission line at 50 keV just matches the expectation and one coincidence with the emission of 2048 keV was observed. Hence, this 50 keV transition is a candidate for the “x” in both scenarios b and c. The peak which occurs at 42 keV shows coincidences with the emission of 511 keV confirming the origin in decay events and the coincidences with 436 keV as well as 1297 keV suggest that this transition also belongs to the level scheme of  $^{100}\text{In}$ . However, the broad structure of this transition indicates a larger contribution by Compton-scattering events such that these events could solely be random coincidences.

Regarding the low intensity transitions of scenario c, their efficiency corrected estimate for the number of expected counts is  $5 \pm 2$  counts for  $2^+ \rightarrow 3^+$  with 1239 keV and less than 1 count for the other two transitions ( $\rightarrow$  Fig. 4.17(c)). This holds equivalently for

the level scheme as derived by [Hin+12]. Thus, there was only a chance to find these transitions by a coincidence analysis if the branching ratios of the calculations apply to the experiment because even the expected number of events of the transition with the highest intensity is close to the background level. Here, the absolute intensities of the first transition of each branch suggest an equal branching ratio. The uncertainties are rather high but even in case of a maximum deviation within  $1\sigma$  of both intensities, the branching ratios of 2048 keV and 1297 keV, are 0.74 and 0.26, respectively. These intensities are normalized with respect to their sum. Thus, at least the proposed transition with  $\sim 1200$  keV should have been observed.

The coincidence analysis of transitions with energies of 96 keV, 141 keV, 436 keV as well as 1297 keV ( $\rightarrow$  Fig. 4.20) unambiguously identifies that they belong to the same cascade and confirm the decay scheme as proposed in the previous GSI experiment ( $\rightarrow$  Fig. 4.17(d)). Concerning the emission with an energy of 2048 keV, one coincidence with the transition of 96 keV was observed. Considering the  $\gamma$ -efficiency at 96 keV being smaller compared to 141 keV, 1 event which shows a coincidence

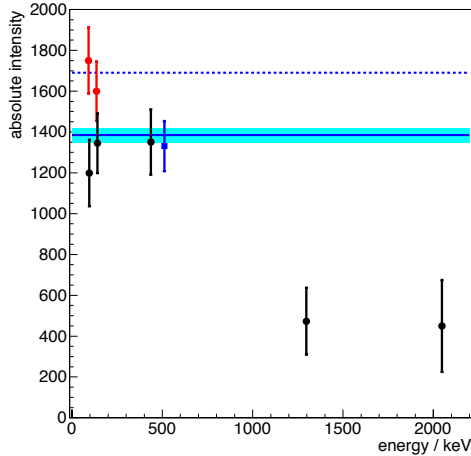


**Figure 4.19:** Absolute intensities of the  $\gamma$ -transitions in  $^{100}\text{In}$ . The sum of the intensities at 1297 keV and 2048 keV corresponds to the corrected number of implantations. Intensities are corrected for M1 (black) and E2 conversion (red) which is negligible for energies above 400 keV because of small conversion coefficients but has a dramatic effect on the transitions of 96 keV and 141 keV. The dashed line is the number of decays expected from the number implantations in DSSD B. The intensities were derived in a time window of 3 s. The number of observable decays is obtained by the dead time and electron capture corrections (blue). The fraction of emission at 511 keV is corrected for the contribution by the daughter decay and the fact that each annihilation releases two  $\gamma$ -rays of 511 keV.

between  $\gamma$ -emission with 141 keV and 2048 keV would be also expected when 15 counts are observed at 2048 keV. The detailed study of the correlations with the emission of 2048 keV also shows two interesting coincidences with an energy 85.81 keV and 84.98 keV as well as one coincidence with the above mentioned 50 keV emission. Considering the emission which is expected according to the transitions with smaller intensities in the addback spectrum, especially the emission at 653 keV and 677 keV is interesting because their sum of 1330 keV is equal to the difference of 1328 keV of the  $1424+x$  state and the  $96+x$  state regarding the HPGe-detector resolution of  $\sim 3$  keV. Both lines also appear in the background but the ratio of both, the 653 keV and 677 keV emission is different in the background spectrum and the background subtracted spectrum of decay correlations. The enhancement of the 653 keV and 677 keV transitions exceeds the background level by 37 and 45 counts, respectively. However, no more than three counts are expected according to the calculations. The coincidence analysis reveals one coincidence between the two of them while 3 counts would be expected with the observed intensities. Another chance to investigate the origin of these lines is a coincidence with emis-

sion at 440 keV which would follow from a second branch of the  $z$ -state. One branch of the  $1424+x$  state decays by a cascade of these two lines, the  $z$ -state would be populated resulting in a subsequent transition with an energy of 440 keV. But the adjacent area of the 436 keV emission does not show evidence for this transition. More information of the level scheme is obtained by considering the absolute  $\gamma$ -intensities ( $\rightarrow$  Fig. 4.19). The

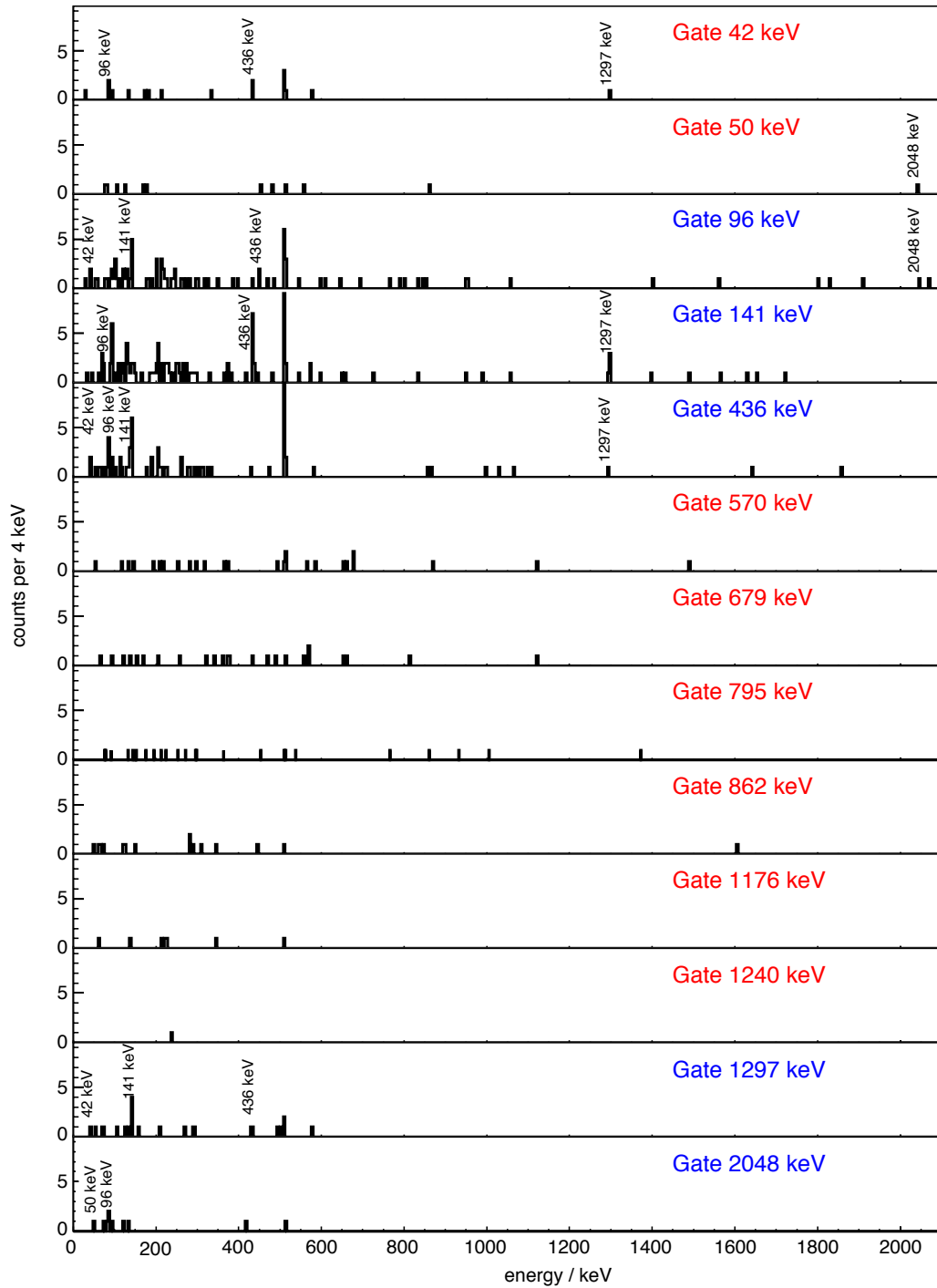


**Figure 4.20:** Coincidence analysis of  $\gamma$ -emission in  $^{100}\text{In}$  which is shown in Figure 4.18 using a correlation time window of 5 s and a spatial correlation by considering its direct neighbors.

number of observed  $\gamma$ -events is corrected for M1 and E2 conversion affecting the lower energies dramatically. The consistency of this numbers is checked by comparison with the number of implantations and the efficiency corrected number of emission of 511 keV ( $\rightarrow$  Fig. 4.19). It has been also accounted for the losses due to electron capture and dead time. Furthermore, the integral of the annihilation peak at 511 keV is corrected for the contribution of the daughter decay. Then, the overlap of the intensity of the annihilation peak with the number of implantations confirms the method.

The obtained intensities show that the transitions at 96 keV, 141 keV and 436 keV have equal intensities as well as those at 1297 keV and 2048 keV. In conclusion, the latter two must belong to different branches which both feed the cascade of the former three transitions.

All things considered, the coincidence analysis and the study of the absolute intensities confirm the level scenario which was proposed by Hinke et al. [Hin+12]. The coincidence of 50 keV with 2048 keV is expected to be the missing link between the  $5^+$  and  $6^+$ -state of  $^{100}\text{In}$ . In agreement with the shell model calculations of each scenario, the correction for M1-conversion and E2-conversion of the low energy transition suggests that the character is rather M1 than E2 from the comparison of the number of implantations and the absolute intensities. But the confirmation of the link between the 2048 keV transition and the level scheme as well as the transitions which connect the  $2^+$ -state with the lower  $3^+$ -state and  $4^+$ -state remain open questions.

### 4.3 Search for the Isomeric $6^+$ -state of $^{100}\text{Sn}$

Excitations of neighboring nuclei of  $^{100}\text{Sn}$  have been studied extensively and cascades of E2-transitions were identified in  $N=Z$  nuclei. A shell model calculation by Grawe [Gra04] predicts a  $2^+, 4^+$  and  $6^+$ -state with transition energies of  $\sim 3000$  keV,  $\sim 1300$  keV and  $\sim 100$  keV, respectively. ( $\rightarrow$  Fig. 4.21(a)). The  $6^+$ -state is expected to be isomeric with a half-life of  $\sim 100$  ns to a few  $\mu\text{s}$  depending whether it dominantly decays by direct proton decay. Since the number of implanted nuclei in the present experiment is much higher than in the frequently referred experiment by Hinke et al. [Hin+12], there is a new chance to search for the  $6^+$ -isomer which is expected to have a transition to a  $4^+$ -state at energies between 100 keV and 300 keV with an upper limit for its half-life given by  $T_{1/2}^{6^+} < 1 \mu\text{s}$ . The TDCs as well as the the DGF modules allow for the observation of short-lived isomers in the range of 10 ns. The information about the isomeric states is obtained from the energy-time correlations of  $\gamma$ -emission after an implantation of  $^{100}\text{Sn}$  ( $\rightarrow$  Fig. 4.21(a)). Indeed, a few delayed counts occur at  $E_\gamma = 180$  keV but the trace is too weak to be clearly distinguished from background events. Transitions at 3004 keV, where 4 counts at  $E_\gamma = 3004$  keV were previously reported as 'not very probable' [Hin10], have also not been observed in this experiment.

In conclusion, further efforts are necessary with regards to the search of the  $6^+$ -isomeric state and the de-excitation cascade of  $^{100}\text{Sn}$ . The  $6^+$  isomeric state has to be searched for by implantation spectroscopy while the first excited  $2^+$ -state is accessible in Coulomb excitation experiments.

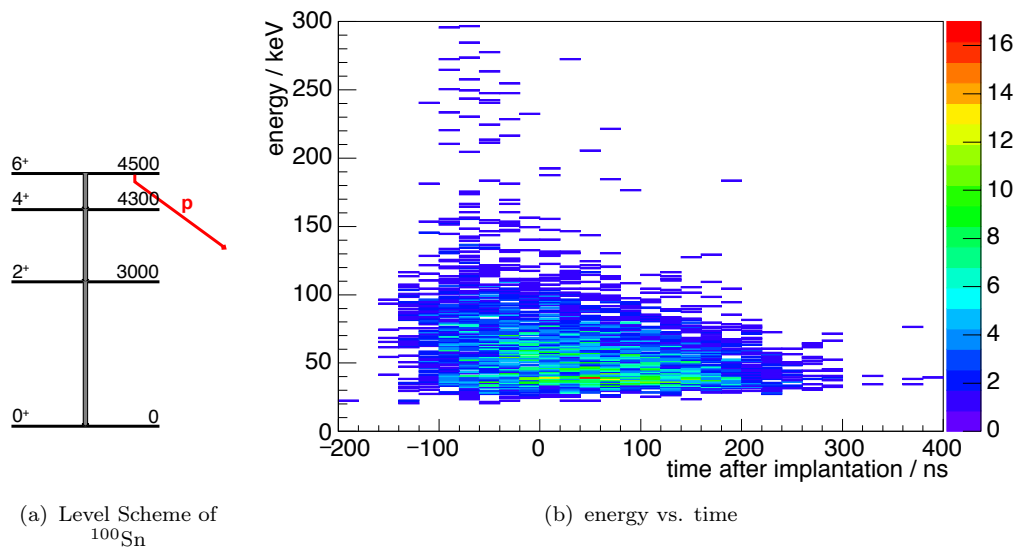


**Figure 4.21:** Left: Level scheme of  $^{100}\text{Sn}$  described by Grawe [Gra04]. Right: Energy-vs-time plot of  $\gamma$ -emission correlated with  $^{100}\text{Sn}$  implantations. No clearly delayed transitions are visible and the spectrum dilutes to higher energies.

## 4.4 $Q_\beta$ -Value & Transition Strength

The phase space part of the  $\log(ft)$ -value depends on the fifth power of the  $Q_\beta$ -value while the half-life affects this measure only linearly. Hence, the precision of the Gamow-Teller transition strength  $\mathcal{B}_{\text{GT}}$ , which is proportional to the inverse product of  $f(Z, Q_\beta)T_{1/2}$ , is crucially affected by the precision of the  $Q_\beta$ -value. For that reason, a precise calibration and the detailed discussion how to determine the exact energy deposit of  $\beta^+$ -particles in Section 3.4 was necessary in order to achieve a  $\mathcal{B}_{\text{GT}}$  which can challenge different theoretical model calculations. At first, the  $Q_\beta$ -value of  $^{100}\text{Sn}$  is derived and in a second step the transition strength is determined.

### 4.4.1 The $\beta$ -Endpoint Energy of $^{100}\text{Sn}$

The determination of the  $Q_\beta$ -value of the  $\beta$ -decay of  $^{100}\text{Sn}$  from the endpoint energy of the positron spectrum is the last step to be performed before the Gamow-Teller transition strength  $\mathcal{B}_{\text{GT}}$  is calculated. This is committed by applying a GEANT4-simulation using a positron source in the center of the middle implantation detector with a Gaussian spatial distribution which is derived experimentally according to the distribution of  $^{100}\text{Sn}$  implantations. The energy input is given by the  $Q_\beta$ -distribution. The  $\chi^2$ -method is applied in order to derive the best-fitting simulation by means of a  $\chi^2$ -test as described in Section 3.4.2.

In contrast to the determination of the  $Q_\beta$ -value of  $^{98}\text{Cd}$  in the test case, a  $\gamma$ -gate was not applied here because it contributes only to improve the statistical uncertainties if the background is not sufficiently well-determined. In this case, the background was determined from a 10 s time window of decay correlations which occurred before the implantation. Considering 1780 implantations for the correlation analysis and a time window of 3 s, the  $\gamma$ -gate has selected less than 150 decay events while no spatial

restriction was applied. Furthermore, the  $\gamma$ -gated energy spectrum were contaminated by contributions which coincide with Compton-scattered  $\gamma$ -emission with 96 keV and 141 keV. A selection by only higher  $\gamma$ -energies where such contributions are negligible would further decrease the sample size.

In case of a spatial restriction to single pixels and their direct neighbors (adjacent to the long edges) with a time window of 3 s and no  $\gamma$ -gate applied, 1070 events remain after subtraction of the contributions by the daughter component and background which improves the statistical uncertainty by 30% to 50% while the contribution from the background is 20% at maximum. Therefore, the  $Q_\beta$ -value is derived by an event selection which considers all decay correlations within the time window of 3 s. The experimental  $Q_\beta$ -spectrum is shown in Figure 4.23.

Thus, as the  $\gamma$ -gate is not applied, the contribution of the daughter decays to the energy spectrum has to be considered. The  $Q_\beta$ -values of the transitions of  $^{100}\text{In} \rightarrow ^{100}\text{Cd}$  were determined by a total absorption spectrometry experiment and tabulated for  $\beta^+/\text{EC}$  as well as  $\beta p$ -channels [Ple+02]. The decay scheme of  $^{100}\text{Sn}$  ( $\rightarrow$  Fig. 4.22) including the daughter decay shows that the  $\beta^+$ -decay of  $^{100}\text{In}$  is highly fragmented. The intensities of transitions of lower energy ( $E < 3000$  keV) are accurately measured while the intensities for transitions into states above are given in steps of 200 keV. Then, 24 components of the  $\beta^+$ -decay were considered in the input  $Q_\beta$ -spectrum while the contribution from electron capture was dropped because it does not affect the electron spectrum. The contribution of decays from the daughter nucleus  $^{100}\text{In}$  with a half-life of 5.8(2) s is 19.8% in the time window of 3 s. Further contributions by the decay of the grand daughter nucleus are negligible because of a long half-life of  $^{100}\text{Cd}$  with  $T_{1/2} = 49.1$  s compared to the half-lives of the parent and daughter nucleus. The effect of conversion electrons which mainly originate from the transitions in  $^{100}\text{In}$  with energies of 147 keV, 198 keV and below is clearly visible by the enhancement of the experimental spectrum at energies  $E < 400$  keV.

The simulation resembles the shape of the experimental spectrum in agreement with the statistical uncertainties and the result of the comparison of both spectra by the  $\chi^2$ -method using  $\chi^2 = \sum \frac{|x_{\text{exp}} - x_{\text{sim}}|^2}{\sigma_{\text{exp}}^2}$  is shown in Figure 4.23. This  $\chi^2$  was determined for each simulation with an energy distribution for a certain  $Q_\beta$ -value. The minimum  $\chi_{\text{min}}^2$  in the plot yields the best-fitting  $Q_\beta$ -value. The range of comparison where the  $\chi^2$ -method has statistical significance by the change of the  $Q_\beta$ -input is between 600 keV and 3000 keV. The range below is strongly affected by the change of the position of the positron source ( $\rightarrow$  Fig. 3.7). In the range above, the main contributions of the spectrum are given by the daughter component and background such that this part of the spectrum does not contain valuable information. Furthermore, histogram bins with less than ten entries are not in agreement with the  $\chi^2$ -method because their statistical uncertainties are not Gaussian. The best-fitting  $Q_\beta$ -values result in the minimum  $\chi_{\text{min}}^2$  of the  $\chi^2$ -distribution which is obtained by a polynomial fit. It yields

$$Q_\beta(^{100}\text{Sn}) = (3.81^{+0.14}_{-0.14} \text{ stat. } ^{+0.10}_{-0.28} \text{ sys.}) \text{ MeV} \quad (4.19)$$

The systematic uncertainty, which is introduced by the minimization procedure, was determined by varying the fit range. At first, the upper limit was fixed at 3000 keV while

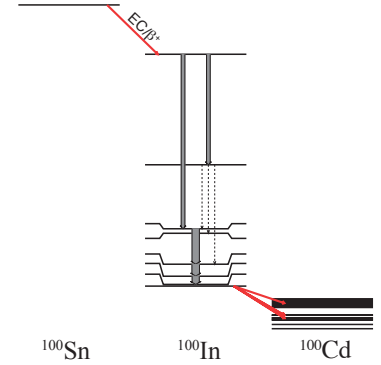


**Figure 4.22:** Level scheme schematic of  $^{100}\text{In}$  as suggested from the  $\beta$ -decay of  $^{100}\text{Sn}$  by Hinke et al. [Hin+12] and confirmed in this experiment ( $\rightarrow$  Fig. 4.17(d)). The transition strength of  $^{100}\text{Cd}$  is highly fragmented [Ple+02]. Each  $\beta$ -decay channel is considered in the **Geant4**-simulation.

the lower limit was varied ( $\rightarrow$  Fig. 4.23 b)). Secondly, the upper limit was varied with the lower limit fixed at 600 keV. The uncertainty which is associated with the selection of the fit range was determined by the maximum deviation of the best-fitting  $Q_\beta$ -values. It is not independent of the statistical uncertainties and therefore not considered as a separate contribution in the following discussion.

Furthermore, the  $Q_\beta$ -value in Equation (4.19) has to be corrected for the contribution of conversion electrons which deposit their energy in the Si-detectors, too. The corresponding conversion coefficients  $\alpha_{\text{tot}}$  are calculated to  $\alpha_{\text{tot}}^{96 \text{ keV}} = 0.637(17)$  and  $\alpha_{\text{tot}}^{141 \text{ keV}} = 0.216(6)$  according to Kibedi et al. [Kib+08]. The probability for internal conversion of  $\gamma$ -emission in terms of  $\alpha_{\text{tot}}$  is given by  $I_e = \frac{\alpha_{\text{tot}}}{1+\alpha_{\text{tot}}}$ . This results in  $I_e^{96 \text{ keV}} = 0.389$  and  $I_e^{141 \text{ keV}} = 0.178$ . Thus, the average contribution to the  $Q_\beta$ -spectrum from conversion electrons is  $\bar{E}_e = 0.389 \cdot 96 \text{ keV} + 0.178 \cdot 141 \text{ keV} \approx 63 \text{ keV}$  and the corrected  $Q_\beta$ -value is

$$Q_\beta^{\text{corr}}(^{100}\text{Sn}) = (3.74 \pm 0.14) \text{ MeV} \quad (4.20)$$

This value is between the results from previous experiments by Stolz [Sto02], when it was derived from 7 correlations,  $3.8_{-0.73}^{+0.28}$  MeV, and the experiment by Hinke et al. [Hin+12], when  $Q_\beta = 3.29 \pm 0.2$  MeV was derived from 70 correlations.

Comparing the  $1\sigma$ -confidence intervals, the new value has an improved statistical uncertainty by a factor of  $\sim 1.5$  which strongly affects the precision of the  $\mathcal{B}_{\text{Gt}}$ -value ( $\rightarrow$  next Section). Concerning the value by Hinke et al. [Hin+12], another systematic uncertainty of 200 keV associated with the influence of bremsstrahlung and annihilation radiation was reported. Therefore, even in case of a  $4\pi$ -geometry a simple fit of the positron energy distribution of the Si-detectors is not advisable in spite of a dominant  $0^+ \rightarrow 1^+$  GT-transition. In contrast to the previous analysis, these effects were also taken into account in the **Geant4**-simulation.

The  $Q$ -value analysis is concluded with the calculation of the  $Q_{\text{EC}}$ -values according to the scenarios of the level scheme of  $^{100}\text{In}$  which is given by the sum of the  $Q_\beta$ -value, the energy  $E(1_1^+)$  of the first excited  $1^+$ -state which is populated after the  $\beta$ -decay and the electron mass  $m_e$ .

$$Q_{\text{EC}} = Q_\beta + E(1_1^+) + 2m_e c^2 \quad (4.21)$$

$E(1^+)$  is given by 4018 keV, (2048+x) keV and (2721+y) keV according to scenario a), b) and c), respectively ( $\rightarrow$  Fig. 4.17), resulting in

$$Q_{\text{EC}}^{\text{a}} = (8.84 \pm 0.14) \text{ MeV} \quad (4.22)$$

$$Q_{\text{EC}}^{\text{b}} = (6.82 \pm 0.14) \text{ MeV} \quad (4.23)$$

$$Q_{\text{EC}}^{\text{c}} = (7.54 \pm 0.14) \text{ MeV} \quad (4.24)$$

Regarding a further selection of the scenarios for the level scheme of  $^{100}\text{In}$ , the mass measurement by Chartier et al. [Cha+96] who reports a mass difference between  $^{100}\text{Sn}$  and  $^{100}\text{In}$  of  $6.9 \pm 1.0$  MeV as well as the calculated mass difference of 7.03 MeV [WAW+12] are considered.

Scenario a), which suggests a single cascade, implies a large splitting between the  $\nu g_{7/2}$  and  $\nu d_{5/2}$ -orbitals introducing a significant change in the matrix elements of the  $\pi g_{9/2} \nu g_{7/2}$  and  $\pi g_{9/2} \nu d_{5/2}$  interactions. The difference between the  $Q_{\text{EC}}^{\text{a}}$ -value further increases so that a single cascade becomes even less likely as the results do not overlap within  $1.5\sigma$ .

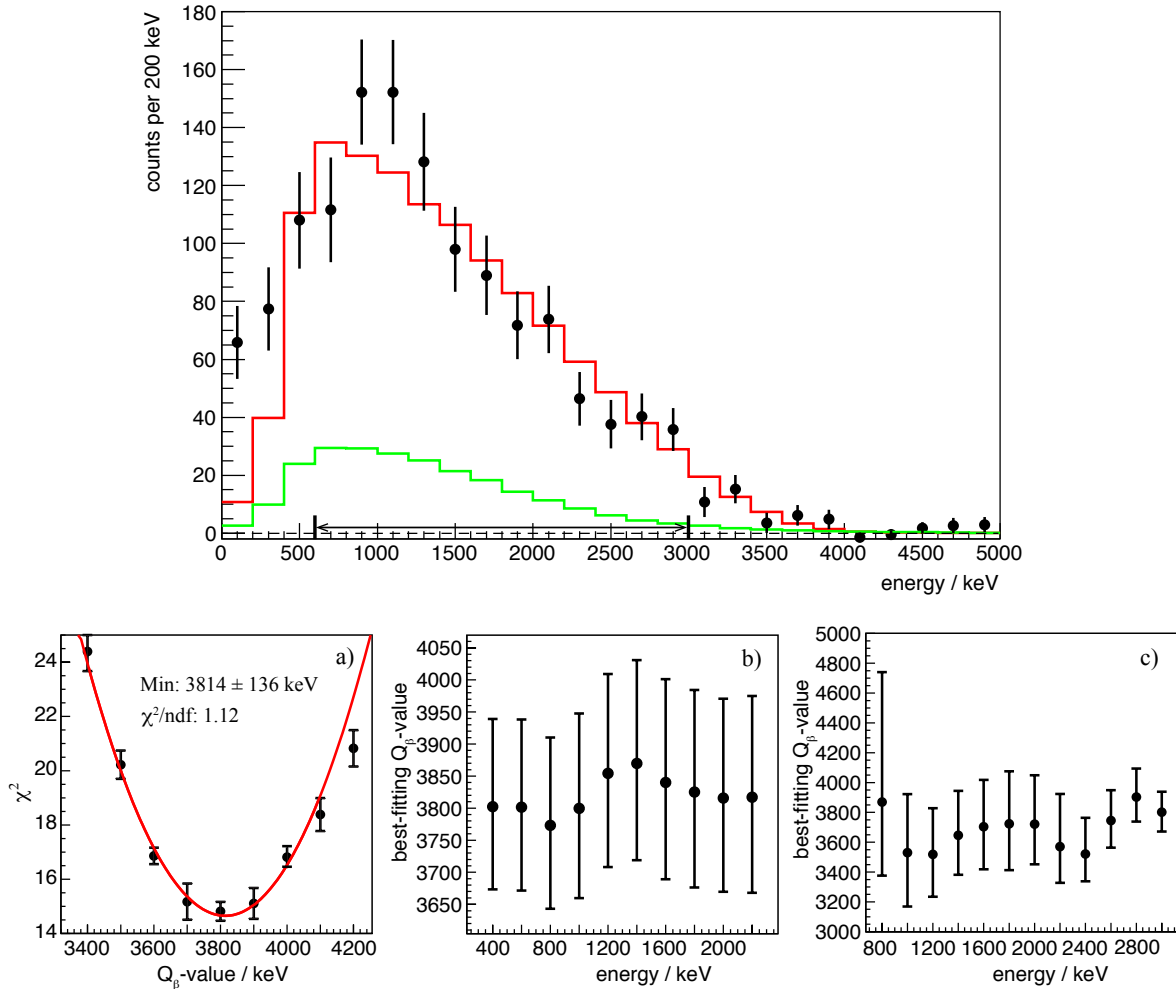


**Figure 4.23:** Background corrected experimental spectrum of positron energy deposit in Si-detectors for single pixel and adjacent pixel correlations within a time window of 3 s (black). The error bars consist of the Gaussian sum of the statistical uncertainties of the decay correlations and the subtracted background. The red curve represents the `Geant4`-simulation which is associated with the minimum in the  $\chi^2$ -test, with a population size of  $10^5$  normalized to the integral number of the experiment. The green curve shows the daughter component of the fit model. Lower Panels: a)  $\chi^2$ -values of the comparison of the experiment and simulations at different  $Q_\beta$ -values. The error bars denote the statistical uncertainties which are introduced by the simulation. b) Analysis of systematic uncertainties by the variation of the lower fit range while the upper fit range is fixed at 3000 keV. c) Opposite from b) while the lower limit is fixed at 600 keV.

Concerning the  $Q_{\text{EC}}^{\text{b,c}}$ , both certainly overlap with the value of the mass measurement where the only uncertainty in the level schemes arises from the missing M1 or E2 transitions, respectively, which accounts for the spin difference from  $1^+$  to  $6^+$ . Hence, if this transition exists, the transition energy has to be below 100 keV accounting for a low detection efficiency because of conversion. The emission at 50 keV was tentatively assigned to originate from this transition ( $\rightarrow$  Fig. 4.20) such that the  $Q_{\text{EC}}$ -values of each scenario could be precisely calculated. Remarkably, the  $Q_{\text{EC}}^{\text{b}}$ -value of scenario b is in good agreement with the results of the mass measurement and with the predicted mass. However, the scenario cannot ultimately be concluded by the  $Q_{\text{EC}}^{\text{b}}$ -analysis because of a large uncertainty of 1 MeV of the mass measurement. Even though, the range of the  $Q_{\text{EC}}$ -value or the mass difference of the decay of  $^{100}\text{Sn}$  is narrowed down to 6.53 MeV to 7.76 MeV.

#### 4.4.2 The Gamow-Teller Transition Strength of $^{100}\text{Sn}$

Both experimental inputs of the Gamow-Teller transition strength  $\mathcal{B}_{\text{GT}}$  have been determined, the half-life and the  $Q_\beta$ -value. Thus, the  $\mathcal{B}_{\text{GT}}$ -value can be determined according to the derivation in the introduction after a long journey of treating time and energy measurements.  $^{100}\text{Sn}$  has been explained to decay dominantly by a pure  $0^+ \rightarrow 1^+$  GT-transition that the transition strength is simplified as described in Appendix A and is calculated from

$$\mathcal{B}_{\text{GT}} = \frac{3811.5 \text{ s}}{f(Z, Q_\beta) \cdot T_{1/2}} \quad (4.25)$$

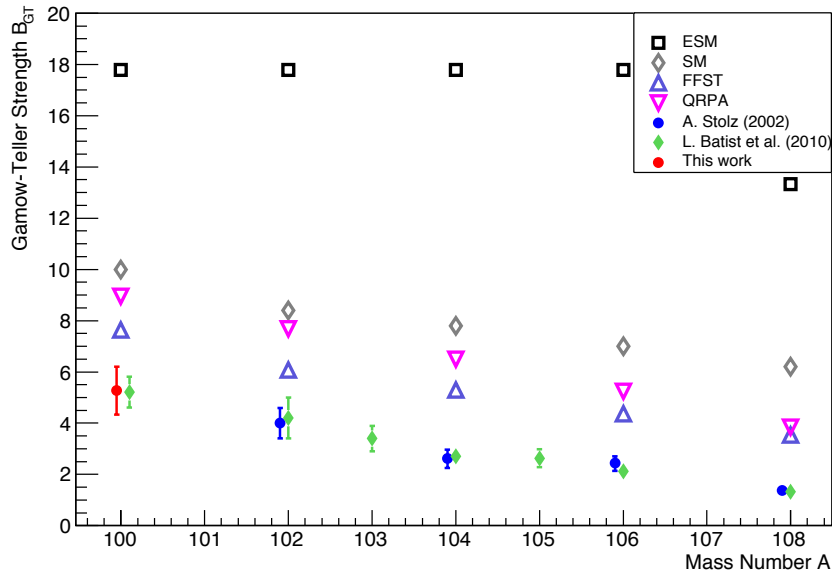
with the proton number  $Z$  of the daughter nucleus, the  $Q_\beta$ -value and the half-life  $T_{1/2}$ . The  $ft$ -value was calculated by using the NNDC LOGFT calculator [Nat16b] with the inputs  $1.17 \pm 0.10 \text{ s}$  for the half-life  $T_{1/2}$  and  $3.74 \pm 0.14_{\text{stat.}}$  for the  $Q_\beta$ -value which yields

$$\log(ft) = 2.86^{+0.08}_{-0.08} \text{ stat.} \quad (4.26)$$

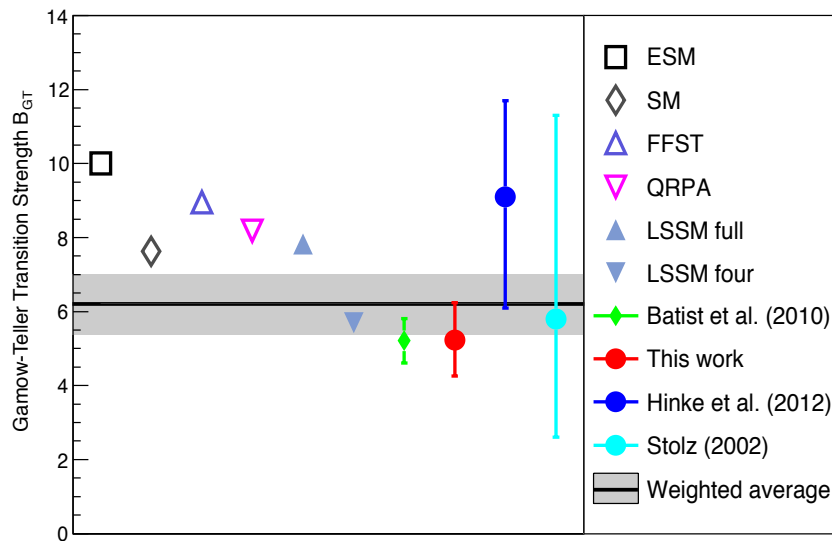
$$\mathcal{B}_{\text{GT}} = 5.26^{+0.90}_{-1.06} \text{ stat.} \quad (4.27)$$

The result is shown in comparison with theoretical calculations and previous experimental results in Figure 4.24. The statistical uncertainty has obviously improved to previous measurements and calculations of the Finite Fermi System Theory, Quasi Random Phase Approximations and Large Scale Shell Model (LSSM) calculations are very close to the weighted average which is calculated from the experimental values of the present as well as previous experiments ( $\rightarrow$  Fig. 4.24(b)). The systematic uncertainty appears rather large but compared to previous methods using an analytic fit  $Q_\beta$ -spectrum this value is of the same order. Considering that the dominant contribution of the systematic uncertainty originates from fit ranges with less confined limits due to the deviations of the bin entries, the systematic uncertainty is not independent from the statistical uncertainty. The calculation of the  $\mathcal{B}_{\text{GT}}$ -value in the Extreme Single Particle Model results in an extremely high value of 17.78 ( $\rightarrow$  Eqn. (1.12)) and the lower measured transition strength was described by a hindrance factor attributed to the renormalization of  $\frac{g_A}{g_V} = 1$  instead of  $\frac{g_A}{g_V} = 1.27$ . This resulted in a  $\mathcal{B}_{\text{GT}}$ -value of 10. In contrast, LSSM calculations revealed that the missing strength is attributed to an incomplete model space and the fact, that higher  $1^+$ -states exist in  $^{100}\text{In}$ . LSSM calculations by Hinke et al. [Hin+12], Brown and

Rykaczewski [BR94] as well as Hamamoto and Sagawa [HS93] predict several excited  $1^+$ -states being in good agreement while the lowest  $1^+$ -state dominantly contributes. Thus, the calculations by Hinke et al. [Hin+12] result in  $\mathcal{B}_{\text{GT}} = 8.19$  if all possible final states are considered and  $\mathcal{B}_{\text{GT}} = 7.82$  for all final states within the  $Q_{\text{EC}}$  window. The contribution of the first excited  $1^+$  state to the total transition strength is predicted as 5.7. This value was compared to the reduced observed transition strength of  $7.6^{+2.2}_{-2.5}$  where the reduction is caused by further accessible but unobservable states while the actual determined value was  $9.1^{+2.6}_{-3.0}$ . The measured value of  $5.26^{+0.90}_{-1.06}$  stat. agrees with the extrapolated value of  $5.21 \pm 0.60$ . It is consistent with the results obtained by Stolz [Sto02] and Hinke et al. [Hin+12] while the overlap with the latter confidence intervals is remarkably small. The result of the  $\mathcal{B}_{\text{GT}}$ -value has clearly shown the strong effect of the improved accuracy of the  $Q_{\beta}$ -value on the transition strength. The comparison of this  $\mathcal{B}_{\text{GT}}$ -value with those obtained from theoretical calculations is shown in Figure 4.24. From the experimental point of view, the transition strength of  $^{100}\text{Sn}$  rather follows a trend of  $\mathcal{B}_{\text{GT}}$ -values of its neighboring isotopes than being an exception. Still, the  $\log(ft)$ -value of this nucleus keeps its uniqueness as it remains the smallest one throughout the nuclear chart.



(a) neighboring even Sn-isotopes

(b)  $B_{GT}$  of  $^{100}\text{Sn}$ : theory & experiment

**Figure 4.24:** a) Gamow-Teller transition strength of Sn-isotopes from theory and experiment. The lower values compared to the ESM model are clearly visible. The values of  $^{102-108}\text{Sn}$  by Batist et al. [Bat+03] are experimental values while the value for  $^{100}\text{Sn}$  was extrapolated. b) Comparison of the results of the Gamow-Teller transition strength of  $^{100}\text{Sn}$  from previous experiments and calculations. The extrapolation and the LSSM calculation considering four possible  $1^+$ -states agree very well. LSSM labels the results for the  $B_{GT}$  of calculations [Hin+12]. LSSM full: summed strength of all possible states, LSSM four: summed strength of the first four excited states. FFST: results from the Finite Fermi System theory [BK00] and QRPA: results from quasi random phase approximation [BK00].

# 5 Summary & Prospects

## 5.1 Summary of the Results

The present experiment is a joint effort of the EURICA RIBF09 collaboration with the TUM group as a leading partner. The EURICA  $\gamma$ -spectrometer of a European collaboration was maintained and prepared for a series of experiments in Japan. The WAS3ABi array was specifically assembled for this experiment so that  $\beta$ -delayed  $\gamma$ -spectroscopy could be performed with high resolution in time and energy while high-resolution  $\beta$ -calorimetry was possible in parallel. A major fraction of the data analysis was performed within the framework of this thesis with a set of different findings.

Four nuclei,  $^{90}\text{Pd}$ ,  $^{92}\text{Ag}$ ,  $^{94}\text{Cd}$  and  $^{96}\text{In}$ , along the  $N = Z - 2$  line were newly identified with the high-resolution magnetic separator BigRIPS and half-lives were measured for the first time.

On the  $N = Z - 1$  line,  $^{93}\text{Ag}$  was ultimately confirmed as a proton emitter which was suggested by the anomaly in the implantation intensities compared to its neighbors when a non-selective population by the fragment separator is assumed. The half-life was determined rather precisely by considering the ratios of implantations between  $Z \pm 1$  neighbors on the  $N = Z$  and  $N = Z - 1$  line which resulted in  $228 \pm 16$  ns. In contrast, the half-lives of the other  $N = Z - 1$  nuclei were derived from their decay curves by using the unbinned MLH-method. The half-lives of these nuclei are very similar and the fit results in values between 27 ms and 33 ms for each of them with statistical uncertainties of less than 6 ms.

Regarding nuclei on the  $N = Z$  line, the determination of the Gamow-Teller transition strength of  $^{100}\text{Sn}$  was a main goal of the experiment which has been achieved with an improved precision. The value is  $\mathcal{B}_{\text{GT}} = 5.26^{+0.90}_{-1.06}$  corresponding to the smallest  $\log(ft)$ -value in the nuclear chart of  $\log(ft) = 2.86 \pm 0.08$ . By the measurement of the half-life to  $T_{1/2} = 1.17 \pm 0.10$  s and the  $Q_{\beta}$ -value to  $Q_{\beta} = 3.74 \pm 0.14$  MeV unprecedented precision was achieved by using a  $\chi^2$ -method in comparison to the results of **Geant4**-simulations. Using this method, the dependence of the detector response on the spatial distribution of implantations and effects such as bremsstrahlung and annihilation radiation were included into a fit model which has significantly improved the reliability of the determined  $Q_{\beta}$ -values. The systematic uncertainties due to the detector geometry, electronic noise or contributions from the daughter decays were minimized. The determination of the half-life of  $^{100}\text{Sn}$  was checked by a  $\gamma$ -gated event selection for the first time using  $N = 204$  decay correlations. The experimental  $\mathcal{B}_{\text{GT}}$  is in very good agreement with the prediction of  $\mathcal{B}_{\text{GT}}^{\text{LSSM}} = 5.8$  by LSSM calculations which include large configuration spaces [Hin+12]. The ordering of the level scheme of  $^{100}\text{In}$  was confirmed by the  $\beta$ -delayed  $\gamma$ -spectroscopy of  $^{100}\text{Sn}$  using the HPGe-detectors of EURICA. The combination of absolute  $\gamma$ -intensities and a  $\gamma$ - $\gamma$  coincidence analysis has revealed a candidate for the missing link between a  $5^+ \rightarrow 6^+$  transition with an energy of 50 keV. In contrast to the LSSM calculations, the measured transition intensities suggest two branches with a similar branching rather

than a single dominant one. The additional low intensity transitions from a strongly fragmented branch proposed by these calculations have not been observed yet. Other nuclei which were studied in detail along the  $N = Z$  line are the isotopes  $^{98}\text{In}$ ,  $^{94}\text{Ag}$  and  $^{90}\text{Rh}$ . The branching of the  $\beta$ -decay of  $^{98}\text{In}$  into the  $8^+$ -state and the core-excited  $10^+$ -state of  $^{98}\text{Cd}$  is a strong indication for an isomeric  $9^+$ -state which is populated in the production process. The decay correlations of  $^{98}\text{In}$  show a slow and a fast decay component which belong to the  $T = 0$  and  $T = 1$  states, respectively. Gamma-correlations with each of the components of the decay curve suggest also a  $0^+$ -state populating the ground state of  $^{98}\text{Cd}$  and the existence of the expected  $T = 0$ ,  $9^+$ -state. However, the level ordering of these two states is still under discussion. This was also addressed by a comparison of their absolute level energies with respect to the ground state of the daughter nucleus. By considering the  $\beta$ -decay into the ground state of  $^{98}\text{Cd}$  and the branching into the  $\beta p$ -channel the absolute energy of the expected  $9^+$ -state could be placed  $1.4 \pm 1.9$  MeV above the  $0^+$ -state in  $^{98}\text{In}$ . The next odd-odd  $N = Z$  nucleus  $^{94}\text{Ag}$  shows similar characteristics in its decay curve as well as in the correlated  $\gamma$ -radiation. This nucleus was reported earlier to decay also by  $1p$ - and  $2p$ -emission which was not observed in this experiment. In agreement with the expectations of their corresponding branching ratios. The lightest  $N = Z$  nucleus, which was implanted in WAS3ABi was the  $^{90}\text{Rh}$ -isotope. For the first time, this nucleus could be studied in detail. An isomeric state was inferred from the decay curve and the correlated  $\gamma$ -emission. The  $\gamma$ -spectroscopy revealed the level ordering of the lowest states in the daughter nucleus  $^{90}\text{Ru}$  as well as additional  $\gamma$ -emissions with energies of 1163 keV and 1316 keV which have not been reported yet. The selection rules of the  $\beta$ -decay were used to assign tentatively a spin-parity of  $5^+$  to the long-lived state in  $^{90}\text{Rh}$ .

## 5.2 Why the Region of $^{100}\text{Sn}$ Remains Interesting

In addition to the observables, which have been investigated within the framework of this thesis, other measures such as the masses,  $B(E2)$ -values or deformation parameters are important for the description of the nuclear structure. In particular, the  $B(E2)$ -values and the excitation energies of  $2_1^+$ -states provide an experimental signature of the nuclear structure. Sn-isotopes with even neutron numbers from  $N = 50$  to  $N = 82$  show an almost constant  $2_1^+$ -energies [Nat16a]. They are well-established but the  $B(E2)$ -values, which are accessible in Coulomb-excitation experiments, show deviations from the parabolic shape proposed by theoretical predictions. However, these experiments need high-production cross section of secondary beam projectiles. These

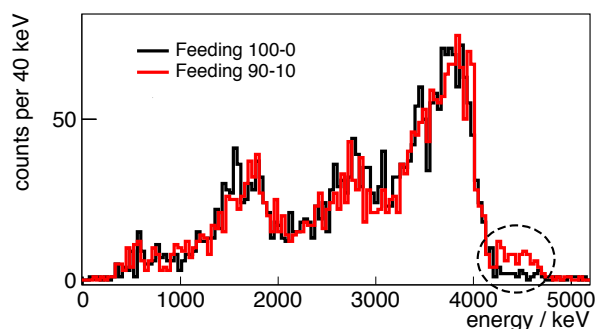


**Figure 5.1:** Simulated TAS spectrum of  $\gamma$ -emission which is correlated with the subsequent  $\beta$ -decay of 3000  $^{100}\text{Sn}$  implantations with a feeding of 100% of the lowest  $1_1^+$ -state of  $^{100}\text{In}$  (red) and a feeding of 90% [Alg+16]. In the latter case, the remaining 10% populate another  $1_2^+$ -state which is expected at an energy of 744 keV above. The transition are identified by the peaks at  $2963+1022$  keV and  $744+1022$  keV. The difference between both spectra above 4000 keV originates from the feeding of the second  $1^+$ -state.

These

rates are achievable for  $^{102}\text{Sn}$  at the RIBF. Therefore, big efforts are already taken to measure the  $B(E2)$ -value of this nucleus in the near future.

While the  $B(E2)$ -values of  $^{100}\text{Sn}$  will remain inaccessible for the next few years, total absorption spectrometry (TAS) could investigate the level scheme of  $^{100}\text{In}$  being sensitive on the measurement of additional  $1^+$ -states. Algorta et al. [Alg+16] has already proposed such an experiment. The reported efficiency for the detection of a  $\gamma$ -cascade of at least two  $\gamma$ -rays are more than 98%. Hence, the level scheme scenarios could be discriminated with available beam production rates. According to a simulation ( $\rightarrow$  Fig. 5.1), the spectrometer is also sensitive on the population of another  $1^+$ -state if the branching ratio is  $\sim 10\%$ . The photopeak efficiency of 46% of this detection system allows also for the search of a  $6^+$ -state.

A complementary measure to investigate the scenario is the mass difference of  $^{100}\text{Sn}$  and  $^{100}\text{In}$ . The accuracy of the known value of this mass difference is only 1 MeV which was not enough to discriminate the scenarios in combination with the measurements of the  $Q_\beta$ -value. A significant improvement of the precision in the mass measurement down to several 10 keV of nuclei in the region around  $^{100}\text{Sn}$  could be achieved with a storage ring such as the Collector Ring (CR) which is under construction at the future facility FAIR at GSI [Dol+15; Ger16].

### 5.3 Summary of the Half-Lives

Nucleus	$J^\pi$	T = (N-Z)/2	Half-lives		$\beta p$ / %
			This Work	Literature	
$^{100}\text{Sn}$	$0^+$	0	$(1.17 \pm 0.10)$ s	$(1.16 \pm 0.20)$ s <sup>1)</sup> , $0.55^{+0.70}_{-0.31}$ s <sup>2)</sup>	< 0.1
$^{99}\text{Sn}$		$-\frac{1}{2}$	$(27 \pm 6)$ ms	> 200 ns <sup>3)</sup>	< 7.0
$^{100}\text{In}$	$(6^+, 7^+)$	+1	$(5.8 \pm 0.2)$ s	$5.7(3)$ s <sup>4)</sup> , $5.9(2)$ s <sup>5)</sup>	
$^{98}\text{In}(0^+)$	$0^+$	0	$(29 \pm 1)$ ms	$32^{+32}_{-11}$ ms <sup>6)</sup> , $47(13)$ ms <sup>4)</sup> , $(47 \pm 13)$ ms <sup>2)</sup>	< 2.7
$^{98}\text{In}(9^+)$	$(9^+)$	0	$(0.86 \pm 0.04)$ s	$1.2^{+1.2}_{-0.4}$ s <sup>6)</sup> , $1.27(30)$ s <sup>4)</sup> , $(0.66 \pm 0.4)$ s <sup>2)</sup>	
$^{98}\text{In}(\beta p)$	$(9^+)$	0	$(0.87 \pm 0.06)$ s	$135(65)$ ms, $1.27(30)$ s <sup>4)</sup>	8.1(5)
$^{97}\text{In}$	$\frac{9}{2}^+$	$-\frac{1}{2}$	$(32 \pm 6)$ ms	$26^{+47}_{-10}$ ms <sup>3)</sup>	
$^{96}\text{In}$		-1	$17^{+82}_{-8}$ ms	—	—
$^{96}\text{Cd}^{0+}$	$0^+$	0	$(1.16 \pm 0.09)$ ms	$(0.67 \pm 0.15)$ s <sup>7)</sup> , $1.03^{+0.24}_{-0.21}$ s <sup>2)</sup>	
$^{96}\text{Cd}^{16+}$	$16^+$	0	$(0.54 \pm 0.06)$ ms	$0.29 + 0.11_{-0.10}$ s <sup>7)</sup> , $0.5$ s <sup>8)</sup>	
$^{95}\text{Cd}$	$\frac{9}{2}^+$	$-\frac{1}{2}$	$(33 \pm 4)$ ms	$73^{+53}_{-28}$ ms <sup>3)</sup>	2.3(17)
$^{94}\text{Ag}(0^+)$	$0^+$	0	$(28 \pm 2)$ ms	$26^{+26}_{-9}$ ms <sup>9)</sup>	
$^{94}\text{Ag}(7^+)$		0	$(0.49 \pm 0.02)$ s	$(7^+) : 0.55(6)$ s, $(21^+) : 0.40(4)$ s <sup>9)</sup>	
$^{94}\text{Ag}(\beta p)$	$7^+$	0	$(0.44 \pm 0.05)$ s	—	3.2(3)
$^{93}\text{Ag}(p)$		$-\frac{1}{2}$	$228 \pm 16$ ns	> 200 ns <sup>3)</sup>	
$^{93}\text{Ag}(\beta)$		$-\frac{1}{2}$	$27 \pm 7$ ms	—	—
$^{92}\text{Ag}$		-1	$12^{+22}_{-5}$ ms	—	—
$^{92}\text{Pd}$	$0^+$	0	$(1.25 \pm 0.03)$ s	$0.7^{+0.4}_{-0.2}$ <sup>10)</sup> , $1.0^{+0.3}_{-0.2}$ <sup>9)</sup>	1.2(2)
$^{91}\text{Pd}$		$-\frac{1}{2}$	$(32 \pm 4)$ ms	—	1.0 (10)
$^{90}\text{Pd}$		-1	$40^{+191}_{-19}$ ms	—	—
$^{90}\text{Rh}(0^+)$	$0^+$	0	$(27 \pm 4)$ ms	$12^{+9}_{-4}$ ms <sup>9)</sup>	
$^{90}\text{Rh}(5^+)$	$(5^+)$	0	$(0.50 \pm 0.04)$ s	$1.0^{+0.3}_{-0.2}$ s <sup>9)</sup>	
$^{90}\text{Rh}(\beta p)$	$(5^+)$	0	$(0.49 \pm 0.09)$ s	—	2.8(4)

**Table 5.1:** Summary of half-lives and branching ratios of the decay channel of  $\beta$ -delayed protons. The half-lives are compared with literature values. References: <sup>1)</sup> [Hin+12], <sup>2)</sup> [Baz+08], <sup>3)</sup> [SH+10], <sup>4)</sup> [Lor+12], <sup>5)</sup> [Ple+02], <sup>6)</sup> [Kie96], <sup>7)</sup> [Nar+11], <sup>8)</sup> [Oga+83], <sup>9)</sup> [Nat16a], <sup>10)</sup> [Wef+00]

## A The Gamow-Teller Transition Strength

In this chapter, the derivation of the expressions for the  $\log(ft)$ -value in Equation (1.13) is derived starting from the transition rate. If a nucleus in the initial state  $\langle i |$  decays into the final state  $\langle f |$  of its daughter nucleus, the matrix element is given by  $\mathcal{M} = \langle f | \mathcal{H}_{V-A} | i \rangle$  with the Hamiltonian

$$\mathcal{H}_{V-A} = \frac{1}{\sqrt{2}} \int d^3r \cdot \bar{\psi}_p g_V \gamma^\mu (1 - g_A \gamma_5) \psi_n \cdot \bar{\psi}_e \gamma_\mu (1 - \gamma_5) \psi_\nu \quad (\text{A.1})$$

$\gamma^\mu$  denotes the Lorentz-invariant  $\gamma$ -matrices,  $g_V$  denotes the vector coupling constant and  $g_A$  the axial coupling constant. The wave functions of the proton, neutron, electron and neutrino are labeled by  $\psi_{p,n,e,\nu}$ , correspondingly. Considering Fermi's Golden rule, the transition rate of a nucleus is written as

$$d\lambda dE_e dE_\nu = \frac{2\pi}{\hbar} |\mathcal{M}|^2 \delta(\epsilon_0 - \epsilon_e - \epsilon_\nu - \epsilon_R) \quad (\text{A.2})$$

with the reaction energy  $\epsilon_0$ , the energy of the recoil  $\epsilon_R$ , the electron energy  $\epsilon_e$  and the energy of the neutrino  $\epsilon_\nu$ . The recoil energy is negligible as it is of the order of some eV and the fixed energy  $\delta$ -distribution where the recoil energy is negligible due to the large mass of the nucleus. Since, the neutrino is usually not observed, its energy is expressed in terms of the reaction energy  $\epsilon_0$  and the electron energy  $\epsilon_e$  resulting in

$$d\lambda dE_e = \mathcal{K} \frac{2\pi}{\hbar} |\mathcal{M}|^2 \epsilon_e \sqrt{\epsilon_e^2 - m_e^2 c^4} (\epsilon_0 - \epsilon_e)^2 d\epsilon_e \quad (\text{A.3})$$

where  $\mathcal{K} = \mathcal{V}(4\pi)^2 / (2\pi\hbar \cdot c)^6$  with the normalization volume  $\mathcal{V}$ . The matrix element  $\mathcal{M}$  depends on the nuclear charge of the daughter nucleus  $Z$  and the reaction energy  $\epsilon_0$  which originates from the perturbation of the wave functions by the Coulomb interaction. This is represented by a factor which is known as Fermi's function  $F(Z, \epsilon_0)$ . Integrating Equation (A.3) in order to obtain the total transition rate, the phase space is written as

$$f(Z, \epsilon_0) = \int_0^{\epsilon_0} F(Z, \epsilon) \epsilon \sqrt{\epsilon^2 - 1} (\epsilon_0 - \epsilon)^2 d\epsilon \quad (\text{A.4})$$

and with the transition rate  $\lambda = \frac{\ln(2)}{T_{\frac{1}{2}}}$  it results

$$f(Z, \epsilon_0) \cdot T_{\frac{1}{2}} = \frac{\ln(2)}{\mathcal{K}} \frac{1}{\mathcal{M}} \quad (\text{A.5})$$

Writing the matrix element  $\mathcal{M}$  in terms of the Fermi-transition and the Gamow-Teller transition, it separates into

$$f(Z, \epsilon_0) \cdot T_{1/2} = \mathcal{C} \frac{\ln(2)}{g_V^2 |\mathcal{M}_F|^2 + g_A^2 |\mathcal{M}_{GT}|^2} \quad (\text{A.6})$$

with  $\mathcal{C} = \frac{2\pi^3 \hbar^7}{g^2 m_e^5 c^4}$ . Finally, substituting the matrix elements by the definitions of the transition strengths  $\mathcal{B}_F$  and  $\mathcal{B}_{GT}$  according to equations (1.10) and (1.11), it yields

$$f(Z, \epsilon_0) \cdot t_{1/2} = \frac{6142.8 \text{ s}}{\mathcal{B}_F + \frac{g_A}{g_V} \cdot \mathcal{B}_{GT}} \quad (\text{A.7})$$

where the ratio  $\frac{g_A}{g_V} = 1.2695 \pm 0.0029$  was determined by the decay of the free neutron decay  $n \rightarrow p + e^- + \bar{\nu}_e$  [Eid+04]. Then, if the decay proceeds by a single Gamow-Teller transition and Fermi-transitions are absent, the calculation of the  $\mathcal{B}_{\text{GT}}$ -value is simplified as

$$\mathcal{B}_{\text{GT}} = \frac{3811.5 \text{ s}}{f(Z', \epsilon_0) \cdot t_{1/2}} \quad (\text{A.8})$$

In case of several accessible final states for the  $\beta$ -decay,  $\mathcal{B}_{\text{GT}}$  is given by the sum over all decay channels with the corresponding phase space factors  $\sum_i 3830/f_i t_i$ .

## B The Fermi-Function

The perturbation of the matrix element by the Coulomb interaction between the nuclear charge and the electron considering plane wave functions was explicitly calculated by Fermi [Fer34]. The correction of the wave function is derived analytically by solving the Schrödinger Equation for the Coulomb potential.

$$F(Z, \epsilon_0) = \frac{1}{\Gamma(3 + 2S)^2} \rho^{2S} \eta^{2+2S} \exp(\pi\gamma \frac{\sqrt{1-\eta^2}}{\eta}) \left| \Gamma(1 + S + i\gamma \frac{\sqrt{1-\eta^2}}{\eta}) \right|^2 \quad (\text{B.1})$$

where  $S = \sqrt{1 - \gamma^2}$ ,  $\gamma = \alpha Z$  and  $\rho$  the nuclear radius.  $\Gamma$  denotes the Gamma-function and  $\alpha$  is the fine-structure constant. According to Mott and Massey [MM33], the square of the absolute of the wave functions at the origin of the nucleus as a solution of the wave equation with a Coulomb-potential is given by  $|\psi|^2 = \frac{2\pi\nu}{e^{2\pi\nu} - 1}$  that the Fermi-function is approximately written as

$$F(Z, \epsilon_0) \approx \frac{2\pi\nu}{1 - e^{-2\pi\nu}} \quad \nu = \mp \frac{Z\alpha}{v_e/c} \quad (\text{B.2})$$

with  $v_e$  is the velocity when the  $\beta$ -particle carries the complete energy which is available after the reaction. This approximation is valid because the  $\beta$ -decay proceeds inside the nucleus and slow electrons imply a high probability at the origin. On the opposite, if this approximation is applied to the  $\alpha$ -decay,  $\alpha$  is small and fulfills the condition of the Born approximation such as the Coulomb potential  $V(r)$  is treated as a perturbation.

## C The Construction of the p.d.f for the First Correlation

The probability that a transition occurs within a time  $dt$  with a decay constant  $\lambda$  is derived by the law of radioactive decay  $dN \propto \lambda N(t)dt$ . The evolution of species following the parent decay is governed by the Bateman Equations ( $\rightarrow$  Sec. 3.1.3). In the following, the explicit expressions of the probability distributions are shown for the parent and daughter decay labeled by 1 and 2, respectively. The probability density of the radioactive decay with the decay constant  $\lambda_1$  of a parent nucleus at a time  $t$  follows directly from the law of radioactive decay.

$$f_1(\lambda_1, t) = \lambda_1 \cdot \exp(-\lambda_1 t) \quad (\text{C.1})$$

where the integral

$$F_1(\lambda_1) = \int_0^t f_1(\lambda_1, t') dt' = 1 - \exp(-\lambda_1 t) \quad (\text{C.2})$$

is the probability that a particle has decayed until the time  $t$ . The same holds for the daughter species where the probability density and the integral expression are written as

$$f_2(\lambda_1, \lambda_2, t) = \frac{\lambda_1 \lambda_2}{\lambda_2 - \lambda_1} \left[ \exp(-\lambda_1 t) - \exp(-\lambda_2 t) \right] \quad (\text{C.3})$$

$$F_2(\lambda_1, \lambda_2, t) = 1 - \frac{\lambda_1 \lambda_2}{\lambda_2 - \lambda_1} \left[ \frac{1}{\lambda_1} \exp(-\lambda_1 t) - \frac{1}{\lambda_2} \exp(-\lambda_2 t) \right] \quad (\text{C.4})$$

Concerning the construction of a probability density to describe the activity in a detector, background events have to be considered as well. The probability of observing an event within a time window  $t_c$  in a spatially confined area at a constant background rate  $b_r$  is given by the Poisson distribution where  $r$  denotes the number of events observed within  $t_c$ .

$$B_r = \frac{(bt_c)^r \exp(-bt_c)}{r!} \quad (\text{C.5})$$

Considering event scenarios with decays which proceed in a chain, one observed event might have different origin corresponding to the parent, daughter and background. Therefore, the complementary probability distribution of the expressions, given above, are written

$$\bar{F}(\lambda, t) = 1 - F(\lambda, t) \quad (\text{C.6})$$

Suppose, the probability of the observation of a certain event is given by the detection efficiency  $\epsilon$ , the complement is written as

$$\bar{\epsilon} = 1 - \epsilon \quad (\text{C.7})$$

After this preparations, the probability distribution for the correlation of only first decay events after a certain implantation is symbolically given by

$$D_1 O_1 B_0 + D_1 \bar{O}_1 B_1 + \bar{D}_1 B_1 + D_1 \bar{O}_1 D_2 O_2 B_0 + D_1 \bar{O}_1 D_2 \bar{O}_2 B_1 + D_1 \bar{O}_1 \bar{D}_2 B_1 \quad (\text{C.8})$$

where  $D_i$  denotes that a nucleus has decayed,  $O_i$  denotes that the corresponding decay was observed and  $B_r$  denotes the probability that a number of  $r$  background events has occurred in the time window between the implantation and the decay correlation. Substituting the above expressions into Equation (C.8), it yields

$$\begin{aligned} p(\lambda_1, \lambda_2, t) = \mathcal{C} \cdot & \left( f_1(\lambda_1, t) \epsilon_1 B_0 + f_1(\lambda_1, t) \bar{\epsilon}_1 \frac{B_1}{t} \right. \\ & + \overline{F_1(\lambda_1, t)} \frac{B_1}{t} + F_1(\lambda_1, t) f_2(\lambda_1, \lambda_2, t) \bar{\epsilon}_1 \epsilon_2 B_0 \\ & \left. + F_1(\lambda_1, t) \bar{\epsilon}_1 F_2(\lambda_1, \lambda_2, t) \bar{\epsilon}_2 \frac{B_1}{t} + F_1(\lambda_1, t) \bar{\epsilon}_1 \overline{F_2(\lambda_1, \lambda_2, t)} \frac{B_1}{t} \right) \end{aligned} \quad (\text{C.9})$$

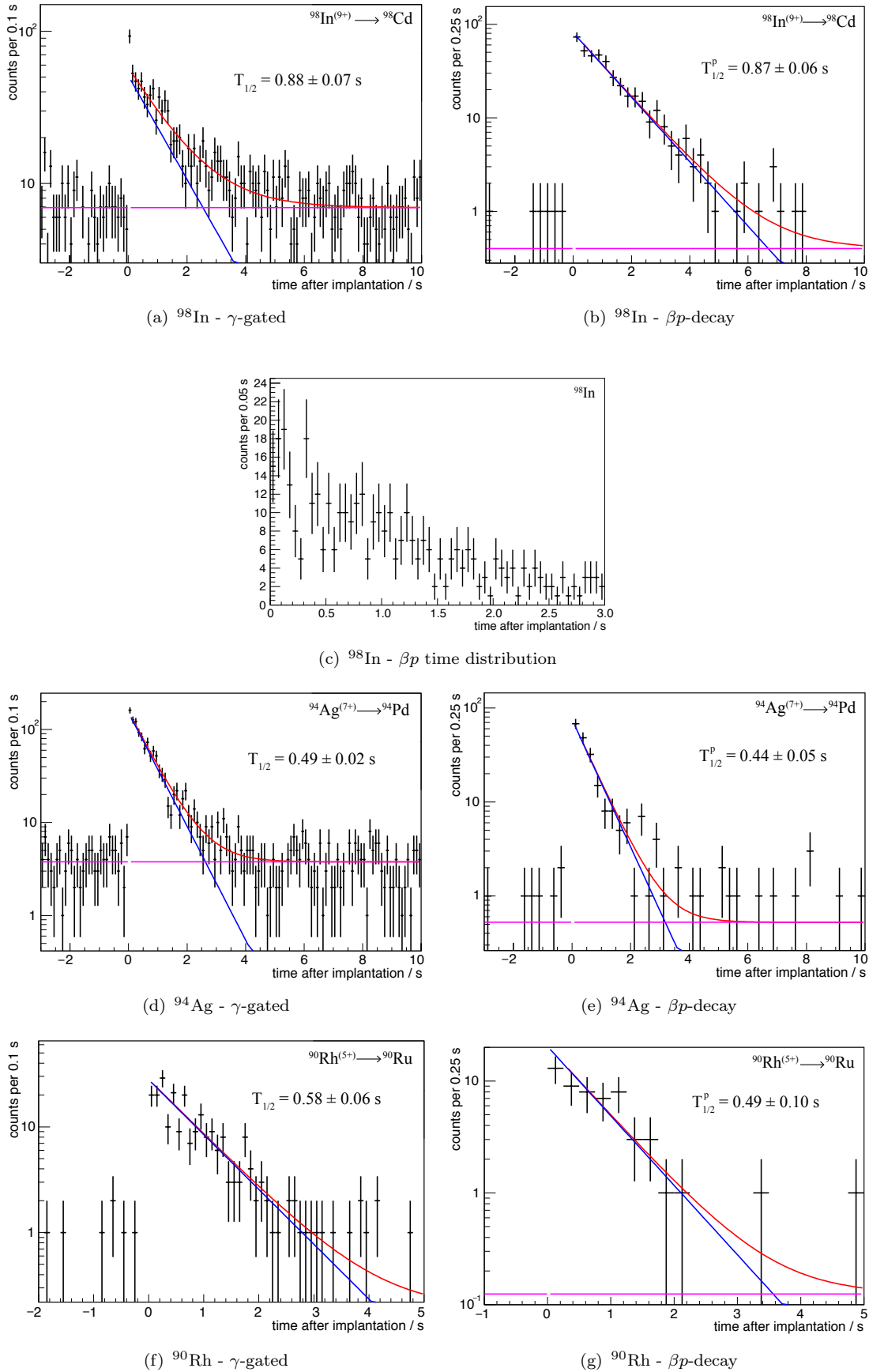
with the normalization constant  $\mathcal{C}$  and the normalization condition

$$\int_0^{t_c} p(\lambda_1, \lambda_2, t) dt = 1 \quad (\text{C.10})$$

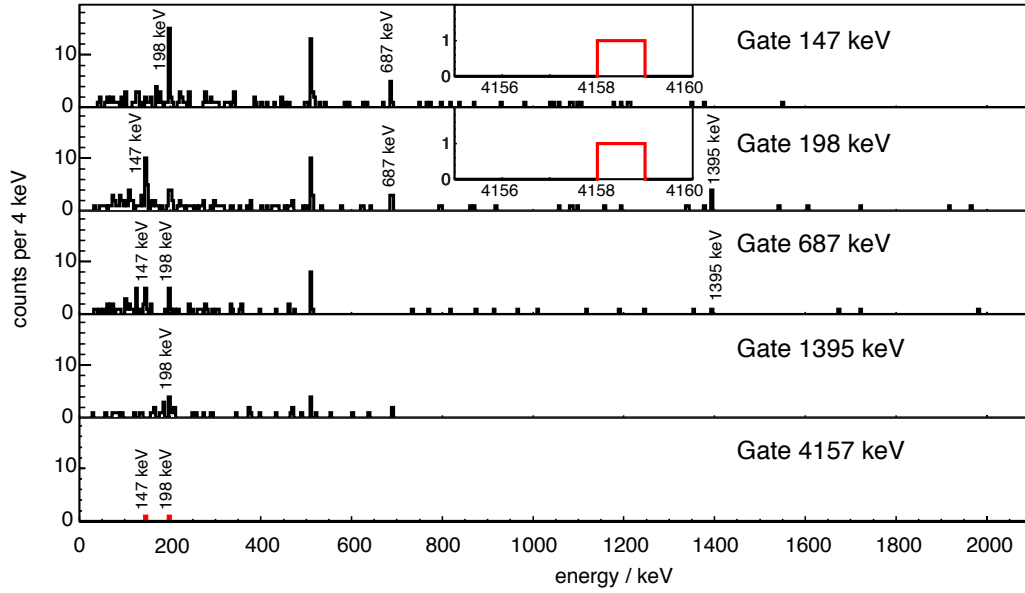
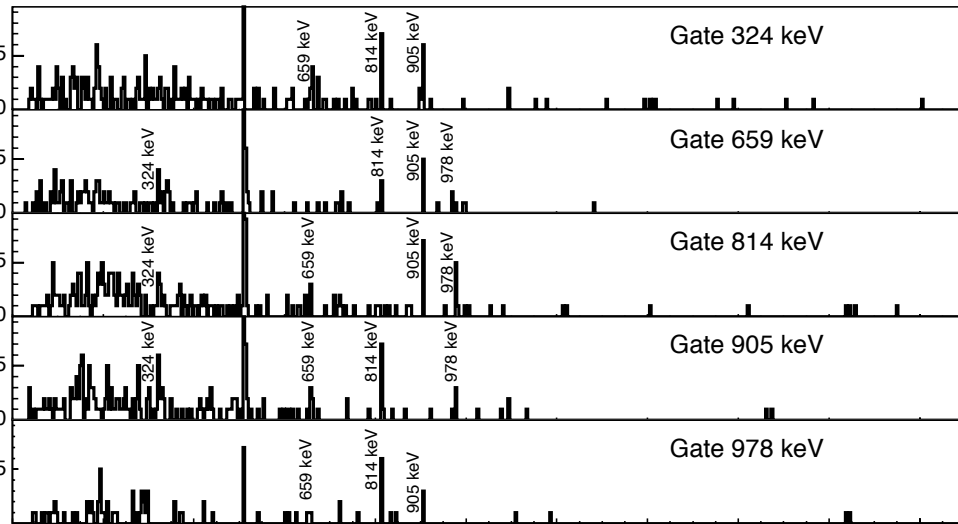
## D Half-Life Plots & Tables

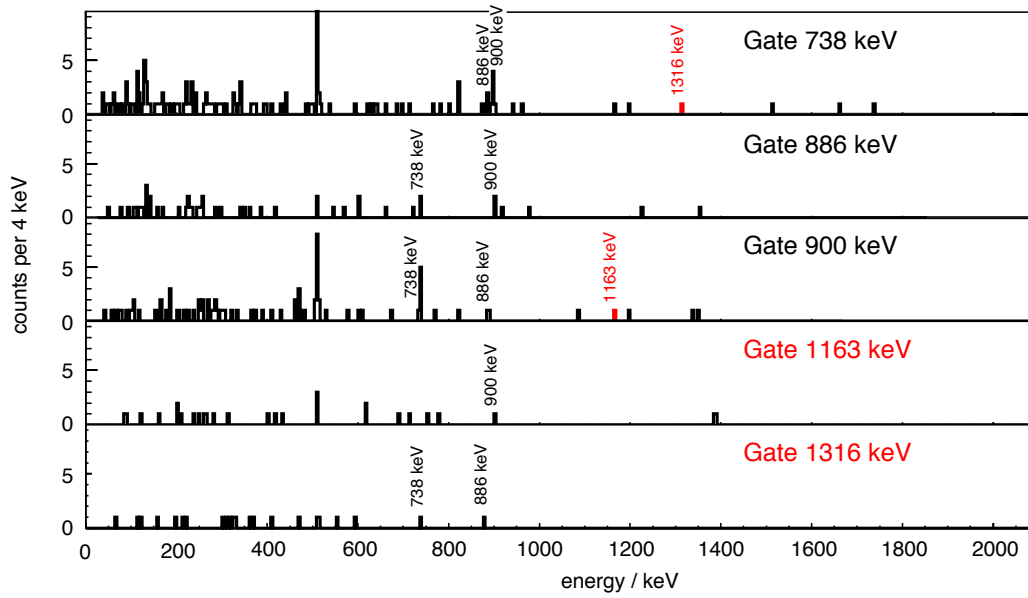
$^{96}\text{In}$	$^{94}\text{Cd}$	$^{92}\text{Ag}$	$^{90}\text{Pd}$
Before the implantation			
	-9.386	-7.589	
-3.807	-0.824	-5.931	
After the implantation			
<b>0.017</b>	<b>0.121</b>	<b>0.009</b>	<b>0.040</b>
4.300	<b>0.425</b>	<b>0.016</b>	9.331
10.048	1.417	6.078	
	6.411	11.769	
	7.846	12.832	
	8.252		
	10.614		

**Table D.1:** Decay correlations of implanted  $N = Z - 2$  nuclei. Numbers in bold denote the correlations which are certainly assigned to the decay of the implanted nucleus. All numbers are given in units of seconds.

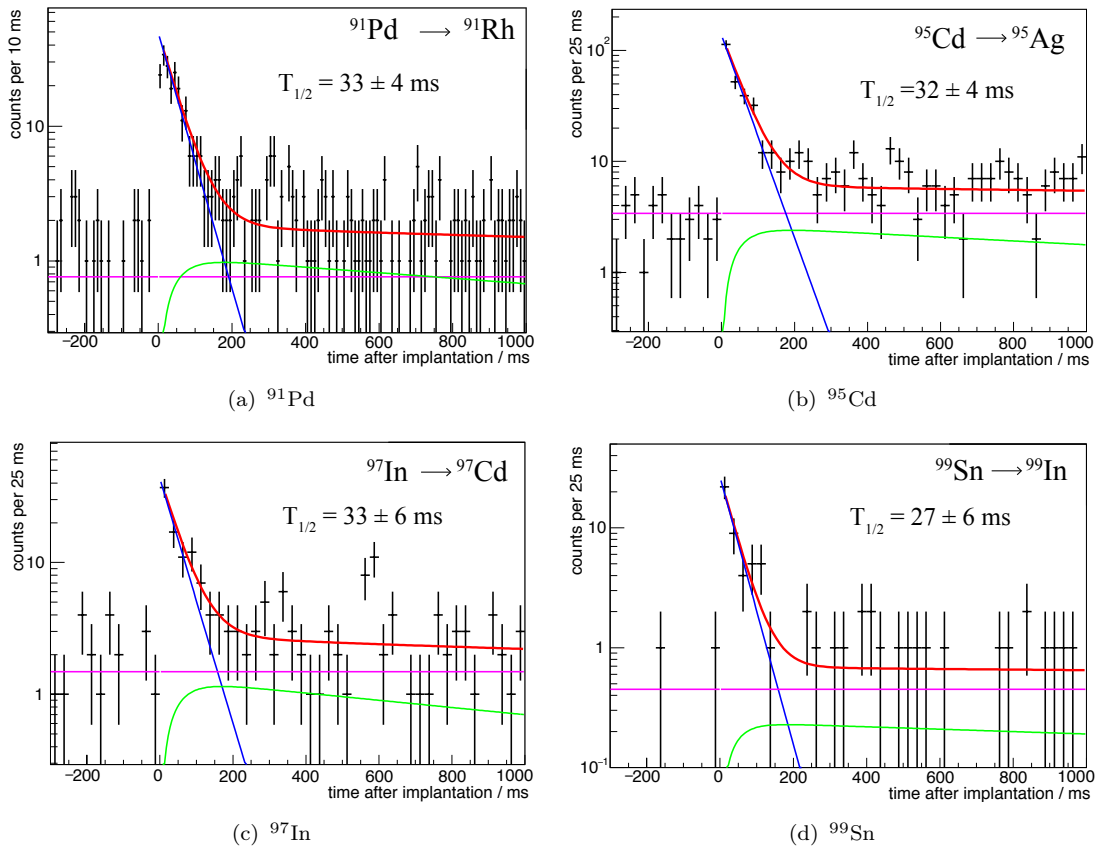


**Figure D.1:** Determination of half-lives of even-even  $N = Z$  nuclei  $^{98}\text{In}$ ,  $^{94}\text{Ag}$  and  $^{90}\text{Rh}$  by requiring corresponding  $\gamma$ -transitions (a,d,f) or by an event-selection of  $\beta p$ -decay events (b,e,g) ( $\rightarrow$  Sec. 4.1.4). Figure c) shows the time distribution of decay correlations with a  $\beta p$ -signature of  $^{98}\text{In}$  where only one decay component is apparent.

(a) coincidences of  $^{98}\text{In}$ (b) coincidences of  $^{94}\text{Ag}$ **Figure D.2:** Coincidences of  $^{98}\text{In}$  and  $^{94}\text{Ag}$ . The red bins mark the evidence for the  $9^+ \rightarrow 10^+$  Gamow-Teller transition.

(a) coincidences of  $^{90}\text{Rh}$ 

**Figure D.3:** Coincidences of  $^{90}\text{Rh}$ . The transitions in red mark lines which have been newly observed. The emission at 1163 keV is also not found to be associated with a daughter decay.

(a)  $^{91}\text{Pd}$ (b)  $^{95}\text{Cd}$ (c)  $^{97}\text{In}$ (d)  $^{99}\text{Sn}$ 

**Figure D.4:** Half-life fits of the  $N = Z - 1$  nuclei. The red curve is the fit result while the curves in blue, green and magenta show the parent, daughter and background components. The background was determined from the implantation history and applied as a fixed component to the actual fit.

# Bibliography

- [Ady98] T. E. Adye. “A Study of  $J/\psi$  Production at the LEP  $e^+e^-$  Collider; and the Implementation of the DELPHI Slow Controls System”. PhD thesis. Lincoln College, University of Oxford, 1998.
- [Alg+16] A. Algorta et al. “Studies of the beta decay of  $^{100}\text{Sn}$  and its neighbours with a Total Absorption spectrometer(TAS)”. *RIBF Proposal, RIKEN Nishina Center, Japan, Wako-shi* (2016).
- [APB97] M. S. Antony, A. Pape, and J. Britz. “Coulomb Displacement Energies Between Analog Levels for  $3 \leq A \leq 239$ ”. *Atomic Data and Nuclear Data Tables* 66 (1997), p. 1.
- [Aoi06] N. Aoi. “ $\gamma$ -ray spectroscopy at RIPS and BigRIPS”. *J. Phys. Conf. Ser.* 49 (2006), p. 190.
- [Ari+01] A. Arima et al. “Delta-hole interaction in nuclei and the Gamow-Teller strength in  $^{90}\text{Nb}$ ”. *Phys. Lett. B* 499 (2001), p. 104.
- [Bal+10] A. Balzhev et al. *J. Phys. Conf. Ser.* 205 (2010), p. 012035.
- [Bat10] H. Bateman. “Solution of a system of differential equations occurring in the theory of radioactive transformations”. *Proc. Cambridge Phil. Soc.* 15 (1910), p. 423.
- [Bat+03] L. Batist et al. “Isomerism in  $^{96}\text{Ag}$  and non-yrast levels in  $^{96}\text{Pd}$  and  $^{95}\text{Rh}$ , studied in  $\beta$  decay”. *Phys. Rep.* 720 (2003), p. 245.
- [Baz+08] D. Bazin et al. “Production and  $\beta$  Decay of rp-Process Nuclei  $^{96}\text{Cd}$ ,  $^{98}\text{In}$ , and  $^{100}\text{Sn}$ ”. *Phys. Rev. Lett.* 101 (2008), p. 252501.
- [Bec+05] F. Becker et al. “Status of the RISING project at GSI”. *Eur. Phys. J. A* 25.s01 (2005), p. 719.
- [BB36] H. A. Bethe and R. F. Bacher. “Nuclear Physics - A. Stationary States of Nuclei”. *Rev. Mod. Phys.* 8 (1936), p. 82.
- [Bla+10] A. Blazhev et al. “High-energy excited states in  $^{98}\text{Cd}$ ”. *J. Phys. Conf. Ser.* 205 (2010), p. 012035.
- [BK00] A. Bobyk and W. Kaminski. “Gamow-Teller beta-decay strengths of neutron-deficient tin isotopes: comparison of FFST and pnBCS+QRPA results”. *Acta Phys. Pol. B* 31.4 (2000), p. 953.
- [BR94] B. A. Brown and K. Rykaczewski. “Gamow-Teller strength in the region of  $^{100}\text{Sn}$ ”. *Phys. Rev. C* 50 (1994), p. 2270.
- [Bul79] M. G. Bulmer. “Principles of Statistics”. *Dover* (1979), p. 75.
- [CH81] X. Campi and J. Hüfner. “Nuclear spallation-fragmentation reactions induced by high-energy projectiles”. *Phys. Rev. C* 24 (1981), p. 2199.

- [Cau+05] E. Caurier et al. “The shell model as a unified view of nuclear structure”. *Rev. Mod. Phys.* 77 (2005), p. 427.
- [Ced+02] B. Cederwall et al. “Evidence for a spin-aligned neutron–proton paired phase from the level structure of  $^{92}\text{Pd}$ ”. *Eur. Phys. J. A* 15 (2002), p. 185.
- [Cel+16] I. Celikovic et al. “New isotopes and proton emitters - crossing the drip-line in the vicinity of  $^{100}\text{Sn}$ ”. *Phys. Rev. Lett.* 1 (2016), p. 1.
- [Cha+96] M. Chartier et al. “Mass Measurement of  $^{100}\text{Sn}$ ”. *Phys. Rev. Lett.* 77 (1996), p. 2400.
- [Cor+04] L. Coraggio et al. “Structure of particle-hole nuclei around  $^{100}\text{Sn}$ ”. *Phys. Rev. C* 70 (2004), p. 034310.
- [Cou00] R. Cousins. “Review of Particle Physics”. *Eur. Phys. J. C* 15 (2000), p. 195.
- [Cow+56] C.L. Cowan et al. “Detection of the free neutrino: a confirmation”. *Science* 124 (1956), p. 3212.
- [Dea+04] S. Dean et al. “The beta decay of neutron-deficient rhodium and ruthenium isotopes”. *Eur. Phys. J. A* 21 (2004), p. 243.
- [DLW06] D. S. Delion, R. J. Liotta, and R. Wyss. “Systematic of Proton Emission”. *Phys. Rev. Lett.* 96 (2006), p. 072501.
- [Dol+15] A. Dolinskii et al. “Collector ring project at FAIR”. *Phys. Scr. T* 166 (2015), p. 014040.
- [Ead+71] W. T. Eadie et al. *Statistical Methods in Experimental Physics*. Amsterdam, London: North-Holland Pub. Co., 1971.
- [Eid+04] S. Eidelman et al. “Baryon Particle Listings”. *Phys. Lett. B* 592 (2004), p. 864.
- [EH+08] K. Eppinger, C. Hinke, et al. “ $^{100}\text{Sn}$  and Nuclei in its Neighbourhood”. *GSI Scientific Report* (2008), p. 147.
- [FGG13] T. Faestermann, M. Gorska, and H. Grawe. “The structure of  $^{100}\text{Sn}$  and neighbouring nuclei”. *Prog. Part. Nucl. Phys.* 69 (2013).
- [Fae+02] T. Faestermann et al. “Decay studies of  $N \approx Z$  nuclei from  $^{75}\text{Sr}$  to  $^{102}\text{Sn}$ ”. *Eur. Phys. J. A* 15 (2002), p. 185.
- [Fer34] E. Fermi. “Versuch einer Theorie der  $\beta$ -Strahlen I”. *Z. Phys.* 88 (1934), p. 161.
- [Fuk+13] N. Fukuda et al. “Identification and separation of radioactive isotope beams by the BigRIPS separator at the RIKEN RI Beam Factory”. *Nucl. Instrum. and Meth. Phys. Res. B* 323 (2013), p. 191.
- [GS91] J.-J. Gaimard and K.-H. Schmidt. “A Reexamination of the abrasion-ablation model for the description of the nuclear fragmentation reaction”. *Nucl. Phys. A* 531 (1991), p. 709.
- [Gei+92] H. Geissel et al. “The GSI projectile fragment separator (FRS): a versatile magnetic system for relativistic heavy ions”. *Nucl. Instrum. Methods Phys. Res. B* 70 (1992), p. 286.

- [Ger16] R. Gernhäuser. *Precision of Mass Measurements with the Collector Ring at FAIR*. private communication. 2016.
- [Glo+05] J. Glodo et al. “Effects of Ce Concentration on Scintillation Properties of LaBr<sub>3</sub>:Ce”. *IEEE Trans. Nucl. Sci.* 52 (2005), p. 1805.
- [GM48] M. Goeppert-Mayer. “On closed shells in nuclei”. *Phys. Rev.* 74 (1948), p. 235.
- [GMJ55] M. Goeppert-Mayer and J.H.D. Jensen. *Elementary Theory of Nuclear Shell Structure*. New York: John Wiley and Sons, 1955.
- [Gra04] H. Grawe. “Shell Model from a Practitioner’s Point of View”. *Springer Lecture Notes in Physics* 615 (2004), p. 33.
- [GLMP07] H. Grawe, K. Langanke, and G. Martinez-Pinedo. “Nuclear structure and astrophysics”. *Reg. Prog. Phys.* 70 (2007), p. 1525.
- [Gra+95] H. Grawe et al. *Physica Scripta T* 56 (1995), p. 71.
- [Gra+06] H. Grawe et al. “Nuclear structure far of stability - Implications for nuclear astrophysics”. *Eur. Phys. J. A* 27 (2006), p. 257.
- [HS93] I. Hamamoto and H. Sagawa. “Gamow-Teller beta decay and isospin impurity in nuclei near the proton dripline”. *Phys. Rev. C* 48 (1993), p. 960.
- [HT15] J. C. Hardy and I. S. Towner. “Superallowed  $0^+ \rightarrow 0^+$  nuclear  $\beta$  decays: 2014 critical survey, with precise results for  $V_{ud}$  and CKM unitarity”. *Phys. Rev. C* 91 (2015), p. 025501.
- [Har+90] J. C. Hardy et al. “Superallowed  $0^+ \rightarrow 0^+$  nuclear  $\beta$  decays: A critical survey with tests of CVC and the standard model”. *Nucl. Phys.* 509 (1990), p. 429.
- [HJS49] O. Haxel, J.H.D. Jensen, and H. E. Suess. “On the ‘magic numbers’ in nuclear structure”. *Phys. Rev.* 75 (1949), p. 1766.
- [Hee+94] J. Heese et al. “High spin states and shell model description of the neutron deficient nuclei <sup>90</sup>Ru and <sup>91</sup>Ru”. *Phys. Rev. C* 49 (1994), p. 1896.
- [Hin10] C. Hinke. “Spectroscopy of the doubly magic nucleus <sup>100</sup>Sn and its decay”. PhD thesis. Technische Universität München, 2010.
- [Hin+12] C. Hinke et al. “Superallowed Gamow–Teller decay of the doubly magic nucleus <sup>100</sup>Sn”. *Nature* 486 (2012), p. 341.
- [Ili+02] C. Iliades et al. “The effects of thermonuclear reaction-rate variations on nova nucleosynthesis: a sensitivity study”. *Astrophys. J. Suppl. Ser.* 142 (2002), p. 105.
- [Ima+14] H. Imao et al. “Air stripper for high-intensity xenon beam”. *RIKEN Accel. Prog. Rep.* 47 (2014), p. 147.
- [Kib+08] T. Kibedi et al. “Evaluation of theoretical conversion coefficients using BrIcc”. *Nucl. Instrum. Meth. Phys. Res. A* 589 (2008), p. 202.
- [Kie96] P. Kienle. “On the limit of nuclear stability - The region of double magic <sup>100</sup>Sn and bound-state  $\beta$ -decay of <sup>187</sup>Re<sup>75+</sup>”. *Hyp. Int.* 103 (1996), p. 49.

- [Kie+01] P. Kienle et al. “Synthesis and Halfives of Heavy Nuclei Relevant for the rp-Process”. *Prog. Part. Nucl. Phys.* 46 (2001), p. 73.
- [Kim+05] K. Kimura et al. “High-rate particle identification of high-energy heavy ions using a tilted electrode gas ionization chamber”. *Nucl. Instrum. and Meth. Phys. Res. A* 538 (2005), p. 608.
- [Kli+52] P. F. A. Klinkenberg et al. “Tables of nuclear shell structure”. *Rev. Mod. Phys.* 24 (1952), p. 63.
- [Kub+12] T. Kubo et al. “BigRIPS separator and ZeroDegree spectrometer at RIKEN RI Beam Factory”. *Prog. Theor. Exp. Phys.* (2012), p. 03C003.
- [Kum+01] H. Kumagaia et al. “Delay-line PPAC for high-energy light ions”. *Nucl. Instrum. and Meth. Phys. Res. A* 470 (2001), p. 562.
- [La +02] M. La Commara et al. “Beta decay of medium and high spin isomers in  $^{94}\text{Ag}$ ”. *Nucl. Phys. A* 708 (2002), p. 167.
- [Lew+94] M. Lewitowicz et al. “Identification of the doubly-magic nucleus  $^{100}\text{Sn}$  in the reaction  $^{112}\text{Sn} + \text{natNi}$  at 63 MeV/nucleon”. *Phys. Lett. B* 332 (1994), p. 20.
- [Lid+06] S. N. Liddick et al. “Discovery of  $^{109}\text{Xe}$  and  $^{105}\text{Te}$ : Superallowed  $\alpha$  Decay near Doubly Magic  $^{100}\text{Sn}$ ”. *Phys. Rev. Lett.* 97 (2006), p. 082501.
- [Lip+98] M. Lipoglavsek et al. “E2 polarization charge in  $^{102}\text{Sn}$ ”. *Phys. Lett. B* 440 (1998), p. 246.
- [Lip+02] M. Lipoglavsek et al. “Break up of the doubly magic  $^{100}\text{Sn}$  core”. *Phys. Rev. C* 66 (2002), 011302(2).
- [Lip+05] M. Lipoglavsek et al. “ $^{100}\text{Sn}$  core excitations in  $^{97}\text{Ag}$ ”. *Phys. Rev. C* 72 (2005), p. 061304.
- [LLC] XIA LLC. *User’s Manual Digital Gamma Finder (DGF)*. English. Version Version 4.03. XIA LLC.
- [Lor+12] G. Lorusso et al. “ $\beta$  delayed proton emission in the  $^{100}\text{Sn}$  region”. *Phys. Rev. C* 86 (2012), p. 014313.
- [MSA69] M. Moinester, J.P. Schiffer, and W.P. Alford. “Multipole Analysis of Particle-Particle or Particle-Hole Multiplets”. *Phys. Rev.* 179 (1969), p. 984.
- [Mor+78] D. J. Morrissey et al. “Target residue mass and charge distributions in relativistic heavy ion reactions”. *Phys. Rev. C* 18 (1978), p. 1267.
- [Mos+15] K. Moschner et al. “Study of ground state and excited state decays in  $N \approx Z$  Ag nuclei”. *EPJ Web Conf.* 93 (2015), p. 01024.
- [MM33] N. F. Mott and H. S. F. Massey. *The Theory of Atomic Collisions*. Oxford: Clarendon Press, 1933.
- [Muk+04] I. Mukha et al. “ $\beta$ -delayed proton decay of a high-spin isomer in  $^{94}\text{Ag}$ ”. *Phys. Rev. C* 70 (2004), p. 044311.
- [Muk+05] I. Mukha et al. “Observation of Proton Radioactivity of the  $(21^+)$  High-Spin Isomer in  $^{94}\text{Ag}$ ”. *Phys. Rev. Lett.* 95 (2005), p. 022501.

- [Muk+06a] I. Mukha et al. “ $\beta$ -delayed proton decay of high-spin isomer in  $^{94}\text{Ag}$ ”. *Nature* 439 (2006), p. 298.
- [Muk+06b] I. Mukha et al. “Proton-proton correlations observed in two-proton radioactivity of  $^{94}\text{Ag}$ ”. *Nature* 439 (2006), p. 298.
- [Nar+11] N. S. Nara Singh. et al. “ $16^+$  Spin-Gap Isomer in  $^{96}\text{Cd}$ ”. *Phys. Rev. Lett.* 197 (2011), p. 172502.
- [Nat16a] National Nuclear Data Center. *Chart of Nuclides*. 2016. URL: <http://www.nndc.bnl.gov/> (visited on 09/03/2016).
- [Nat16b] National Nuclear Data Center. *LOGFT calculator*. 2016. URL: <http://www.nndc.bnl.gov/logft/> (visited on 06/18/2016).
- [Oga+83] K. Ogawa et al. “Shell-model calculations of high-spin isomers in neutron deficient  $1g_{9/2}$ -shell nuclei”. *Phys. Rev. C* 28 (1983), p. 958.
- [Oli+79] L. F. Oliviera et al. “Abrasion-ablation calculations of large fragment yields from relativistic heavy ion reactions”. *Phys. Rev. C* 19 (1979), p. 826.
- [Ots+05] T. Otsuka et al. “Evolution of Nuclear Shells due to the Tensor Force”. *Rev. Mod. Phys.* 95 (2005), p. 232502.
- [Par+09] A. Parikh et al. “The impact of uncertainties in reaction Q-values on nucleosynthesis in type I X-ray bursts”. *Phys. Rev. C* 79 (2009), p. 045802.
- [Par16] J. Park. *Decay spectroscopy of  $N \sim Z$  nuclei in the vicinity of  $^{100}\text{Sn}$* . private communication. 2016.
- [Pec+07] O. L. Pechenaya et al. “Level structure of  $^{92}\text{Rh}$ : Implications for the two-proton decay of  $^{94}\text{Ag}^m$ ”. *Phys. Rev. C* 76 (2007), p. 011304.
- [Pek+71] L. K. Peker et al. “Many particle isomeric states as sources of proton and neutron radio-activity”. *Phys. Lett. B* 36 (1971), p. 547.
- [Pie+07] S. Pietri et al. “Recent results in fragmentation isomer spectroscopy with rising”. *Nucl. Instr. Meth. B* 261 (2007), p. 1079.
- [Ple+94] C. Plettner et al. “Decay properties of the new isotopes  $^{94}\text{Ag}$  and  $^{95}\text{Ag}$ ”. *Z. Phys. A* 350 (1994), p. 99.
- [Ple+02] C. Plettner et al. “ $\beta$  decay of  $^{100}\text{In}$ ”. *Phys. Rev C* 66 (2002), p. 044319.
- [Ple+04] C. Plettner et al. “On the  $\beta$ -decaying ( $21^+$ ) spin gap isomer in  $^{94}\text{Ag}$ ”. *Nucl. Phys. A* 733 (2004), p. 20.
- [Pov+93] B. Povh et al. *Teilchen und Kerne*. Springer, 1993.
- [Pł+92] A. Płochocki et al. “Gamow-Teller  $\beta$  decay of the very neutron-deficient  $N=50$  nuclide  $^{98}\text{Cd}^*$ ”. *Zeitschrift für Physik A* 342 (1992), p. 43.
- [RC06] R. Ragnarsson and B. G. Carlsson. “Favoured high-spin states in  $N \approx Z$  nuclei close to  $^{100}\text{Sn}$ ”. *Nuclear Structure Conference Booklet* (2006).
- [Rei13] S. Reichert. “Study of  $K_x$ -Ray Multiplicities of Evaporation Residues in Heavy Fusion Systems Using the MINIBALL Spectrometer”. MA thesis. Technische Universität München, 2013.

- [Rei94] J. Reinhold. “Produktionsquerschnitte und longitudinale Impulsverteilungen neutronenarmer Fragmente in der Reaktion  $^{129}\text{Xe} + ^{27}\text{Al}$  bei  $E_{\text{lab}} = 790 \text{ AMeV}$ ”. PhD thesis. Technische Universität München, 1994.
- [Sch+79] D. Schardt et al. “Alpha decay studies of tellurium, iodine, xenon and cesium isotopes”. *Phys. Rev. Lett.* 326 (1979), p. 65.
- [SR06] H. Schatz and K. E. Rehm. “X-ray binaries”. *Nucl. Phys.* 777 (2006), p. 601.
- [Sch+98a] H. Schatz et al. “rp-process nucleosynthesis at extreme temperature and density conditions”. *Phys. Rep.* 294 (1998), p. 167.
- [Sch+01] H. Schatz et al. “End Point of the rp Process on Accreting Neutron Stars”. *Phys. Rev. Lett.* 86 (2001), p. 3471.
- [Sch+98b] C. Scheidenberger et al. *Nucl. Instrum. Methods Phys. Res. B* 142 (1998), p. 441.
- [Sch+84] K.-H. Schmidt et al. “Some Remarks on the Error Analysis in the Case of Poor Statistics”. *Z. Phys A - Atoms and Nuclei* 316 (1984), p. 19.
- [Sch95a] R. Schneider. “ $\gamma$ -ray spectroscopy at RIPS and BigRIPS”. *Proc. 5th Int. Sym. Physics of Unstable Nuclei* 588 (1995), p. 191.
- [Sch95b] R. Schneider. “Nachweis und Untersuchung des Zerfalls von  $^{100}\text{Sn}$  und benachbarter Kerne”. PhD thesis. Technische Universität München, 1995.
- [Sch+95] R. Schneider et al. “Identification and Half-life Measurement of  $^{100}\text{Sn}$  and Neighbouring Nuclei”. *Phys. Scr. T* 56 (1995), p. 67.
- [Ser47] R. Serber. “Nuclear Reactions at High Energies”. *Phys. Rev.* 72 (1947), p. 1114.
- [ST63] A. de Shalit and I. Talmi. *Nuclear Shell Theory*. New York and London: Academic Press, 1963.
- [SH03] B. Singh and Z. Hu. “Nuclear Data Sheets for  $A = 98$ ”. *Nucl. Data Sheet* 98 (2003), p. 335.
- [Sin+98] B. Singh et al. “Review of  $\log ft$  values in  $\beta$ -decay”. *Nucl. Data Sheets (N.Y. N.Y.)* 84 (1998), p. 487.
- [SP08] O. Sorlin and M.-G. Porquet. “Nuclear magic number: New features far from stability”. *Prog. Part. Nucl. Phys.* 61 (2008), p. 602.
- [Ste09] K. Steiger. “Effizienzbestimmung des Detektoraufbaus für die Zerfallsspektroskopie von  $^{100}\text{Sn}$ ”. MA thesis. TUM, 2009.
- [Sto02] A. Stolz. “Untersuchung des Gamov-Teller-Zerfalls in der Nachbarschaft von  $^{100}\text{Sn}$ ”. PhD thesis. TUM, 2002.
- [SW85] C. A. Stone and W. B. Walter. “The parabolic rule, the Pandya-transformation, and the structure of  $^{100}\text{In}$ ”. *Hyperfine Interactions* 22 (1985), p. 363.
- [Str10] K. Straub. “Zerfallseigenschaften von Nukliden in der Umgebung von  $^{100}\text{Sn}$ ”. PhD thesis. TU München, 2010.
- [SH+10] K. Straub, C. Hinke, et al. “Decay of drip-line nuclei near  $^{100}\text{Sn}$ ”. *GSI Scientific Report* (2010), p. 151.

- [SB+00] K. Sümmerer, B. Blank, et al. “Modified empirical parametrization of fragmentation cross sections”. *Phys. Rev. C* 61 (2000), p. 034607.
- [Suz13] H. Suzuki. “Production cross section measurements of radioactive isotopes by BigRIPS separator at RIKEN RI Beam Factory”. *Nucl. Instrum. Meth. B* 317 (2013), p. 756.
- [Sze+95] J. Szerypo et al. “Beta decay of neutron-deficient even-mass indium isotopes: Evidence for population of highly-excited states in the cadmium-daughter nuclei”. *Nucl. Phys. A* 584 (1995), p. 221.
- [Sö+13] P.-A. Söderström et al. “Installation and Commissioning of EURICA - Euroball-RIKEN Cluster”. *Nucl. Instrum. and Meth. Phys. Res. B* 317 (2013), p. 649.
- [Sü12] K. Sümmerer. “Improved empirical parametrization of fragmentation cross sections”. *Phys. Rev. C* 86 (2012), p. 014601.
- [Sü+90] K. Sümmerer et al. “Target fragmentation of Au and Th by 2.6 GeV protons”. *Phys. Rev. C* 42 (1990), p. 2546.
- [TB08] O. B. Tarasov and D. Bazin. “LISE++ Radioactive beam production with in-flight separators”. *Nucl. Instrum. Methods Phys. Res. B* 266 (2008), p. 4657.
- [Tow85] I. S. Towner. “A mass dependence in hindrance factors for favoured Gamow-Teller transitions”. *Nucl. Phys. A* 444 (1985), p. 402.
- [vHW85] K. von Meyenn, A. Hermann, and V. F. Weisskopf. “Wissenschaftlicher Briefwechsel mit Bohr, Einstein, Heisenberg, u. a., Vol. II: 1930-1939”. *Springer-Verlag* (1985).
- [WW81] R. K. Wallace and W. E. Woosley. “Explosive Hydrogen Burning”. *Nucl. Phys.* 45 (1981), p. 389.
- [WAW+12] M. Wang, G. Audi, A. H. Wapstra, et al. “The AME2012 atomic mass evaluation”. *Chin. Phys. C* 36 (2012), p. 1603.
- [WBM15] N. Warr, Blazhev, and K. Moschner. “Simulations of the SIMBA array towards the determination of  $Q_\beta$  values”. *EPJ Web of Conf.* 93 (2015), p. 07008.
- [Wef+00] E. Wefers et al. “Measurement of Decay Properties of p-Rich Nuclei Near  $^{100}\text{Sn}$ ”. *GSI Scientific Report* (2000), p. 23.
- [Wef+07] E. Wefers et al. “Decay Properties of the Heaviest  $N \sim Z$  Nuclei”. *Private Communication* (2007).
- [Wu+57] C. S. Wu et al. “Experimental Test of Parity Conservation in Beta Decay”. *Phys. Rev.* 105 (1957), p. 1413.
- [Yan04] Y. Yano. “RI Beam Factory at RIKEN”. *Proc. 17th Int. Conf. on Cyclotrons and Their Applications* (2004), p. 169.
- [Yan07] Y. Yano. “The RIKEN RI Beam Factory Project: A status report”. *Nucl. Instr. Meth. B* 261 (2007), p. 1009.

# Acknowledgment

An intense time of working in a great collaboration exploring a unique area of the nuclear chart has passed by. I would like to sincerely thank everybody who has supported me during the last three years that this project could succeed. First and foremost, I am very grateful that Reiner Krücken accepted me as a student and introduced me to Jason Park to start the analysis together. In particular, Roman Gernhäuser gave me the opportunity to work in this exciting area of nuclear physics and it has been a great pleasure to me working with him. Together with Thomas Faestermann and Jason Park, profound analysis could be performed. I do appreciate our challenging, controversial and fruitful discussions as we managed to have a meeting almost once a week.

Furthermore, I would like to thank Shunji Nishimura who was supervising me during the time as an IPA student at RIKEN. Konrad Steiger, Zhengyu Xu, Michael Milde, Kevin Moschner and Nigel Warr were a great support with regards to the analysis software as well as the `Geant4`-simulation of the WAS3ABi setup. Finally, I would like to thank my girlfriend Keiko, my family and my friends for the power and the time which they gave me to work in this project. Last but not least, my special thanks go to Sumiko Nito who made me feeling home in Wako-shi and who always accommodated me when I had to visit Japan even spontaneously.

## EURICA RIBF09 Collaboration

This experiment was performed by a great number of collaborators: J. Park, M. Lewitowicz, R. Krücken, R. Gernhäuser, S. Nishimura, H. Sakurai, H. Baba, B. Blank, A. Blazhev, P. Boutachkov, F. Browne, I. Celikovic, P. Doornenbal, T. Faestermann, Y. Fang, G. de France, N. Goel, M. Gorska, S. Ilieva, T. Isobe, A. Jungclaus, G. D. Kim, Y.-K. Kim, I. Kojouharov, M. Kowalska, N. Kurz, Z. Li, G. Lorusso, K. Moschner, I. Nishizuka, Z. Patel, M. M. Rajabali, S. Rice, H. Schaffner, L. Sinclair, P.-A. Söderström, K. Steiger, T. Sumikama, H. Watanabe, Z. Wang, J. Wu, Z. Y. Xu. I appreciate the support by everybody that the analysis could be completed coherently. Particularly, the former Nuclear Physics Group E12 at TUM has provided the ideal environment for analysis and discussion.

This work was supported and financed by the Excellence Cluster Origin and Structure of the Universe, the Hanns-Seidel-Stiftung and the IPA Programme of the RIKEN Nishina Center.